PHOTOASSOCIATION SPECTROSCOPY OF A DEGENERATE FERMI GAS OF ^{6}LI

by

Mariusz Semczuk

MSc, University of Warsaw, 2009

A THESIS SUBMITTED IN PARTIAL FULFILLMENT
OF THE REQUIREMENTS FOR THE DEGREE OF

DOCTOR OF PHILOSOPHY

in

The Faculty of Graduate and Postdoctoral Studies

(Physics)

THE UNIVERSITY OF BRITISH COLUMBIA

(Vancouver)

January 2015

Abstract

This thesis describes a suite of experimental tools and spectroscopic measurements performed on ultra-cold ^{6}Li molecules. The aim is to create the necessary ingredients for the coherent transfer of the population of ultracold, weakly bound, Feshbach molecules of ^{6}Li to deeply bound ro-vibrational levels, making the eventual creation of a Bose-Einstein condensate (BEC) of ground state lithium dimers a reality at the University of British Columbia. Some of the technological milestones include the development of a unique laser system consisting of two Ti:Sapphire lasers frequency stabilized to a femtosecond frequency comb as well as the demonstration of the first in Canada BEC of Feshbach molecules.

To determine a suitable path for the coherent transfer using stimulated Raman adiabatic passage (STIRAP) we measure the binding energies of the vibrational levels $v'' = 20 - 26$ of the $c(1^3\Sigma_g^+)$ and $v'' = 29 - 35$ of the $A(1^1\Sigma_u^+)$ excited states of lithium dimers by the photoassociation of a degenerate Fermi gas of ^{6}Li atoms, achieving accuracy of 600 kHz. For each vibrational level of the triplet potential, we resolve the rotational structure using a Feshbach resonance to enhance the photoassociation rates from p-wave collisions. We also, for the first time, determine the spin-spin and spin-rotation interaction constants for this state.

Finally, we are the first to demonstrate exotic dark states in quantum gases of fermionic lithium where atom-molecule coherence is produced between a deeply bound singlet (or triplet) molecular level and atomic pairs in a weakly interacting Fermi gas at zero gauss or in the BEC-BCS crossover regime (i.e. Feshbach molecules or BCS-like pairs). We observe an abrupt and unanticipated change of the classic EIT signature (Electromagnetically Induced Transparency) of the dark-state (i.e. the suppression of single photon absorption to the excited state) in the vicinity of the broad Feshbach resonance at 832.2 G potentially indicating new physics not previously considered.

Preface

Chapter 2 extends the material that has been published in W. Gunton *et al.*, Phys. Rev. A, **88**, 023624, Aug (2013) of which I am an author. I was involved in every stage of the design of the experiment, data taking and analysis. I wrote parts of the manuscript and participated in editing. Figures 2.17, 2.18, 2.19, 2.20, 2.21 are made by W. Gunton and come from W. Gunton *et al.* (2013).

The results of Chapter 3 have been published in M. Semczuk *et al.*, Phys. Rev. A **87**, 052505, May (2013) and W. Gunton *et al.*, Phys. Rev. A **88**, 062510, Dec (2013) of which I am an author. I was involved in every stage of the design of the experiment, data taking and analysis. I wrote parts of the manuscripts and participated in editing. The theoretical analysis of molecular potentials presented in the above papers was performed by Dr. N. S. Dattani and is not included in this dissertation. Figures 3.4 and 3.9 are made by Dr. N. S. Dattani and Dr. X. Li, respectively and come from M. Semczuk *et al.* (2013).

Chapter 4 is based on M. Semczuk *et al.*, Phys. Rev. Lett. **113**, 055302, July (2014). I was involved in every stage of the design of the experiment, data taking and analysis. I wrote and edited the manuscript incorporating feedback from other authors. I was responsible for submission process of the manuscript for publication and prepared replies to referees' comments. Figure 4.14 was made by W. Gunton and comes from M. Semczuk *et al.* (2014).

Table of Contents

List of Tables

List of Figures

List of Abbreviations

AOM	acousto-optic modulator
BCS	Bardeen - Cooper - Schrieffer
BEC	Bose-Einstein condensate
CDT/CODT	crossed dipole trap
FR	Feshbach resonance
mBEC	molecular Bose-Einstein condensate
MOT	magneto-optical trap
ODT	optical dipole trap
PA	photoassociation
REMPI	resonance-enhanced multiphoton ionization
STIRAP	stimulated Raman adiabatic passage

Acknowledgments

A 5.5-year long journey has come to an end...Both personally and professionally it has been a rollercoaster, but I am privileged to have shared both ups and downs with many amazing people.

First and foremost, my great thanks go to my supervisor, Kirk Madison. Working with him was a very enriching experience that let me grow as a scientist and as a person. It was overwhelming at times to witness how much he knew, not only about physics, and how quickly he grasped the essence of a problem whenever he faced one. I admire his attitude towards students and everyone working for him immediately realizes that he really cares about you, that your growth and success are important to him and he would do anything to help you achieve your goals. I greatly benefited from numerous discussions we had and many advices I received helped me better shape my future. I owe most of my success to him.

Postdocs Bruce Klappauf and Ben Deh were essential in introducing me to the field of ultra cold atoms in the early stages of my graduate career. I appreciate their effort to teach me experimental skills and I apologize for constantly interrupting their work by asking often silly questions - but in the end the time they spent as my teachers turned out to be a pretty decent investment.

This thesis would not be what it is if it was not for Will Gunton. Working in a team with him was very rewarding and enjoyable. I feel like in many aspects we completed each other and our differences were, in my opinion, the strongest asset of our collaboration. It was rare that we immediately agreed on things, but this only forced both sides to think a little deeper about a problem and I believe it made both of us much better scientists. Now the experiment is in his capable hands and there is no doubt in my mind that he will lead it to greatness.

From the very beginning of my stay in Canada I had a great pleasure to have Gene Polovy as a friend. I could always count on him and I learned a lot about everyday life in Canada from him. This added a lot of value to my experience as a foreigner. He helped to make my life outside of the lab more fun, maybe at times even more than it was initially anticipated. In the end we will both remember the

shenanigans we went through over the years and decades from now we will have memories that will bring smiles to our wrinkled faces.

Janelle's cookies fuelled us during countless hours in the lab, often serving as a substitute for a proper meal. Her kind personality contributes to the friendly atmosphere in the lab. You rarely find people that nice and helpful and I am sure that generations of students can also testify to that. Her father, a frequent visitor, offered a very unique perspective on life and I appreciate his constant support and his faith in me.

I enjoyed many laughs and very fun discussions with Kais and Jim, the MAT (and then PAT) guys. I really hope that their experiment will produce great results soon and they will help establish the first ultra cold atom based pressure standard.

A brand new addition to the team, Kahan and Koko, very quickly became indispensable members of the group. I am glad I had a chance to work with them and I am looking forward to seeing their growth - which, I believe, will be spectacular.

Joining Psi Upsilon immediately after arriving in Canada let me feel like a part of a family of a sort. It gave me an opportunity to meet many amazing people who became my friends. The countless hours spent "on the pine" with them helped me understand Canada and Canadians much better. It was a great getaway from the lab work and it will be always a source of great stories and fond memories.

Last but not least, I want to acknowledge my parents and the rest of my family for their constant support. I hope I made you proud.

Chapter 1

Introduction

Spectacular progress in cooling of atoms resulted in a series of ground breaking experiments leading to the 1995 breakthrough: the production of Bose-Einstein condensate of alkali atoms (BEC) by groups from JILA/University of Colorado [1], MIT [2] and Rice University [3]. A wealth of new opportunities to study Nature opened to researchers and for last 20 years the field has been only gaining momentum, to the extend that nowadays some atomic physicists are even called "condensed matter physicists" (for example Markus Greiner from Harvard University). Ultracold atoms and molecules trapped in optical lattices became "quantum simulators", shedding light on many aspects of condensed matter systems [4] but their applications reach beyond that [5, 6].

Many questions about fundamental concepts in physics can be nowadays addressed in experiments using ultracold atoms, or relying on the techniques developed for their studies. For example, the manipulation of single atoms with photons and single photons with atoms was recognized with the 2012 Nobel prize in physics awarded to Serge Haroche and David J. Wineland "for ground-breaking experimental methods that enable measuring and manipulation of individual quantum systems".

The laser-cooled atoms, among others, have been used to measure the Newtonian gravitational constant [7, 8], parity nonconservation in cesium [9], predicted by general relativity gravitational redshift [10] and are expected to enable the realization of the original Einstein-Podolsky-Rosen proposal [11–13] where the entanglement of the external degrees of freedom of freely moving massive particles can be used to test the fundamental aspects of quantum mechanics.

Some topics that emerged from the studies of ultracold matter have already entered the realm of "applied research". Many national metrology institutes (for example Physikalisch-Technische Bundesanstalt, Germany; National Institute of

Standards and Technology, USA; National Physical Laboratory, UK) have research programs focusing on the development of frequency standards using optical clocks based on ions [14, 15] and atoms in optical lattices [16, 17]. Atom interferometers [18], where optical fields are replaced by interfering matter waves of Bose-Einstein condensates, have recently became contenders as a technology of the future. This approach has been recently validated by the British Ministry of Defence by funding research projects that, amongst others, are expected to develop table-top atom interferometers to provide ultra-precise, highly reliable positional data for submarines at depth, where traditional GPS satellite navigation systems will not work.

Applications of ultracold atoms for both fundamental science and emerging technologies cannot be underestimated and the future for the field is bright. It is a matter of time when newly developed techniques will be extended to more complicated systems like molecules or even macroscopic objects, hopefully proving once again that only the sky is the limit if it comes to progress.

1.1 Motivation

From its inception, the Quantum Degenerate Gases laboratory at the University of British Columbia has been focused on investigation of ways to create ground state molecules of LiRb which are expected to have a sizable permanent electric dipole moment of $\mu \sim 4.15 \times 3.33564 \times 10^{-30} \, \mathrm{Cm} = 4.15 \, \mathrm{Debye}$[1] in the $X^1\Sigma^+$ ground state [19–21]. This is a value in a frame where the molecular framework is fixed in space. In the laboratory frame, however, a molecule in a given rotational state has *no permanent electric dipole moment*. It is necessary, therefore, to apply an external electric field that couples states of opposite parity (different rotational states) and thereby polarizes molecules along the field direction [22]. In modern experiments with alkali molecules the electric dipole moment reached in the laboratory frame is typically a fraction of the permanent value ($< 40\%$ [23]), limited by the ability to create high electric fields that would enable full polarization.

Our early results include a demonstration of a dual species magneto-optical

---

[1]Electric dipole moment is frequently expressed in the units of ea_0 with $1\,\mathrm{Debye} = 0.39\,ea_0$. e and a_0 are the elementary charge and Bohr radius, respectively.

trap of ^{6}Li and ^{85}Rb [24] as well as simultaneous trapping of both species in a dipole trap which enabled measurement of magnetic Feshbach resonances, some of the broadest among reported in other heteronuclear mixtures [25].

The long-range $1/r^3$ character and the angular dependence of dipole-dipole interactions (as opposed to $1/r^6$ character of van der Waals interactions between ground state atoms) makes polar molecules an interesting object of studies in the context of strongly interacting systems. Especially, if these molecules are confined in an optical lattice they are expected to enable novel ways to simulate quantum many-body systems, moving it beyond what can be achieved with ultracold atoms (see e.g. [26–28]).

The ratio of interaction energies between two electric (μ) and magnetic (m) dipoles trapped on neighboring sites of an optical lattice is

$$\frac{E^{\text{d-d electric}}}{E^{\text{d-d magnetic}}} \sim \left(c\frac{\mu}{m} \right)^2, \tag{1.1}$$

where c is the speed of light. Contrasting LiRb with dysprosium ($m = 10\mu_{\text{B}} = 10 \times 9.274 \times 10^{-24}$ J/T), the most magnetic atom that has been cooled to the quantum degenerate regime [29, 30] the ratio of electric to magnetic dipolar interactions ~ 2000 strongly favors molecules. An alternative system providing long-range interactions, with electric dipole moments on the order of 1000s Debye, can be easily obtained using ultracold Rydberg atoms [31, 32] due to the scaling of the dipole moment with the square of the principal quantum number n. These highly excited Rydberg states, typically with $n > 50$ are, however, usually short lived ($\sim 50\mu s^2$), therefore they cannot be considered as a universal substitute for molecules.

Ultracold molecules, the character of interactions aside, are interesting in their own rights. They are, for example, an entry point to the exciting field of ultracold chemistry [33–35], where chemical reactions can be controlled with electric and magnetic fields to an unprecedented level [36]. When the de Broglie wavelength increases (as the temperature decreases), many-body interactions become significant such that the spatial confinement of molecules can influence the outcome of chemical reactions, enabling chemistry in restricted geometries. At very low tem-

---

[2]In the literature devoted to Rydberg gases these highly excited levels are treated as "long lived", because they are typically contrasted with first excited states with lifetimes on the order of 500 ns.

peratures the thermal motion of molecules becomes insignificant thus the control of bi-molecular reactions could be possible. Such a degree of control and flexibility is not achievable with molecules in supersonic beams or in hot vapors.

For the eventual transfer of loosely bound Feshbach molecules of ^{6}Li^{85}Rb to the ground state, a fiber based frequency comb has been built [37] with an intent of using it to stabilize the frequency of two Ti:Sapphire lasers that would be used for the stimulated Raman adiabatic passage (STIRAP).

High resolution spectroscopic studies of LiRb had not been available until 2011 [38, 39] and later [40–42] therefore we decided to test the feasibility of our newly developed experimental setup by focusing on Li$_2$, as this molecule had been already quite extensively studied, but primarily outside of the ultracold regime. This approach was meant to develop a know-how required for successful STIRAP.

It was quickly realized that Li$_2$ molecules would be a very interesting object for investigations instead of being only a test bed as initially assumed. Due to their longevity (caused by Fermi suppression of collisional losses) it is possible to create a molecular Bose-Einstein condensate of loosely bound Feshbach molecules and this brings a question whether this could be used as a starting point for STIRAP, resulting in a Bose-Einstein condensate of ground state molecules. Such expectation is unique to fermionic species (^{6}Li and ^{40}K) and so far no Bose-Einstein condensation of Feshbach molecules consisting of bosons has been demonstrated. Even though many experimental groups made significant progress towards this goal, quantum degeneracy of real (here: deeply bound) molecules has not been achieved yet.

Lithium dimers in the ro-vibrational ground state do not have a permanent electric dipole moment, therefore the molecules in the lowest lying triplet potential seem like a more interesting object of investigation. This stems from the fact that they possess a magnetic dipole moment, possibly enabling e.g. observation of molecule-molecule Feshbach resonances [43, 44]. Such resonances are expected to be more numerous than in the atomic case due to the contribution to the scattering process from rotational and vibrational excitations. Addressing this in the ultracold regime with a relatively simple molecule like lithium dimer would be a major step in understanding collisional physics.

The demonstration of atom-molecule dark states in fermionic lithium in the

4

BEC-BCS crossover (as discussed in Chapter 4) opens up exciting possibilities to optically tune interactions between colliding atoms while suppressing spontaneous scattering. Due to the capability to control optical fields on a sub-microsecond timescale it is conceivable to use this approach to study the dynamics of strongly interacting fermionic systems on time scales not easily accessible with standard methods of magnetically tunable Feshbach resonances [45]. The use of optical fields would also enable high-resolution spatial tunability of interactions. In mixtures it might be possible to control interaction strength in a species-dependent way, for example by optically changing interactions between fermions in a ^{6}Li^{85}Rb mixture while boson-fermion and boson-boson interactions are fixed by the magnetic field.

Finally, the ability to trap ground state lithium molecules would provide a system with a well defined initial population of ro-vibrational levels which could be used for studies of ultracold superrotors (fast rotating molecules whose rotational energy is comparable with the molecular bond strength), by utilizing methods developed for molecular beams [46–48]. In these experiments the singlet molecules need to be sufficiently deeply bound such that femtosecond pulses used to prepare rotating molecules cannot drive any transitions between the initial state and states in excited molecular potentials. For pulses centered at $\sim$790 nm (typical for titanium sapphire laser systems) it requires lithium molecules to be prepared in the $X(1^1\Sigma_g^+)$ potential with vibrational quantum numbers at most $v'' = 12$. This restrictions assures that the photon energy is not enough to reach the minimum of the first excited singlet potential $A(1^1\Sigma_u^+)$.

1.2   Projects prior to lithium spectroscopy

Here is a (non-exhaustive) list of projects that I was involved in but which do not directly contributed to the research presented in this thesis. However, they either led to the improvement of the infrastructure of the laboratory or were a source of know-how that was useful when focusing on ^{6}Li.

- Feshbach resonance measurements in the ^{6}Li^{85}Rb mixture confined in a dipole trap. It was the first such a measurement in ^{6}Li^{85}Rb and resulted in the discovery of the broadest Feshbach resonances among all commonly

studied heteronuclear mixtures. The results were published in [25].

- attempt at measurement of electric Feshbach resonances in ^{6}Li^{85}Rb. It had been predicted that DC electric field of about 30 kV/cm would induce an observable shift of a magnetic Feshbach resonance. We built a high voltage setup that was designed to produce electric fields up to 40 kV/cm at the location of the atoms. The fields could be turned on and off in about 100 ms. The electrodes were made from the indium tin oxide (ITO) coated glass and were located outside of the glass cell, 3 cm apart. After a series of experiments unanticipated shielding effects were observed and as a result electric fields higher than about 17 kV/cm were impossible to achieve. Moreover, switching the electric field caused a significant atom loss. As a result, we were unable to create conditions required to successfully perform the planned experiment. The high voltage setup is still an integral part of our experiment and if needed can be used e.g. to study Li$_2$ or, eventually, ^{6}Li^{85}Rb in high DC electric fields.

- a laser system for simultaneous trapping and cooling of 85Rb and 87Rb was designed for experiments in collaboration with prof. Valery Milner. Parts of a vacuum chamber for this project were designed, and a dual species (Li and Rb) 2D MOT chamber was built. This experiment was cancelled due to limited funding but the design of the laser system was used by another graduate student to construct a Rb MOT for an experiment aiming at production of ultracold RbH, in collaboration with prof. Taka Momose.

- mechanical shutters based on 2.5" hard drives were designed and built. This project resulted in shutters that can be assembled even by a relatively unskilled person, on a mass scale. At the same time they are maximally simplified by using only essential elements of a hard drive (magnets and a swinging arm that moves the HDD readout head) and as a result are cheap to build and resemble a commercial product.

1.3   List of papers

The following is the list of papers published during my time as a doctoral student. Publications 2-5 form the basis of this thesis.

1. B. Deh, W. Gunton, B. G. Klappauf, Z. Li, **M. Semczuk**, J. Van Dongen and K. W. Madison, "Giant Feshbach resonances in ^{6}Li-^{85}Rb mixtures.", Phys. Rev. A Rapid Communications, **82**, 020701, August (2010) [25].

2. **M. Semczuk**, X. Li, Xuan, W. Gunton, M. Haw, N. S. Dattani, J. Witz, A. K. Mills, D. J. Jones and K. W. Madison, "High-resolution photoassociation spectroscopy of the ^{6}Li$_2$ $1^3\Sigma_g^+$ state.", Phys. Rev. A, **87**, 052505, May (2013) [49].

3. W. Gunton, **M. Semczuk** and K. W. Madison, "Realization of BEC-BCS-crossover physics in a compact oven-loaded magneto-optic-trap apparatus.", Phys. Rev. A, **88**, 023624, August (2013) [50].

4. W. Gunton, **M. Semczuk**, N. S. Dattani and K. W. Madison, "High-resolution photoassociation spectroscopy of the ^{6}Li$_2$ $A(1^1\Sigma_u^+)$ state.", Phys. Rev. A **88**, 062510, December (2013) [51].

5. **M. Semczuk**, W. Gunton, W. Bowden and K. W. Madison, "Anomalous behavior of dark states in quantum gases of ^{6}Li.", Phys. Rev. Lett. **113**, 055302, July (2014) [52].

1.4   Outline of the thesis

Chapter 2 of this work gives a description of the technical aspects of the experimental setup. All the essential elements of the vacuum system and the laser setups for cooling, trapping and photoassociation are discussed. The field of ultracold atoms is mature enough to justify treatment of certain topics as established knowledge, therefore the theory of magneto-optical trapping, dipole traps and, in general, atom-light interaction which can be easily found in textbooks (e.g. [53]) is kept to minimum. The focus is on solutions that are unique to the approach taken by our group or are essential to the proper interpretation of the experimental results.

Chapter 3 presents the results of the single color photoassociation spectroscopy of vibrational levels $v = 20 - 26$ and $v = 29 - 35$ in $c(1^3\Sigma_g^+)$ and $A(1^1\Sigma_u^+)$ excited potentials of ^{6}Li, respectively. The experiments performed in a sub-μK Fermi gas confined in a dipole trap at 0 G magnetic field report ro-vibrational levels that have never been observed before resulting in a significant improvement of the models describing the $c(1^3\Sigma_g^+)$ and $A(1^1\Sigma_u^+)$ potentials. Building on the idea of s-wave Feshbach resonance enhancement of photoassociation [54] we show a similar enhancement for the c-state spectroscopy to excited levels with $N' = 0, 2$ in the vicinity of the p-wave Feshbach resonance at 185 G. Furthermore, we discuss systematic uncertainties introduced by the residual magnetic fields, photoassociation laser and the dipole trap. Unexpected splitting of the $v = 30$ level in the A-state potential is presented and is attributed to the dipole trap induced coupling to an (unidentified) excited level when the trapping light intensity is high enough.

Chapter 4 reports on the first ever observation of dark states in degenerate gases of fermionic ^{6}Li. Such states have been reported in the past in experiments with bosonic species and Bose-Fermi mixture of KRb but there is no prior work in Fermi gases. Exceedingly long lifetimes of the dark states (as defined by the revival height decay time for extended exposure to the Raman lasers) are observed on the two photon resonance and are orders of magnitude larger than what would naively be expected given the relative phase coherence of the photoassociation lasers and other possible sources of decoherence. In the BEC-BCS crossover regime, close to the $B = 832.18$ G Feshbach resonance, the dark states are produced in a partially Bose-condensed gas of Feshbach molecules (below the resonance) and in a paired degenerate Fermi gas (above the resonance). For magnetic fields below 829 G the revival height on the two-photon resonance unexpectedly and abruptly changes, providing so far the only observable in the BEC-BCS regime that does not exhibit a monotonic behavior.

In order to demonstrate the feasibility of dark states for precision spectroscopy the binding energies of the least bound vibrational levels in $X(1^1\Sigma_g^+)$ and $a(1^3\Sigma_u^+)$ potentials are measured with an accuracy as high as 21 kHz. The accuracy of the level $v = 9$ in the triplet potential is improved 500-fold and its molecular hyperfine structure is resolved. The $v = 38$ level in the singlet potential has not been observed at 0 G prior to our experiments therefore together with $v = 9$ it provides an input

for further refinement of the lowest lying molecular potentials of $^6Li_2$ and, as a consequence, could be used to improve the predictions for the singlet and triplet background scattering lengths of two component ^6Li mixture. For experiments with dark states at non-zero magnetic fields the field free location of the vibrational level $v = 37$ in the singlet potential has been also measured, providing the laser frequencies needed for dark-state studies of the BEC-BCS crossover regime.

Chapter 5 summarizes the results of the thesis and briefly outlines the current status of the experiment. The impact this thesis could have on the field of ultracold atoms and molecules is discussed with the focus on the experiments that build on the methods and results that are the subject of this work.

Chapter 2

Experimental setup

The main results of this Chapter have been published in

- *W. Gunton,* **M. Semczuk***, and K. W. Madison, "Realization of BEC-BCS-crossover physics in a compact oven-loaded magneto-optic-trap apparatus.", Phys. Rev. A,* **88***, 023624, August (2013)* [50].

Even though the field of ultracold quantum gases is very mature there is no off the shelf device that would allow production of degenerate quantum gases on demand, satisfying the requirements of different research groups. There are certain common characteristics of the experimental setups built around the world but in the end each one needs to be customized depending on the specific goals of the planned research program and the atomic species used. This significantly increases both the time it takes to produce scientific results and the start up costs for every new project in the field. In order to simplify the vacuum part of these setups the magneto-optical traps (MOTs) of alkaline atoms can be loaded directly from the background gas as has been demonstrated for Cs [55], Na [56], K [57] and Rb [58] or from the effusive oven as shown for Li in [24, 59, 60]. This path is, however, rarely chosen for experiments with degenerate gases, mainly because the background gas collisions reduce the lifetime of the trapped samples.

This Chapter describes the details of our experimental setup, with the emphasis on these that are unique to the approach taken by our research group. The fermionic lithium source (an oven) loads the magneto-optical trap without being separated from the trapping region with a differential pumping stage. This approach, contrary to previous beliefs, allows efficient creation of molecular Bose-Einstein condensates and BCS pairs, and is comparable in performance (atom number and lifetime of the degenerate sample) to systems where the lithium MOT is loaded from a slow atom sources like a Zeeman slower [61] or a 2D MOT [62]. It results in a compact,

10

relatively inexpensive vacuum setup that can be easily miniaturized.

2.1   Vacuum system and magnetic trapping

The loss induced by the interactions of ultracold atoms with the background gas in vacuum needs to be negligible on the time scales relevant to the experiments. For lithium, this condition can be satisfied for vacuum pressures on the order of 10^{-10} mbar, higher than 10^{-11} mbar required in early experiments with Bose-Einstein condensates [1]. The difference is caused by the rapid evaporation possible in optical dipole traps together with the high elastic collision rate enhanced with a help of a Feshbach resonance. These two factors decrease the time of an experimental cycle thus putting less stringent requirements on the quality of vacuum.

The MOT trapping region is centered within an optically polished quartz cell bonded on both ends to glass to metal transitions, as shown in Fig. 2.1. The choice of the cell's material is mainly dictated by the quartz's low absorption of light at the wavelength used for cooling and trapping of lithium. This minimizes the thermal lensing effects that are often present when dipole traps are created with tightly focused, high power lasers. The atomic source is introduced on one end and is supported inside the cell by a 2.75 inch conflat electrical feedthrough. The other end of the cell is connected through a stainless steel bellows and 6 inch conflat cross to a second, stainless steel chamber which serves as a port for a 20 L s^{-1} Varian StarCell ion pump and a SAES CapaciTorr NEG pump. The outer dimensions of the quartz cell are 30 mm $\times$ 30 mm $\times$ 100 mm with a 5 mm wall thickness.

The atoms are confined by a quadrupole magnetic field created by a pair of water cooled coils enclosed in a PVC housing (Fig. 2.2). The same coils, set to the Helmholtz configuration by reversing the current in one of the coils, are also used to create homogeneous magnetic fields up to 950 G. Cooling is achieved by running tap water at about 10°C. The details of the design can be found in [63].

At low dipole trap powers gravity distorts the trapping potential leading to atoms spill out. This effect can be enhanced by small inhomogeneities of the magnetic field produced by the MOT coils in the Helmholtz configuration. To minimize such losses an additional coil was placed inside the top MOT coil to create a magnetic field gradient. This coil was essential for creation of quantum degenerate
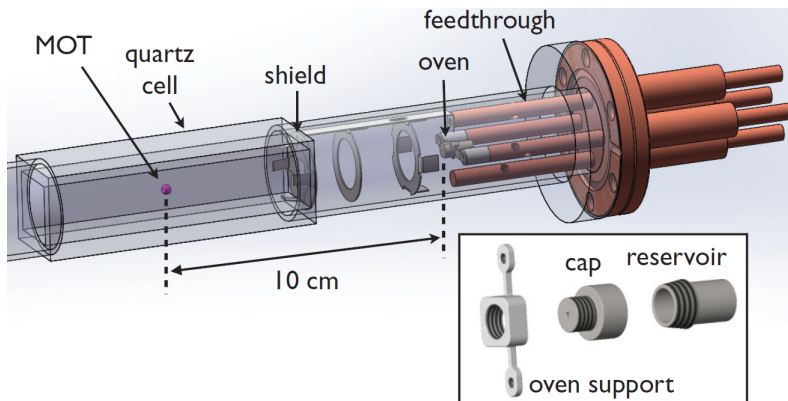
Figure 2.1: Drawing of the vacuum system showing the effusive atomic source, the metal shield used to prevent Li from coating the inside of the quartz cell, and the MOT position, (inset) 3D model of the oven. Figure taken from [50].

samples.

Lithium oven

The effusive lithium oven is located 10 cm from the trapping region in a configuration similar to that reported in Ref. [59] with the exception that here the trapping light for lithium is single frequency and is not broadened in any way to enhance the loading of the MOT. A small beam shield (see Fig. 2.1) is situated between the oven and the trapping region in order to shield the quartz cell walls from the direct output of the effusive oven. The lithium MOT captures atoms from the low velocity tail of the effusive oven output without any additional slowing stages.

The lithium oven consists of a cylindrical reservoir (15 mm long, 7 mm inner diameter, 1 mm wall thickness) enclosed by a screw cap with a 1 mm hole (Fig. 2.1, inset). It is made of non-magnetic stainless steel and the supporting element that is attached to the cap is made of a non-magnetic alloy of nickel and chromium (80% nickel and 20% chromium). It provides a mechanical support and electrical contact between the feedthru electrodes. The thin profile of the leads (1 mm) provides ohmic heating for the atomic reservoir when current is applied. To ensure that hot lithium leaves only through the hole in the cap both the cap and the reservoir have
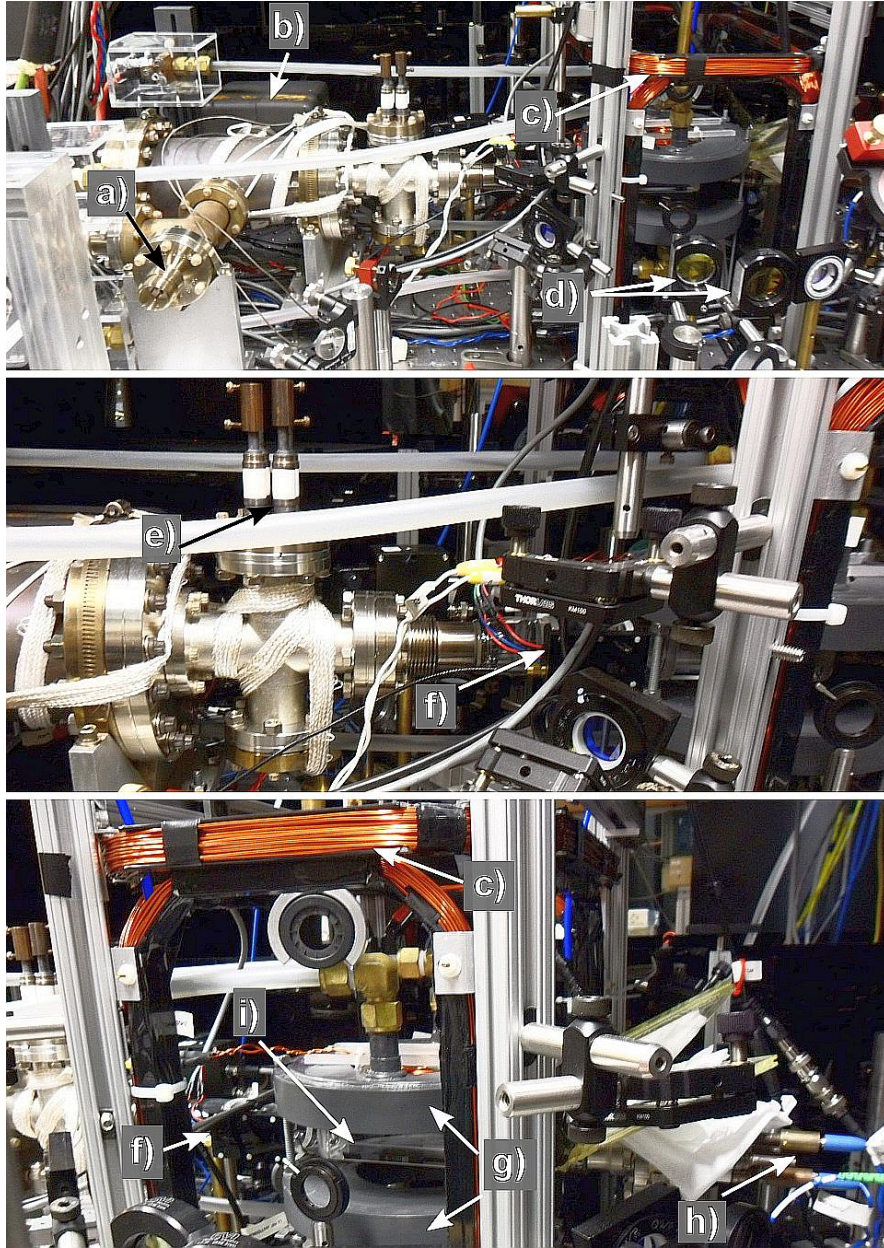
Figure 2.2: View of the vacuum system. (a) NEG pump, (b) ion pump, (c) Helmholtz (compensation) coils, (d) dipole trap optics, (e) rubidium dispenser connectors, (f) black box housing the impedance matching circuit for the rf antenna, (g) MOT coils, (h) oven connectors, (i) glass cell.

13

Figure 2.3: Different views of the stainless steel press designed to create a lithium rod by pushing chunks of lithium through a hole. The diameter of the hole matches the required diameter of the extruded lithium rod that is put into the oven. A slot for a 13/16 wrench was cut to prevent the press from rotating when the piston is screwed in.

tapered threads commonly used in plumbing to connect pipes. This is a significant improvement over our previous design where the connection between the reservoir and the cap was not leak-tight and lithium vapor was found to escape from the sides of the oven [24], effectively reducing the useful lifetime of the source.

Achieving a good vacuum with a hot atomic oven less than 10 cm from the MOT requires careful preparation of the enriched (95% ^{6}Li) sample and systematic degassing of the oven. A nickel wire mesh acts as a wick preventing the molten lithium from draining out of the hot oven. The mesh was rolled onto a 4 mm rod to create a cylindrical roll 10 mm long and with an outer diameter of 7 mm and was then put inside the reservoir. The oven was cleaned with acetone and baked in air at about 300°C to remove contaminants from the machining process. In vacuum equilibrium temperature of the fully assembeled oven (without lithium) was measured as a function of current (Fig. 2.4 and it exhibits a linear dependence:

$$T\,[°C] = 46.5°C/A \times I - 93.8°C. \tag{2.1}$$

The initial sample of lithium was cleaned with petroleum ether to remove residual
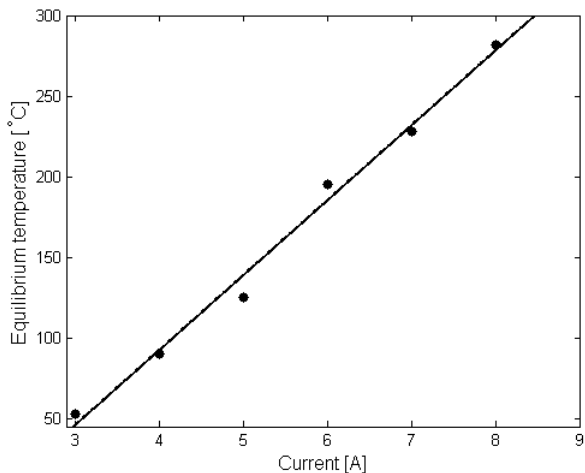
Figure 2.4: The temperature calibration of the oven performed in a test chamber at 10^{-6} Torr. The oven is fully assembled but there is no lithium present.

oil from the surface in an argon filled glove-box. A clean razor blade was used to remove the black exterior from all sides of the lithium sample. The design of the glove-box makes it hard to handle small elements (in this case the lithium sample) therefore to simplify the reservoir loading process and maximize the filling of the oven, the lithium sample was put in a home-built press that produced 10 mm long cylindrical extrusion with a 4 mm diameter (Fig. 2.3). The extrusion was put into the center of the wire mesh roll and covered on the top with an additional round piece of nickel mesh. It is crucial to perform all these steps in an inert gas atmosphere to limit exposure of lithium to air thus limiting the contamination of the sample. In particular, we found that exposure to oxygen, water, or nitrogen was particularly problematic producing an oxide or LiN coating on the exposed metal.

The full lithium oven was degassed by heating it to $200\,^{\circ}\text{C}$ within an auxiliary preparation chamber such that the total pressure from outgassing never exceeded 10^{-6} Torr. The treatment removed the majority of the trapped nitrogen, oxygen, and hydrogen. These were the primary outgassed contaminants as identified by a residual gas analyzer (RGA). The oven was then heated until the pressure due to outgassing at a current of 10 A (corresponding to an oven temperature of 640 K)

fell below the base pressure of the preparation chamber (5×10^{-8} Torr; 10 l s^{-1} pumping speed). After degassing, the preparation chamber was flushed with argon (the use of dry nitrogen was avoided since it was found to contaminate the lithium) and the oven was quickly moved to the experimental vacuum chamber where a 6-day bakeout at 200 °C was performed.

2.2 Trapping, imaging and state preparation

2.2.1 Magneto-optical trapping laser system

The laser system used to cool and image ^{6}Li atoms, shown in Fig. 2.5, is built on a dedicated optical table and the required light is sent to the experiment via 50 m long optical fibers, thus decoupling the light production from the possible unwanted feedbacks from the experiment itself. ^{6}Li is not an ideal 2-level system, therefore cooling requires the presence of two laser fields: "pump" light (near the $2s_{1/2}, F = 3/2 \rightarrow 2p_{3/2}, F = 5/2$ transition frequency) and the "repump" light (near the $2s_{1/2}, F = 1/2 \rightarrow 2p_{3/2}, F = 3/2$ transition frequency). In the $2p_{3/2}$ excited state, the hyperfine level spacings are so small that the pump light, which is typically tuned to the red of the transition by several linewidths, excites with similar rates all three excited states causing rapid depletion of the upper, $F = 3/2$, ground state due to optical pumping. To mitigate this effect, the repump light must have a similar scattering rate as the pump light and it therefore contributes to cooling and exerts a force on atoms in the MOT comparable to that exerted by the pump light. Consequently, both the pump and repump light must be introduced into the trap along all three directions with similar intensities for the proper operation of the lithium MOT.
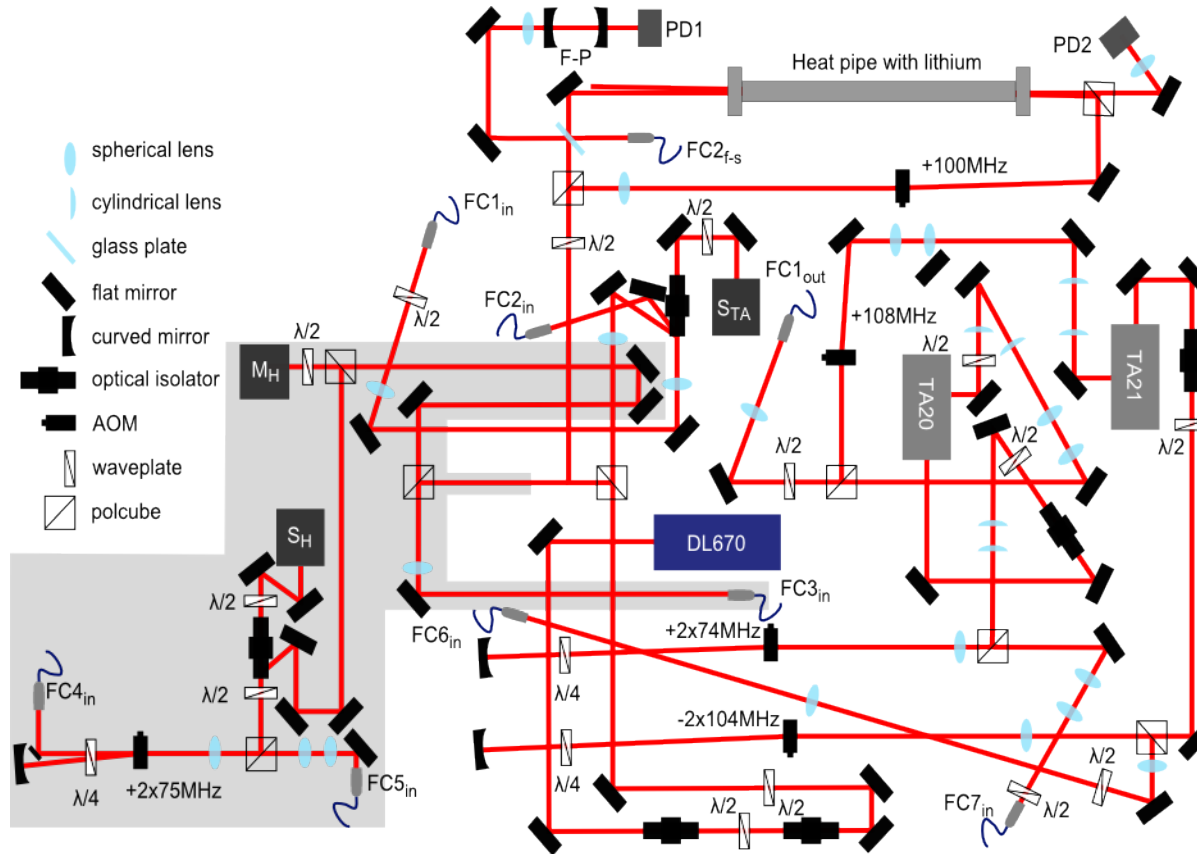
Figure 2.5: Trapping light production and distribution system. The shaded region hosts elements of the high field imaging setup. PD1,PD2: photodiodes; S_{TA}: laser diode seeding tapered amplifiers TA20 and TA21; DL670: master laser Toptica DL670; S_H: laser diode injection locked to a high field imaging master laser M_H; FC1$_{in(out)}$: single mode, polarization maintaining (SM-PM) fiber delivering light for seeding TA20 and TA21; FC2(4)$_{in}$: diagnostics of $S_{TA}(S_H)$, connected to a fiber splitter; FC2$_{f-s}$: output of a fiber splitter, sends light from FC2(4)$_{in}$ to the F-P cavity; FC3$_{in}$: fiber for creating a beatnote between DL670 and M_H; FC5$_{in}$: SM-PM 50 m long high field imaging fiber; FC6(7)$_{in}$: SM-PM 50 m long repump(pump) light fiber.

The master laser (Toptica DL Pro) uses as a reference the signal derived from a Doppler-free saturated absorption spectroscopy of lithium vapor performed in a heat pipe and is locked 50 MHz above the pump transition. 2.6 mW of this stable light is used to injection lock a Mitsubishi ML101J27 laser diode (S_{TA}). These diodes emit 120 mW 660 nm light at 200 mA and a temperature of 25 °C but heating them to 72 °C changes their free running wavelength to 670-671 nm and reduces the output power to 60 mW at 314 mA. The diode is always kept on and we observe that over time the output power decreases therefore to keep it at the 60 mW level the current needs to be increased periodically, usually until it reaches about 450 mA. This, however, still allows us to use one diode for over a year. Turning the diode off every time it is not in use might prolong its lifetime even further.

The cooling light is derived from two tapered amplifiers (TA) from Sacher Lasertechnik which are seeded with 14 mW of light from the laser diode S_{TA}. Typically, the output power of each TA is around 450 mW. The beam quality varies with the alignment of the seeding beams and it has been observed that the optimized power does not necessarily translates into the most efficient coupling into fibers FC6$_{in}$ and FC7$_{in}$ (see Fig. 2.5). To reach required frequencies for the atom trapping the light seeding the pump TA is up-shifted by 108 MHz and then the output of the TA is down-shifted with an acousto-optic modulator (AOM) in a double pass configuration. The output of the repump TA is up-shifted with a double pass AOM. Finally, the pump and the repump light are each coupled into a separate, 50 m long, single mode, polarization maintaining fiber and sent to the experimental table. 80 mW of pump and 60 mW of repump light is available for experiments.

On the experimental table the pump and repump light for trapping is combined into a single beam and, by way of several polarization beam splitter cubes, is split into four beams. Three beams are then expanded to a $1/e^2$ diameter of 2.5 cm, and introduced into the MOT cell along three mutually orthogonal axes in a retro-reflection configuration. It maximizes the optical power available for trapping and so far it has proven to perform better than a six independent beam configuration tested in the early versions of this experiment. The fourth (slowing) beam is sent counter-propagating to the atomic beam, and enters the cell through a viewport at the opposite end of the chamber from the oven. We do not observe any coating of the window by lithium, an issue encountered in many experiments involving

Zeeman slowers. This is primarily because the oven output is not an intense, collimated atomic beam and because the distance from the source to the viewport is large (on the order of 1 m). Effectively, our approach creates a 7-beam MOT, where the slowing beam increases the capture velocity of the MOT along the atomic beam axis, leading to about two-fold improvement in the final atom number.

The main observable in ultracold atom experiments is the atom number measured by absorption imaging. The absorption probe beam uses pump light while a counter-propagating repump beam is included to provide hyperfine repumping with a radiation pressure opposing the probe beam to limit the acceleration of the atoms during imaging.

2.2.2 High field imaging laser system

Due to the limitations of our existing current driver, turning off the magnetic field to image the trapped sample is a relatively slow process often introducing additional atom loss. It also erases any information about the spatial properties of the trapped cloud at the fields where the experiments are performed. In order to mitigate these issues both the experiment and the imaging can take place at the same (or nearby) magnetic field but because the differential Zeeman shift of $2^2S_{1/2}$ and $2^2P_{3/2}$ (see Fig. 2.6) is larger than the typical tuning range (few tens of MHz) of the pump and repump light discussed in section 2.2.1 a separate imaging laser system is needed. At magnetic fields above a few tens of Gauss, the atomic hyperfine coupling is greatly suppressed and the optical transitions used for imaging atomic states become closed and no repump light is required. Only one frequency is necessary and this light is produced by an in-house-built extended cavity diode laser (based on the Roithner RLT6720MG diode laser) that is locked with a large frequency offset to the master laser (Fig. 2.7 shows the working principle of the offset frequency lock). The output is then amplified by injection locking a Mitsubishi ML101J27 diode laser, and the output beam's amplitude and fine frequency tuning is provided by an AOM in a double pass configuration (see Fig. 2.5).

Typically, the imaging light is detuned 600–1000 MHz below the cooling transition with the frequency offset lock and then precisely tuned on resonance with the AOM. The double pass AOM also acts as a shutter and allows us to change the

19
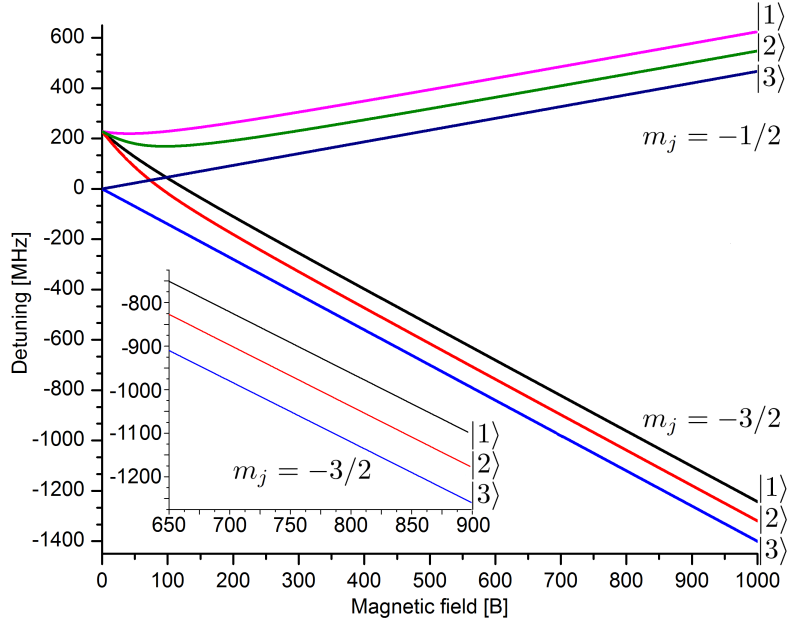
Figure 2.6: Magnetic field dependent detuning of the imaging light from the cooling transition enabling imaging of each of the three high-field seeking states (called $|1\rangle$, $|2\rangle$ and $|3\rangle$). Due to the Zeeman splitting it is possible to independently address these three states by driving optical transitions to $m_j = -1/2$ (upper branch) or $m_j = -3/2$ (lower branch) in the $2^2P_{3/2}$ level. The inset shows the range used for experiments in the BEC-BCS crossover.

beam frequency to image either of the two lowest spin states which are separated by approximately 76 MHz (for fields 600–900 G, see Fig. 2.13). It can also be used to apply short light pulses for spin-selective removal of atoms. The beam is fiber coupled and combined with MOT pump light for imaging at low magnetic fields using a fiber-based combiner (Evanescent Optics Inc.). The imaging axis is perpendicular to the magnetic field, and in this arrangement it is impossible to polarize the light such that it drives only either σ_+ or σ_- transitions. To optimize the absorption signal, the polarization of the imaging beam is set to be linear and along the magnetic field axis. This leads to the underestimation of the atom number in a particular spin state by a factor of two as the imaging light is a mixture of both left and right circular polarizations and only one of these polarizations drives the

Figure 2.7: A diagram of the frequency offset lock. See the text for the explanation of the working principle of the circuit. A more detailed discussion of a circuit of this type can be found in e.g. [64].

transitions of interest.

Down to 200 G below the wide (300 G) resonance at $B = 832.18$ G it is possible to create Feshbach molecules of ^{6}Li. They are sufficiently loosely bound that it is possible to image them with standard absorption imaging [65]. The binding energy is so small that it introduces a negligible frequency shift from the atomic transition, allowing the molecule's atomic constituents to be imaged separately. As with free atoms the absorption image of molecules underestimates the molecule number by a factor of two.

Setting the high field imaging frequency

Let's call δ the detuning of the high field imaging light from the cooling transition (frequency f_{cool}), as shown in Fig. 2.6. The frequency f_H of the high field imaging master is $f_H = f_L \pm f_{beat}$, where $f_L = f_{cool} + 50$ MHz is the frequency of Toptica DL670 and f_{beat} is the beatnote between the two master lasers. The double pass AOM up-shifts f_H by $2f_{AOM} = 130 - 270$ MHz. The frequency f_{AOM} of the double

Figure 2.8: The oscilloscope trace showing the error signal produced by the frequency offset circuit. The horizontal axis shows the frequency difference between the high field imaging laser and Toptica master laser. (Top): full scanning range of the high field imaging master laser. The error signal is symmetric and the shaded area corresponds to the frequencies that are lower than the frequency of the Toptica DL670 master laser. (Bottom): decreasing the scanning range zooms into the shaded area. The high field imaging laser is locked to the highlighted slope (~ 5.1 mV/MHz).

pass AOM can be changed over $65 - 135$ MHz range, more than is required to image both $|1\rangle$ and $|2\rangle$ states without changing f_H. As a result, the beatnote f_{beat} between two masters required to achieve detuning δ is:

$$f_{beat} = |\delta - 2f_{AOM} - 50\,\text{MHz}| \qquad (2.2)$$

The beams derived from the Toptica master laser and the high field imaging master laser are overlapped and then coupled into a common fiber. The output of about 150 μW per beam is directed into a photodiode which records the beatnote δ.

After amplification the beatnote is mixed with the output of the voltage-controlled oscillator. The signal is split into two equal parts which are recombined with a frequency mixer after one part has been delayed by ≈ 2 m of coaxial fiber. The output of the mixer at twice the frequency is blocked by a low pass filter with a cutoff frequency of 1.9 MHz. The resulting output voltage (Fig. 2.8), all else kept constant, is a function of the beatnote frequency δ. The feature spanning from about -200 MHz to +200 MHz is due to the imperfections of the frequency mixer that result in the transmission of the rf signal at low frequencies δ. The signal is cut off at 200 MHz by the low pass filter, but within this range it creates an error-like feature proportional to $\cos \Phi = \cos (2\pi \delta / \Omega_0)$, analogous to the desired $\cos \Phi = \cos (2\pi (\delta - f) / \Omega_0)$ shown in Fig. 2.7.

To create a high quality error signal, the frequency of the local oscillator needs to be set to $f_{\mathrm{VCO}} = f_{\mathrm{beat}} + 92\,\mathrm{MHz}$ [1] and the slope (~ 5.1 mV/MHz) highlighted in Fig. 2.8(bottom) should be used as a reference for the locking circuit. The choice of this specific slope assures that the desired imaging frequencies can be achieved with the frequency shift $2f_{\mathrm{AOM}}$ introduced by the AOM. With a different AOM another slope would perform equally well. The part of the signal to the right of its symmetry axis (Fig. 2.8(top)) corresponds to $f_{\mathrm{H}} < f_{\mathrm{L}}$ such that the excited level addressed by the high field imaging light is $m_j = -3/2$ in $2p_{3/2}$ state. The choice of this level (instead of $m_j = -1/2$ in the $2p_{3/2}$ state, which is less sensitive to the magnetic field [2]) allows us to use the high field imaging laser for a coarse calibration of the magnetic field. Once the f_{beat} is decided on, the imaging frequency can be changed from the control software level only by changing the frequency f_{AOM}.

2.2.3 Dipole traps

The temperature of atoms confined in a MOT is limited by the scattering of photons from the cooling beams. Further decrease of the sample's temperature required to reach quantum degeneracy is achieved with evaporative cooling, which for ^{6}Li is typically done in optical dipole traps, where the elastic collision rate can be widely tuned thanks to the presence of a wide Feshbach resonance at $B = 832.18$ G between states $|1\rangle$ and $|2\rangle$ [66].

---

[1] $\tau = (92\mathrm{MHz})^{-1}$ is related to the delay introduced by the 2 m long delay line shown in Fig. 2.7.
[2] The magnetic dipole moment of $m_j = -3/2$ is $-2\mu_0$B/h vs. $-2/3\mu_0$B/h for $m_j = -1/2$.

The off-resonance scattering of photons

$$\Gamma_{sc} = \frac{3\pi c^2}{2\hbar\omega_0^3} \left(\frac{\Gamma}{\Delta}\right)^2 I \qquad (2.3)$$

and associated heating of the sample by the dipole traps is not an issue here as the lasers used in this work are detuned by more than $\Delta \sim 2\pi \times 165$ THz from both the D_1 and D_2 transitions, with transition frequencies $\omega_0^{D1} = 2\pi \times 446.789634$ THz and $\omega_0^{D2} = 2\pi \times 446.799677$ THz, respectively [67]. $\Gamma = 2\pi \times 5.872$ MHz is the natural linewidth of the transitions [67] and I is the intensity of the trapping light experienced by atoms.

For typical experimental conditions during photoassociation the total power (intensity) of the 1064 nm dipole trap rarely exceeds 1 W (30 kW/cm^2), corresponding to the upper bound on the photon scattering rate of 0.14s^{-1}. Only during the transfer of the atoms from the MOT into the high power dipole trap (1090 nm, total 200 W power and 6 MW/cm^2 intensity) and subsequent fast evaporation (overall some tens of ms) the photon scattering rate reaches 13s^{-1}.

The light for the crossed optical dipole trap (referred to as CODT) is derived from a multi-longitudinal mode, 100 W fiber laser (SPI Lasers, SP-100C-0013) with a central wavelength 1090 nm and a spectral width exceeding 1 nm. The CODT is comprised of two nearly co-propagating beams crossing at an angle of 14° (Fig. 2.9). Recycling the first beam results in the total available power of 200 W. The beams are focused to a waist ($1/e^2$ intensity radius) of 42 μm (first) and 49 μm (recycled) which produces a 6 mK deep trap. The output power of this SPI laser is varied by an analog input controlling the pump diode current of the post amplifier stage.

We limit the time the CODT operates at high power to mitigate the thermal lensing effects which produce beam aberrations. With a quartz cell the position of the beam waists of the CODT arms moves at approximately 780 μm/s when the high power CODT is initially turned on with 100 W per beam [3]. These thermal effects were worse with a previously used vacuum cell made from borosilicate glass. Quartz has a higher transmission in the near IR (e.g. at 1090 nm), and the

---

[3]The beam focus is observed to move 395 μm in the first 500 ms and 280 μm in the next 500 ms due to thermal lensing

24
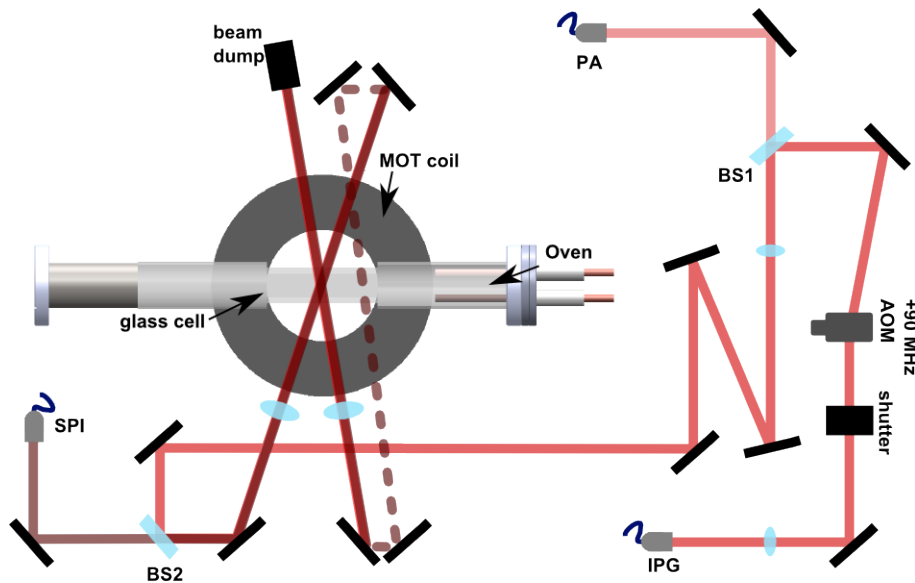
Figure 2.9: The arrangement of the dipole traps used in current experiments. The low and the high power dipole traps are overlapped using a dichroic mirror BS2 from Semrock that transmits 1090 nm and reflects 1064 nm and 780 nm. The photoassociation light and the low power dipole trap are overlapped with a dichroic mirror BS1. This arrangement optimizes the transfer between the dipole traps and provides superior stability over approaches used previously. The dashed line is the part of the path that is moved up to go above the cell.

thermal expansion coefficient of quartz is ten times smaller than that of borosilicate glass.

After initial pre-evaporation in the high power CODT atoms are transferred into a lower-power, 1 mK deep CODT. The light for this second CODT is generated by a single frequency, narrow-linewidth (< 10 kHz), 20 W fiber laser operating at 1064 nm (IPG Photonics YLR-20-1064-LP-SF). This transfer is done to avoid ensemble heating observed in the SPI laser CODT and allows further forced evaporative cooling to much lower powers and thus ensemble temperatures. The 26 nm wavelength difference between the trapping lasers allows overlap of the low-power trap with the SPI on a dichroic mirror (Semrock) that reflects 780 nm and 1064 nm and transmits 1090 nm. With this approach we assure good spatial overlap be-

tween the traps that results in improved transfer efficiency. Most importantly, this approach offers superior stability and minimizes the misalignment of the traps.

Both IPG beams have the same frequency and are focused to waists similar to that of the SPI ($1/e^2$ intensity radius, 42 μm and 49 μm). The polarization of the first beam is chosen to lie in the horizontal plane to minimize reflections at the cell (the cell uncoated). The polarization of the recycled beam deviates from horizontal by a small degree. This results from the beam path the beam travels from one side of the cell to the other and will be addressed in the planned upgrade of the setup. This small relative angle between polarizations of both beams does not limit the performance of the trap.

The IPG CODT beam power is controlled by a water cooled AOM (Intraaction ATD-1153DA6M). The diffraction efficiency of the AOM is 60%. Due to the experimental constraints the polarization of the IPG CODT is perpendicular to the polarization that, according to the manufacturer of the AOM, would lead to the diffraction efficiency of 75%. It is worth noting that the power of neither the SPI nor the IPG laser is actively stabilized.

Trapping potential and trap frequencies

The trapping potential is created by two Gaussian beams crossed in the $X - Y$ plane at an angle α (here $\sim 14°$) [Fig. 2.10]. However, if the thermal energy $k_{\rm B}T$ of an atomic ensemble is much smaller than the potential depth U_0, the trapping potential experienced by a particle with a mass m can be well approximated by the three dimensional potential of a harmonic oscillator [68]

$$U \approx -U_0 + \frac{1}{2}mv_{\rm x}^2 x^2 + \frac{1}{2}mv_{\rm y}^2 y^2 + \frac{1}{2}mv_{\rm z}^2 z^2, \tag{2.4}$$
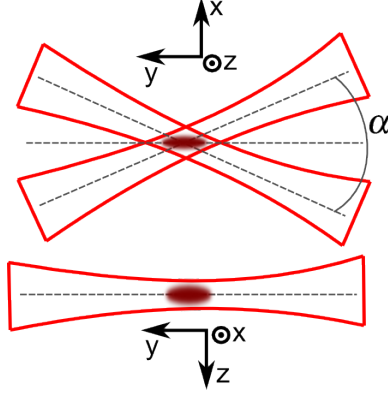
Figure 2.10: Two crossed Gaussian beams creating the optical dipole trap. The elliptical shape in the crossing of the beams corresponds to the atomic cloud. The trapping potential used in the experiments resembles an oblate spheroid (ellipse rotated about one of its axes).

with trap frequencies

$$v_x = \sqrt{\frac{4U_0}{mw_0^2}} \tag{2.5}$$

$$v_y = \sqrt{\frac{4U_0}{mw_0^2}\left(\frac{\alpha}{2}\right)^2} = \frac{\alpha}{2}v_x \tag{2.6}$$

$$v_z = \sqrt{\frac{4U_0}{mw_0^2}} \tag{2.7}$$

Here we assumed that both beams have the same waists w_0 and powers, and $\alpha/2$ is a small angle expressed in radians. U_0 is related to the total power P of the crossed beams and their waists,

$$U_0 = \frac{3c^2P}{\omega_{671}^3 w_0^2}\frac{\Gamma}{\Delta} \tag{2.8}$$

where $\omega_{671} = 2\pi \times 446.789634$ THz and $\Gamma = 2\pi \times 5.9$ MHz are the frequency and the natural linewidth of ^{6}Li D_1 line. $\Delta = 2\pi \times 165$ THz is the detuning of the 1064 nm dipole trap from the transition ω_{671}.

The frequencies of the IPG crossed dipole trap were determined by measuring the trapped atom number after parametric heating. The best quality of the measured

27

signal was achieved in a four step excitation process. (1) The sample was cooled to an IPG power of 0.7 W which was then (2) increased adiabatically (in 1 s) to the desired power. It was verified that this step did not change the T/T_F ratio. (3) The RF power of the water cooled AOM was then modulated for a fixed time, mapping onto power modulation of the dipole trap. (4) Finally, the dipole trap power was turned back down to 0.7 W in 50 ms in order to convert heated atoms into lost atoms. The atom number was measured as a function of modulation frequency, with a loss showing up at twice the trap resonance (for reference see e.g. [69]). Two strong features were present in the spectrum, a low and high frequency one corresponding to v_y and $v_x \approx v_z$, respectively. Assuming the trap is approximately harmonic, the frequency v scales as a square root of the laser power P. Fitting $v = A\sqrt{P}$ yields trapping frequencies:

$$v_y = 0.13\,\text{kHz} \times \sqrt{P/\text{Watt}} \tag{2.9}$$

$$v_x = v_z = 1.9\,\text{kHz} \times \sqrt{P/\text{Watt}} \tag{2.10}$$

Transition to degeneracy

As the sample confined in the dipole trap is cooled, its quantum nature becomes more and more relevant. There are two important cases to consider when working with ultracold ^{6}Li: (a) creation of a Bose-Einstein condensate of loosely bound Feshbach molecules and (b) creation of a degenerate Fermi gas. Case (a) is relevant for magnetic fields below the Feshbach resonance at $B = 832.18$ G. When the phase space density $n_0 \lambda_{\text{dB}}^3 = n_0 \left[2\pi\hbar^2/(mk_B T) \right]^{3/2} \approx 2.61$ the sample undergoes a quantum phase transition that occurs at the temperature T_C

$$T_C = 0.94 \frac{\hbar\bar{\omega}}{k_B} N_{\text{mol}}^{1/3}. \tag{2.11}$$

The condensed fraction for $T < T_C$ is

$$\frac{N_0}{N_{\text{mol}}} = 1 - \left(\frac{T}{T_C} \right)^3. \tag{2.12}$$

In the above equations n_0 is the density at the trap center, N_0 is the population in the BEC phase, N_{mol} is the number of noncondensed molecules, λ_{dB} is de Broglie wavelength, and $\bar{\omega} = (\omega_x \omega_y \omega_z)^{1/3}$ (where $\omega_i = 2\pi \nu_i$). The above relations are true for an ideal (noninteracting) gas but even for real systems they are very good approximations.

For the negative scattering lengths (attractive interactions) present near $B = 0\,\mathrm{G}$ and at magnetic fields larger than $B = 832.18\,\mathrm{G}$ the case (b) takes place. The figure of merit here is the Fermi temperature T_F which for the spin polarized sample of N atoms is

$$T_F = \frac{\hbar \bar{\omega}}{k_B} (6N)^{1/3} \tag{2.13}$$

When the temperature of the sample drops below T_F, the Fermi gas starts to exhibit quantum properties. For example, the average energy per particle starts to deviate from $3 k_B T$ expected from a classical gas [70] and the blocking of the elastic collisions due to the Pauli exclusion principle leads to the decrease in the evaporation efficiency of a two-component Fermi gas [66, 70, 71].

If a two-component Fermi gas (with N atoms per spin state) at a temperature $T \leq 0.5 T_F$ is converted into a gas of N bosonic molecules by adiabatically changing the interactions to repulsive in the vicinity of a Feshbach resonance [72], the resulting bosonic molecules will be below the BEC transition temperature, T_C (Eq. 2.11). Additionally, when T is on the order of $0.5 T_F$, the experimental signatures of the quantum nature of a Fermi gas can be more reliably observed (as in [70]). Therefore, in the field of degenerate Fermi gases $T/T_F \sim 0.5$ is treated as a limit that needs to be reached in order to consider the sample to be quantum degenerate [4].

Previous dipole trap arrangements

It became clear very early that efficient photoassociation of lithium in a single arm dipole trap would be inefficient because the density of sample was not high enough. A cross trap was therefore necessary and we tested two approaches before arriving at the solution described in the previous section. Due to the timing of the dipole trap changes it happened that the data for each of the single color photoassociation

---

[4]This is, by no means, a strict definition but more of a "rule of thumb", useful from the experimental point of view.

papers we published [49, 50] were taken with a different dipole trap arrangement, both shown in Fig. 2.11. For the sake of completeness both, now obsolete, approaches are discussed.

- in order to avoid the creation of a lattice the cross beam was derived from the 0-th order of the main IPG AOM and then down-shifted by 100 MHz (Fig. 2.11a). As a result, the frequency difference between the main and the cross beam was 190 MHz. This solution allowed us to independently control the power of the cross beam and thanks to the use of a fiber the necessary day-to-day alignment was reduced. The main drawback of this solution was the loss of power due to the low efficiency (about 50%) of the AOM. The fiber was a standard 1064 nm fiber from Thorlabs (P3-1064PM-FC-2) and it worked well with incident powers as high as 10 W, maintaining the coupling efficiency of 70% - even though it was not specified for high power aplications. In this arrangement the photoassociation light was overlapped only with the main dipole trap arm. The section that utilizes the 0-th order of the main AOM will be used in the future to create a 1-D lattice and the fiber will guarantee high quality of the lattice beams.

- the independent control of the cross beam power turned out not to provide any additional advantage and the best evaporation efficiency was actually achieved when the powers of both the main and the cross beam were balanced. This led to an alternative dipole trap design shown in Fig. 2.11b) where the IPG beam was recycled after passing through the cell. The recycled beam had the same polarization and is focused to approximately the same size as the main beam. The main advantage of this design is that the photoassociation beam is also recycled, doubling the power available for experiments – an important feature in a situation when there is no reliable theoretical predictions or previous experimental data that would lead to estimations of the power necessary for STIRAP of ^{6}Li. Unexpected heating and loss was observed when the polarization of the second beam was fixed perpendicular to the first (i.e. perpendicular to the horizontal plane and parallel to the magnetic field axis).
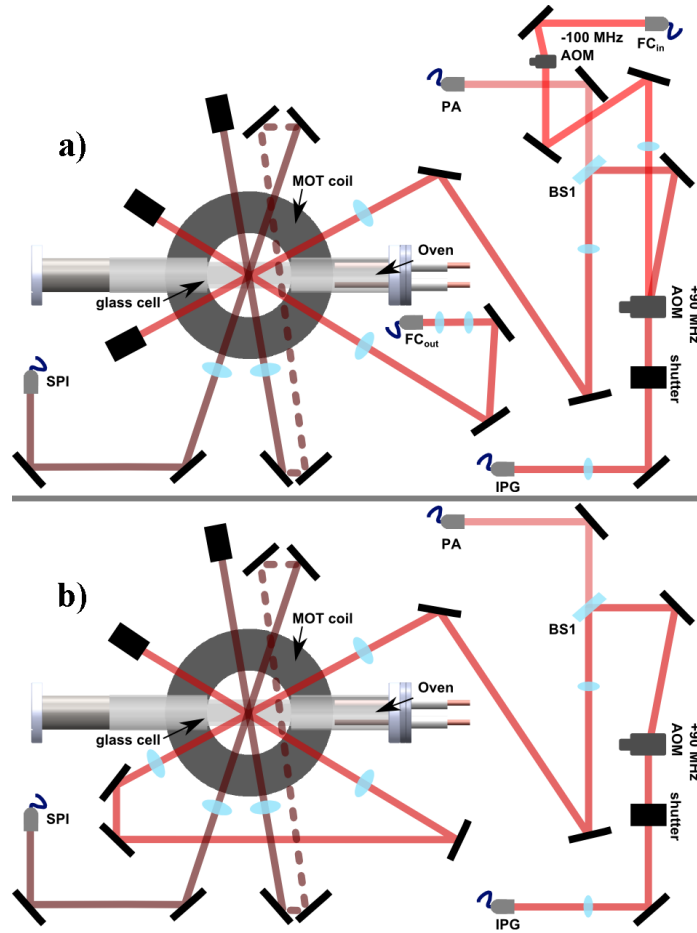
Figure 2.11: Dipole trap arrangements used in previous iterations of the experiment. a) the cross beam of the low power dipole trap is independently controlled with an additional AOM and is derived from the 0-th order of the main IPG AOM. It is sent to the setup via fiber and enters the cell with the same polarization as the main beam. The photoassociation light is overlapped only with the main IPG beam. This arrangement was used to obtain results published in [49], b) the main beam of the low power dipole trap is recycled and both arms have the same polarization. The photoassociation light follows the entire IPG path. This arrangement was used to obtain results published in [51] as well as for the production in the first molecular BEC in Canada [50]. The dashed line corresponds to the recycled beam that is raised above the glass cell.
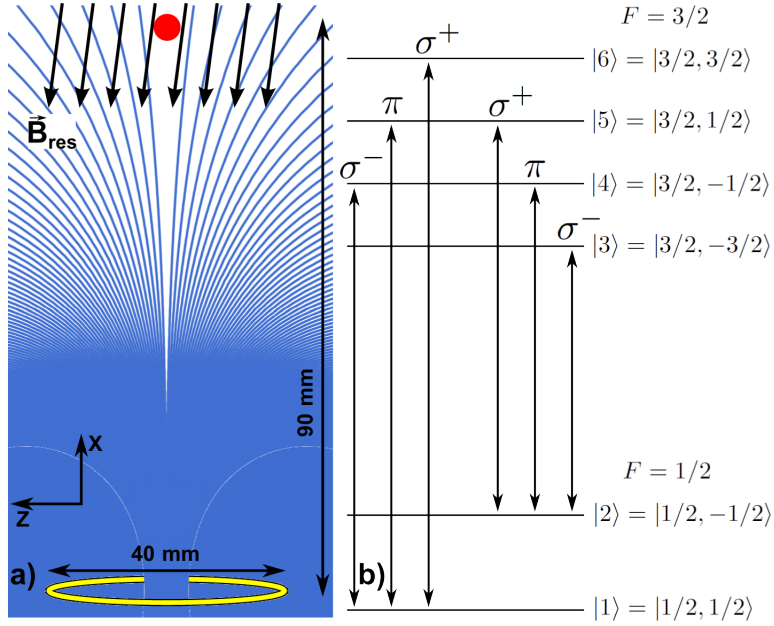
Figure 2.12: a) Magnetic field lines of the one loop antenna used for rf spectroscopy. The rf field shows some degree of inhomogeneity but far from the antenna, where atoms (large, red dot) are located. B_{res} is the uncompensated residual magnetic field. b) Rf transitions between Zeeman sublevels of the $2^2S_{1/2}$ level relevant to the magnetic field cancellation described in section 2.3.4. $|1\rangle$ to $|6\rangle$ at ~ 0 G correspond to $|F, m_F\rangle$ states.

2.2.4 RF antenna for spin manipulation

Radio frequency used for driving transitions between atomic or molecular levels proved to be an effective technique for spectroscopy and spin state manipulation (e.g. [73–75]) in ultracold samples. Notably, an "rf knife" [76] was used to evaporatively cool magnetically trapped atoms, an essential step in creating first Bose-Einstein condensates of rubidium [1] and sodium [2].

There are two relevant frequency ranges for the spin state manipulation in ^{6}Li. One is centered around the atomic hyperfine splitting, 228.205 MHz [77], and is used to drive transitions between hyperfine levels $F = 1/2$ and $F = 3/2$ of the $2^2S_{1/2}$ level. Depending on the orientation of the residual magnetic field B_{res} with respect to the field generated by the antenna, σ^-, σ^+ or π transitions can be driven
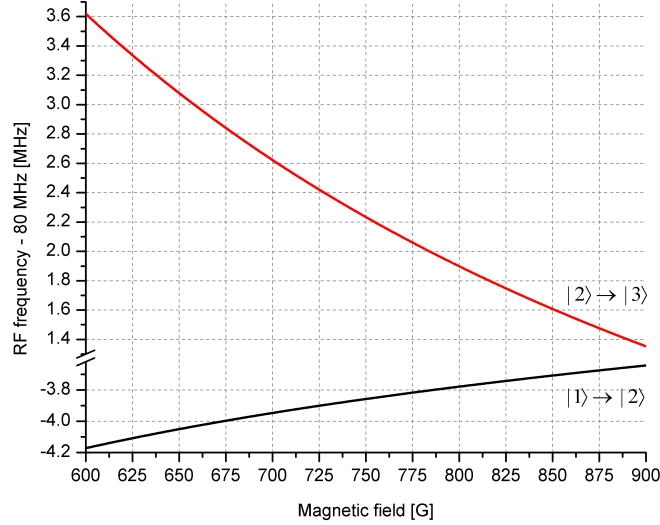
Figure 2.13: Frequency difference between magnetic sublevels within the $2^2S_{1/2}$ level for magnetic fields relevant to the rf spectroscopy of ^{6}Li in the BEC-BCS crossover regime. The numerical calculations are done based on [67, 77].

as shown in figure 2.12(b). It is important to note that no matter what is the relative orientation of the rf radiation and B_{res} there is always a transition available that is sensitive to the magnetic field [5]. This property can be used to probe the residual magnetic field enabling magnetic field cancellation (see section 2.3.4).

Magnetic field splits $F = 1/2$ and $F = 3/2$ into Zeeman sublevels, m_j, thus it is also possible to drive rf transitions between various m_j's, especially the lowest three which are separated by 76-84 MHz in the BEC-BCS crossover regime (Fig. 2.13). These transitions can be used to calibrate the magnetic field but, more importantly, rf provides a diagnostic tool for spectroscopic studies of Feshbach molecules [78] and BCS pairs [74].

The rf signal is derived from a direct digital synthesizer (DDS) driven by an

---

[5]For example, if the rf field is pointing along the residual magnetic field it induces π transitions. If, however, this transition is insensitive to the magnetic field then the rf spectroscopy of this level would not show any field dependent behavior.
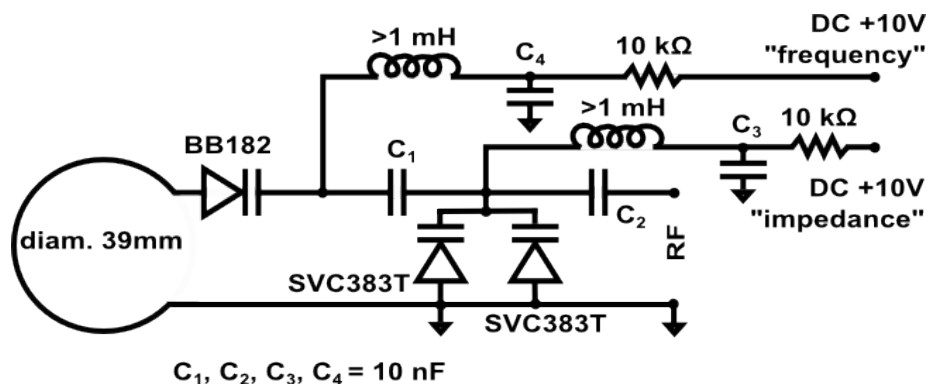
Figure 2.14: The design of the impedance matching circuit of the antenna used for driving rf transitions in ^{6}Li. The dc voltages corresponding to "frequency" and "impedance" are used to change the resonant frequency and the impedance of the circuit, respectively. Their values are set between 0 V and 10 V, depending on the rf frequency required by the experiments.

atomic clock frequency reference at 10 MHz, frequency doubled and then amplified to about 1 W. The spin manipulation is performed with a single loop antenna (R$\approx$ 2 cm) located 10 cm away from the trapped sample (see Fig. 2.2). An electronic circuit 2.14 is used to tune the resonance frequency (50 MHz to 250 MHz) as well as the impedance of the antenna coupled to the rf source, such that the reflections of the rf signal are minimized over the range of frequencies relevant to the experiments with ^{6}Li. Such reflections result in a lower power emitted by the antenna and in principle could damage the rf source. The design is inspired by an impedance matching circuit used in experiments where rf was used to associate Efimov trimers [79]

2.2.5 Photoassociation laser system

The high resolution photoassociation spectroscopy in the ultracold regime requires lasers systems that allow users to determine the frequency of measured transitions with sub-linewidth accuracy and precision. In alkali systems it usually means that the laser frequency needs to be known to within few MHz. This kind of accuracy is rarely achievable by direct measurements of the light frequency with wavemeters,

which usually are accurate only to within few tens of MHz. A relatively new [80], but already widespread method of measuring optical frequencies uses frequency combs where a cw laser used for spectroscopy is phase locked to a comb line [81] allowing accurate determination of its frequency. This approach, in principle, allows referencing multiple cw laser to one frequency comb assuring good relative phase coherence between these lasers even if their frequencies differ by tens of THz.

Frequency comb

The frequency comb is a femtosecond erbium-doped fiber laser oscillator based on nonlinear polarization rotation (spectrum centered at 1550 nm) that produces sub-100 fs pulses at a repetition rate of 125 MHz [37]. The free-space sections of the femtosecond oscillator and self-referencing optics are limited to make the system more robust, and less sensitive to the influence of the environment. The light is split into two amplified branches. The referencing branch is used to stabilize the offset frequency of the comb, f_o, and the repetition frequency, f_rep. It is spectrally broadened with a highly nonlinear fiber (HNF) for self-referencing the carrier-envelope offset frequency via an f–$2f$ interferometer. The signals containing f_o and f_rep are stabilized to separate rf synthesizers (Agilent 8648A and HP 8663A, respectively) using phase/frequency discriminators (PFDs) and loop filters to control the oscillator pump current and cavity piezoelectric transducer (PZT), respectively. These rf synthesizers are in turn referenced to a global positioning system (GPS) disciplined quartz oscillator (GPS 6-12 Frequency Standard, Menlo Systems GmbH). The second, "measurement", branch is also spectrally broadened with HNF and then split in two paths for referencing two Ti:Sapphire lasers. Here only 1.5–1.65 μm range is of importance for our applications, as opposed to the entire 1–2 μm region required for the referencing branch.

Titanium-sapphire lasers

High output power (100 mW and more) and narrow linewidth are typically required from lasers used for photoassociation spectroscopy. Moreover, these lasers need to be widely tunable because the theoretical predictions for the levels locations (at

35

least for lithium) are not always known precisely and frequency scans spanning hundreds of MHz are often necessary. We use two Coherent 899-21 ring cavity Ti:Sapphire lasers (called TS1 and TS2 throughout the thesis, see Fig. 2.15) with cavity optics suitable for lasing in the 760–830 nm range [6]. A Coherent Verdi V-18 pumps each Ti:Sapphire laser with 9 W of 532 nm light. For some experiments the relative phase coherence of the two lasers is important therefore both are locked to the same frequency comb.

As described in the previous section there are two "measurement" paths provided by the frequency comb and each is frequency doubled (second harmonic generation, SHG) in a separate periodically poled lithium niobate (PPLN) crystal and then overlapped with a respective cw laser. A heterodyne beat, f_{beat}, between the SHG comb, a cw laser and a stable rf reference signal is used to generate an error signal that after processing is fed back as a control signal such that each Ti:Sapphire is phase locked to a tooth of the frequency comb. The resulting frequency of a laser is

$$f_{laser} = m f_{rep} \pm f_o \pm f_{beat}, \tag{2.14}$$

where f_{rep}, f_{o} and f_{beat} are known radio frequencies, and m is a natural number on the order of 3×10^6. A preliminary frequency measurement using a standard wavemeter (with accuracy better than $f_{\text{rep}}/2$) enables the mode number m to be determined unambiguously.

Directly locking two lasers to the same frequency comb makes it impossible to change the relative frequency of the lasers over wide range. To circumvent this issue, for one of the lasers (TS1) the beam used for the beat note generation is frequency shifted by an AOM in a double pass configuration before overlapping with the comb. The technical details of this method will be discussed in the doctoral thesis of William Gunton and here we provide only a brief description. The laser is initially locked to a tooth n with the AOM and TS1 frequencies f_{AOM}^i and f_n^+, respectively. f_n^+ fulfills the condition $0 < f_n^+ - f_n < f_{\text{rep}}/2$, where f_n is the frequency of the tooth number n and f_{rep} is the repetition rate of the frequency comb. Because the beat note is fixed, changing the AOM frequency must result in the

---

[6]We would like to acknowledge Takamasa Momose and Mark G. Raizen for the long term loan of these lasers.
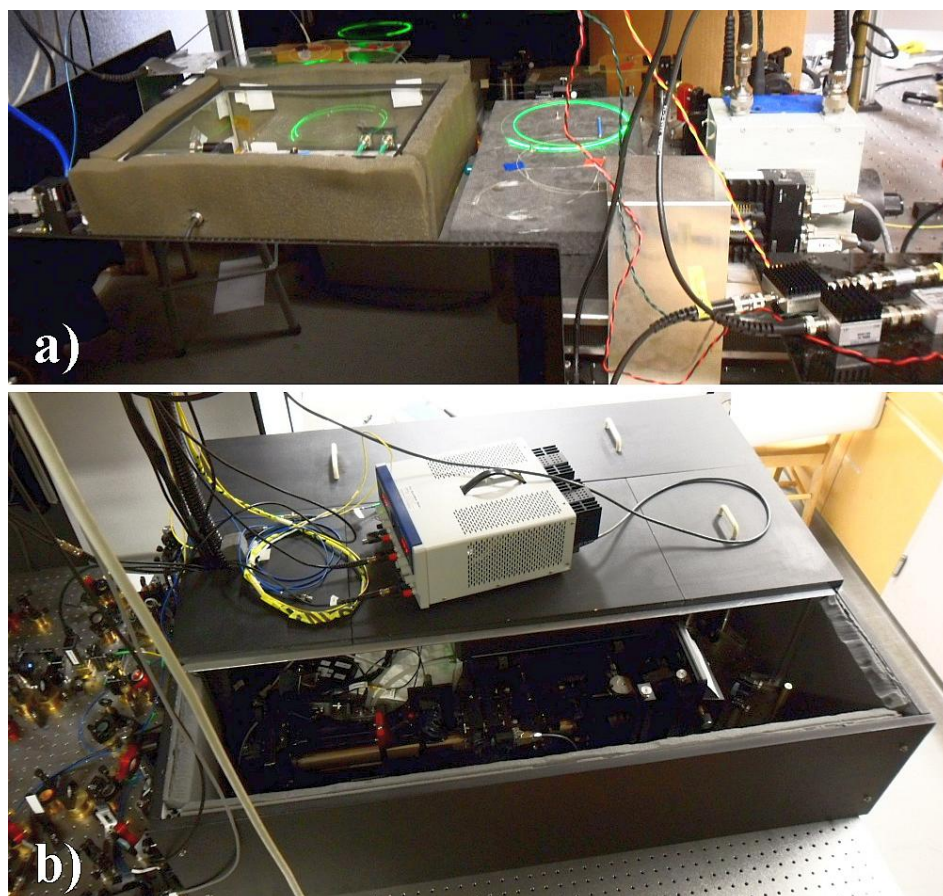
Figure 2.15: a) Fiber based frequency comb. The box to the left with the top off hosts the femtosecond oscillator. The green light comes from the erbium-doped fibers. b) Two Ti:Sapphire Coherent 899-21 ring lasers used for photoassociation are enclosed in a box with walls covered with a damping foam to reduce the influence of the temperature fluctuations and vibrations on the stability of the lasers. The accessible wavelength range is 760 nm-830 nm and is limited only by the cavity optics set.

change of the TS1 frequency. When the AOM is set to f_{AOM}^{f1} the laser frequency becomes f_{n+1}^- and $0 > f_{n+1}^- - f_{n+1} = -(f_n^+ - f_n)$. Then the sign of the error signal and, simultaneously, the AOM frequency are changed such that the laser becomes locked to the comb tooth $n+1$ with frequency f_{n+1}^- and the AOM is again set f_{AOM}^i. The AOM is further changed to f_{AOM}^{f2} such that the laser reaches f_{n+1}^+ (and $0 < f_{n+1}^+ - f_{n+1} = f_n^+ - f_n$) and the sign of the error signal is changed. Simultaneously the AOM is set to f_{AOM}^i. This completes the cycle and the laser becomes locked to the comb element $n+1$ with frequency $f_{n+1}^+ = f_n^+ + f_{\text{rep}}$. The steps repeat until the predetermined final frequency is reached. This method exploits the finite response time of the PID lockbox and allows continuous scanning of the frequency of TS1 over the entire mode-hop free range while keeping it locked to the comb at all times.

The absolute frequency uncertainty of the comb-referenced Ti:sapphires was verified by measuring the resonant frequencies of the D2 line at 780 nm (the $5s_{1/2} \rightarrow 5p_{3/2}$ transition) of ^{85}Rb atoms in a vapor cell and comparing them with their known values [82]. The test cell was enclosed in a μ–metal shield to limit the influence of stray magnetic fields on the transitions. The measured absolute frequencies differed from known values by amounts that depended on the probed transition - some where below, some were above the expected values. For this reason the difference, that never exceeded 600 kHz, was not attributed to systematic shifts due to the frequency comb but rather to the quality of the test cell setup. As a result, ± 600 kHz was taken as the uncertainty of the absolute frequency determination.

The beatnote measurement between the two Ti:Sapphires allowed us to determine the relative linewidth of the lasers. The two frequencies were set to differ by up to 10 GHz such that the width of the beatnote signal could be measured with a photodiode and an RF spectrum analyzer. The resulting width $\Delta \nu = 160$ kHz was constant over the entire operational range of the photodiode and it is justified to assume that it does not change when the frequency difference increases to 24 GHz (required for the binding energy measurements). The actual value of the beatnote determined directly with a spectrum analyzer agrees to ± 1 kHz with the value obtained by subtracting the frequencies of both lasers (calculated from measured rf frequencies f_{rep}, f_{o} and f_{beat}). This small difference is due to the resolution of the
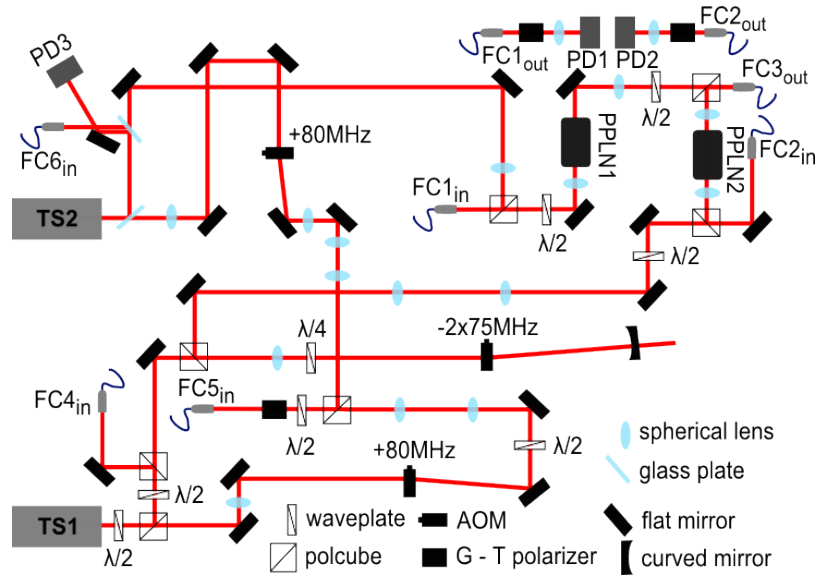
Figure 2.16: The distribution of the light derived from the Ti:Sapphire lasers TS1 and TS2. The light from TS1(TS2) is coupled into fibers (FCX$_{in(out)}$) for the wavelength measurement, FC4$_{in(out)}$(FC6$_{in(out)}$), beatnote with the comb, FC1$_{in(out)}$(FC2$_{in(out)}$), and photoassociation (PA), FC5$_{in}$. The PA light is shuttered with single pass AOMs. The double pass AOM is used for scanning as described in the text. PD1, PD2, PD3 are photodiodes.

frequency counter used in our setup.

Figure 2.16 shows how the Ti:Sapphire light is distributed in order to monitor the frequency and create beat notes to lock lasers to the frequency comb. The light from both lasers is overlapped on a polarizing beam splitter cube, sent through a Glan-Thompson polarizer to assure that both beams have the same polarization, coupled into a single mode, polarization maintaining fiber and sent to the experimental table. Before overlapping with the dipole trap (see Fig. 2.9) the output of the fiber is filtered once again with a Glan-Thompson polarizer to assure a well defined polarization of the photoassociation light. The beams follow the exact same path as the IPG dipole trap and are focused such that the $1/e^2$ radius is about 50 μm.

2.3 Preparation of ultracold quantum gases

This section discusses the performance of our experimental setup and steps that lead to the production of ultracold samples required for high-precision photoassociation spectroscopy. Furthermore, we demonstrate that both molecular Bose-Einstein condensate of Feshbach molecules and the so-called Bardeen-Cooper-Schrieffer pairs in a strongly-interacting, degenerate Fermi gas can be created using a relatively simple design of the vacuum chamber and the atomic source.

The development of our experimental setup is always a "work in progress", especially regarding the dipole traps (Section 2.2.3). The data presented in this section should be treated as a snapshot of the capabilities of our setup at a point in time and an indication of the *minimum* performance level that we are able to achieve.

2.3.1 Trapping performance

An exhaustive search in the pump (Δv_p) and repump (Δv_r) detunings for a range of axial magnetic field gradients ($\partial_z|B|$) between 10 to 70 G cm^{-1} [7] was performed to optimize the MOT numbers at an oven current of 9.5 A (corresponding to an oven temperature of 625 K). Table 2.1 contains a summary of the optimum MOT parameters. The highest atom number we were able to trap (at $I_{oven} = 9.5$ A) was $(8 \pm 2) \times 10^7$ atoms at $\partial_z|B| = 35$ G cm^{-1} and using a detuning from resonance of $\Delta v_p = -8.5\,\Gamma$ and $\Delta v_r = -5.1\,\Gamma$ for the pump and repump light, respectively. The saturation intensities given in table 2.1 are calculated for the case of an isotropic pump field with equal components in all three possible polarizations [82]. In addition, the lithium interaction was assumed to include all of the allowed $2^2P_{3/2}$ excited state levels due to our large detuning relative to the excited state hyperfine splittings.

Fig. 2.17 shows the behavior of this oven loaded lithium MOT at an axial field gradient of 35 G cm^{-1}. The loading rate (R), the lifetime or inverse loss rate (γ_{loss}^{-1}) of both the MOT and ODT, and the steady state atom number (N_∞) in the MOT are shown as a function of the oven temperature. These parameters were determined by fitting the loading curve of the MOT to the solution, $N(t) = N_\infty(1 - e^{-\gamma_{loss}t})$

---

[7]The axial magnetic field gradient for our coils is 5.8 G/cm/A

Table 2.1: Optimal parameter settings for the MOT at an oven current of 9.5 A (oven temperature of 625 K): Wavelength and width of the D2 line, saturation intensities (assuming isotropic light polarization), pump and repump intensities along all three principle axes, relative detunings of the pump and repump light ($\Delta \nu_{\mathrm{p}}$ and $\Delta \nu_{\mathrm{r}}$), axial magnetic field gradient, initial load rate, decay rate, and steady state atom number. Table taken from [50].

	^{6}Li
$\lambda_{\mathrm{D_2,vac}}$ (nm)	670.977
$\Gamma/2\pi$ (MHz)	5.87
I_{sat} (mW cm^{-2})	3.8 [82]
$I_{\mathrm{p}}/I_{\mathrm{sat}}$	21
$I_{\mathrm{r}}/I_{\mathrm{sat}}$	16
$\Delta \nu_{\mathrm{p}}$ (Γ)	-8.5
$\Delta \nu_{\mathrm{r}}$ (Γ)	-5.1
$\partial_z|B|$ (G cm^{-1})	35
R	$(1.3 \pm 0.3) \times 10^6$ s^{-1}
N_∞	$(8 \pm 2) \times 10^7$

of the differential equation $\dot{N} = R - \gamma_{\mathrm{loss}}N$. The steady state number is then the product of the loading and inverse loss rates, $N_\infty = R/\gamma_{\mathrm{loss}}$.

This model does not include a two-body loss term to model particle loss due to light assisted collisions between cold atoms within the MOT, and therefore the loss term we report is an overestimate of the MOT losses due only to collisions with the residual background vapor or atoms from the hot atomic beam. In addition, because the Li–Li* collision cross section (with one atom in the excited state) is much larger than for ground state collisions, the loss rate for the excited state atoms in the MOT will be significantly larger due to collisions with fast moving Li atoms in the atomic beam. These two effects make the MOT lifetime only an estimate of the expected lifetime for the ensemble in the CODT.

For comparison, the inverse loss rate (i.e. lifetime) of a 50 μK deep CODT is also provided for a few of the oven current settings. Since the MOT is significantly deeper than the CODT, the MOT trap loss rate due to background vapor collisions is expected to be smaller [83, 84]. In addition, residual losses from the CODT will occur due to spontaneous emission and evaporation losses. Thus the lifetime in a
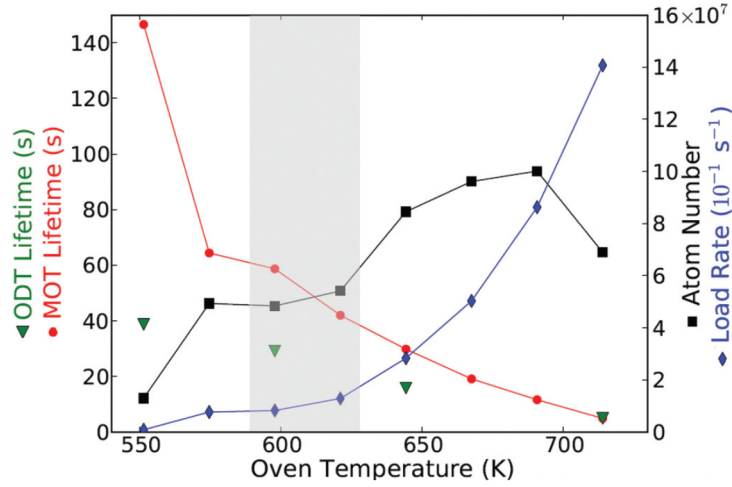
Figure 2.17: The atom loading rate (diamonds), the MOT lifetime (circles), the ODT lifetime (triangles), and the steady state atom number (squares) of the MOT are shown as a function of the oven temperature with parameter values as defined in Table II. We typically operate the source in the shaded region (between 590 K and 625 K), where a good compromise is found between a sufficiently large MOT atom number and a long ODT trap lifetime. The trend lines serve only as a guide for the eye. Figure taken from [50].

shallow CODT will always be an overestimate of the total background collision rate.

At low oven current settings where the loss rate is dominated by collisions with atoms or molecules other than Li atoms, the MOT lifetime is, as expected, much larger than the lifetime in the CODT. Whereas at high oven current settings where the loss rate is primarily determined by the collisions with fast moving atoms in the Li atomic beam, the MOT lifetime is similar to the CODT lifetime. The longest inverse loss rate measured for the CODT was on the order of 40 s (at an oven current of 8 A and a temperature of 550 K) corresponding to a background vapor pressure of approximately 10^{-10} Torr [53, 83, 84]. As the temperature of the oven increases so does the captured flux and the loss rate. At a current of $I_{oven} = 11$ A (corresponding to an oven temperature of 680 K), the steady state atom number is maximized. There exists a clear tradeoff between the inverse loss rate of the
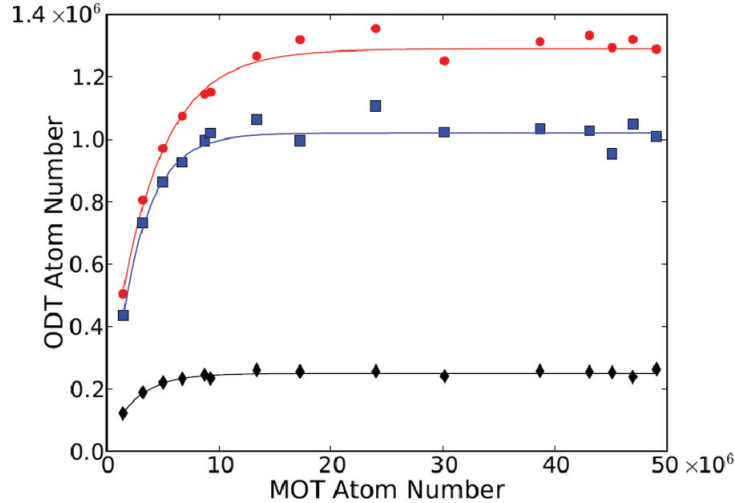
Figure 2.18: Atom number transferred into the CODT versus atom number in the MOT. Plotted are the initial atom number in the high power CODT at 200 W total power (circles), the atom number in the high power CODT after evaporation to 100 W total with 50 W per beam (squares), and the atom number transferred into the low power CODT (diamonds) for various initial MOT atom numbers. Figure taken from [50].

lithium MOT and the steady state atom number, and by running the oven at 625 K (with $I_{oven} = 9.5$ A) instead of 680 K, the inverse loss rate can be increased by more than a factor of four with only a factor of two reduction in the trapped number. We note that the MOT performance is similar to that previously reported in Ref. [24]. The primary difference is that here the oven aperture is 30% larger and a portion of the MOT light is sent counter propagating to the oven flux. This additional slowing beam enhances the loading rate by a factor of two.

To reach degeneracy, atoms need to be transferred from the MOT into a trap that allows evaporative cooling, like an optical dipole trap (as discussed in Section 2.2.3). The atomic cloud trapped in the MOT is compressed and cooled by increasing the axial magnetic field gradient from 35 to 64 G cm^{-1}, lowering the intensity and shifting the frequency of both the pump and repump light to 10 MHz below resonance. During this compression and cooling phase, a CODT of 200 W total power is turned on and, in less than 10 ms, up to 10% of the ^{6}Li atoms are

transferred into the CODT. Fine adjustments of the MOT position to optimize its overlap with the CODT are essential to achieving efficient transfer and are made by adding a small (5 to 10 G) homogeneous magnetic field that shifts the magnetic quadrupole center during the compression phase. This field is generated by three pairs of large (30 cm diameter) "compensation" coils for independent control of the field along each of the three orthogonal spatial axes.

During the compression phase, we observe extremely rapid trap losses (with trap lifetimes on the order of a few ms) due to light assisted collisions and hyperfine relaxation, and we therefore optically pump to the lower hyperfine state ($F = 1/2$) during the transfer by extinguishing the repump light 400 μs before the pump light. As a result an almost equal population of the two sub-levels of the lower hyperfine state: $|1\rangle \equiv |F = 1/2, m_F = 1/2\rangle$ and $|2\rangle \equiv |F = 1/2, m_F = -1/2\rangle$ is produced. After the MOT light is extinguished, the CODT beam power is ramped down linearly in time to 100 W total (50 W per beam) in 100 ms while applying a homogeneous magnetic field of 300 G produced by the same coils used to generate the quadrupole magnetic field for the MOT. Rapid thermalization occurs because of the large collision rate between the $|1\rangle$ and $|2\rangle$ states at 300 G [85]. At the end of this forced evaporation stage, there are approximately 10^6 atoms remaining at a temperature of 200 μK (verified by a time-of-flight expansion measurement). Finally, a second dipole trap is turned on and as a result about 25% of atoms are trapped in low power CODT (see Section 2.2.3). This transfer is done to avoid ensemble heating observed in the SPI laser CODT and allows further forced evaporative cooling to much lower powers and thus ensemble temperatures.

In the experiments that originally led to the creation of degenerate gases (and the data presented in this Section) the trap depth was lowered using a series of linear ramps of different duration, for a total evaporation time of 4 s.[8] We use an additional "gradient" coil, concentric with the top main magnetic coil, to add a magnetic field gradient to both compensate for the residual magnetic field gradient of our main magnetic coil pair and to provide a magnetic force on the atoms equal and opposite to the gravitational force. This additional coil is essential for the production of quantum degenerate samples as in this case the evaporation must

---

[8]We have recently successfully reduced the total evaporation time to about 1.3 s without any measurable decrease in the evaporation efficiency thus reducing the data collection time.
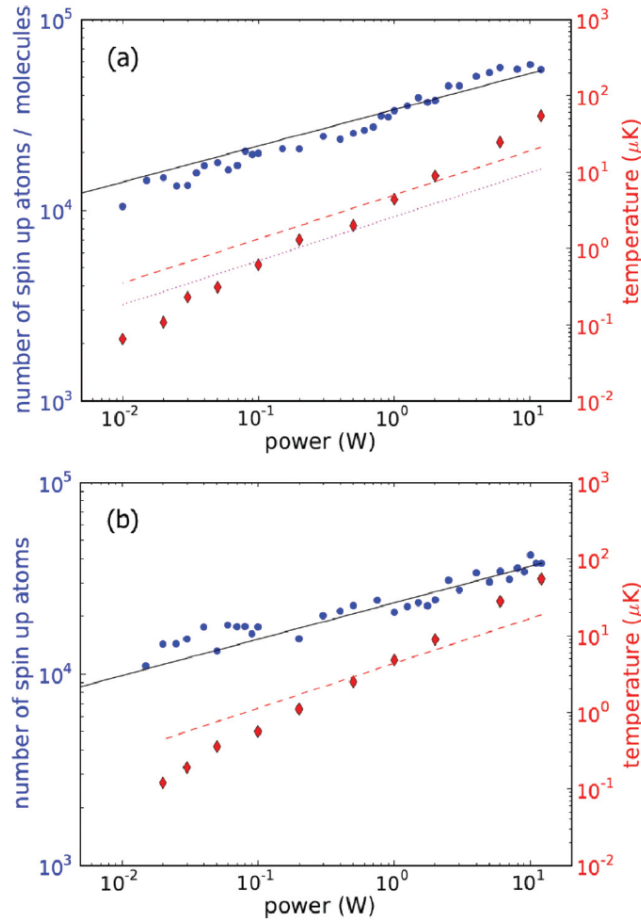
Figure 2.19: Ensemble temperature (diamonds) and particle number (circles) as a function of the CODT laser power (i.e.,trap depth) in the final forced evaporation stage at (a) B = 800 G (below the FR) and (b) B = 900 G (above the FR). The number of "spin-up" atoms (atoms in the $|1\rangle$ state) is detected at these high magnetic fields by absorption imaging. For the evaporation below the FR, when the temperature is well below the binding energy all of the atoms form FR molecules and the number detected in the $|1\rangle$ state corresponds to the total FR molecule number. The solid line indicates the expected particle number for an efficient evaporative cooling. The dashed line indicates the Fermi temperature for the $|1\rangle$ component at each power computed from the particle number and the trap frequencies. In (a) the dotted line shows the critical temperature for BEC for the molecules. Figure taken from [50].

45

be continued to the very lowest optical trap depths where gravitational sagging significantly compromises the confinement.

Figure 2.19 shows the result of evaporation both below and above the Feshbach resonance center at $B = 832.18$ G. Both the ensemble temperature and particle number are shown as a function of the trap depth during the final forced evaporation stage. The solid line indicates the expected particle number N at various trap depths U obtained from the scaling law

$$\frac{N}{N_i} = \left(\frac{U}{U_i}\right)^{3/[2(\eta'-3)]}$$

(2.15)

under the assumption that the ratio η of the trap depth U to thermal energy $k_B T$ is ~ 10 (typical for evaporative cooling in optical traps). Here i denotes initial conditions and $\eta' = \eta + (\eta - 5)/(\eta - 4)$. The detailed discussion of the scaling laws for evaporative cooling in time-dependent optical traps, with emphasis on ^{6}Li, can be found in Ref. [86].

2.3.2 Molecular BEC

For evaporation at $B = 800$ G, we observe the formation of FR molecules when the temperature nears the molecule binding energy (250 nK), and at the end of the evaporation ramp, we observe 2×10^4 molecules at a temperature of 70 nK. To image the molecular cloud, we reduce the magnetic field from 800 to 690 G and release the ensemble from the dipole trap. After some fixed time-of-flight (TOF) expansion, we then take an absorption image of the molecular cloud. The spin-up (or spin-down) component of this very weakly bound molecule can be imaged as if it were a free atom since the binding energy is far below the excited state width.

At the end of the evaporation ramp at $B = 800$ G the molecular gas is strongly interacting and deep in the hydrodynamic regime. In particular, the molecule-molecule s-wave scattering length is predicted to be on the same order as the atom-atom scattering length ($a_{mol} = 0.6a$ [87]), and the atom-atom scattering length at B=800 G is $a > 5000a_B$ [88]. In order to reduce the interaction strength during the TOF expansion and thus increase the visibility of the characteristic bimodal distribution of the mBEC, the TOF is performed at 690 G [72].

Figure 2.20 shows a series of absorption images and resulting horizontal density profiles of these Feshbach molecules after a 3 ms TOF expansion at a magnetic field of $B = 690$ G for different final ensemble temperatures. The wings of the profiles are fit to a Gaussian function and the bimodal character of the density profile is evident for temperatures below the critical temperature for Bose Einstein condensation. For the coldest molecular cloud, we show in Fig. 2.20 the absorption images after different free expansion times. The in-situ shape of the molecular cloud (image taken at 0 ms) has the anisotropic shape of the CODT, and the cloud anisotropy reverses during the time-of-flight expansion. This anisotropy reversal is expected for a BEC of non-interacting particles due to the larger confinement frequency along the vertical direction in these images. However, even at the magnetic field of $B = 690$ G, the molecules are still strongly interacting, and the inversion of the aspect ratio of the molecular cloud can also be the result of hydrodynamics [71, 89].

2.3.3 Strongly interacting degenerate Fermi gas

One of the first experimental signatures of fermionic pairing above the FR where the atom-atom interactions are attractive was the observation of the pairing gap in a strongly interacting Fermi gas of ^{6}Li atoms by radio frequency spectroscopy [74]. While the correct interpretation of these spectra requires a full accounting of both the final-state and trap effects to understand the contributions from the pairing-gap, pseudogap, and no-gap phases, nevertheless, it is a simple measurement that can be intuitively understood and that provides a clear signature of pair formation (both so-called "pre-formed" and condensed pairs) [90].

Here we perform the final evaporation stage at $B = 839.2$ G, just above the FR, to different final trap depths producing different final ensemble temperatures. At the end of this evaporation, we apply radio frequency (rf) radiation for 1 second that transfers atoms in state $|2\rangle$ to the unoccupied $|3\rangle$ state. We monitor the loss of atoms from state $|2\rangle$ by state-selective absorption imaging, and in Fig. 2.21 we plot the loss as a function of the rf radiation frequency detuning δ from the free atom resonance at 81.34 MHz (corresponding to the energy splitting between the $|2\rangle$ and $|3\rangle$ states at this magnetic field including the difference in the mean field interaction
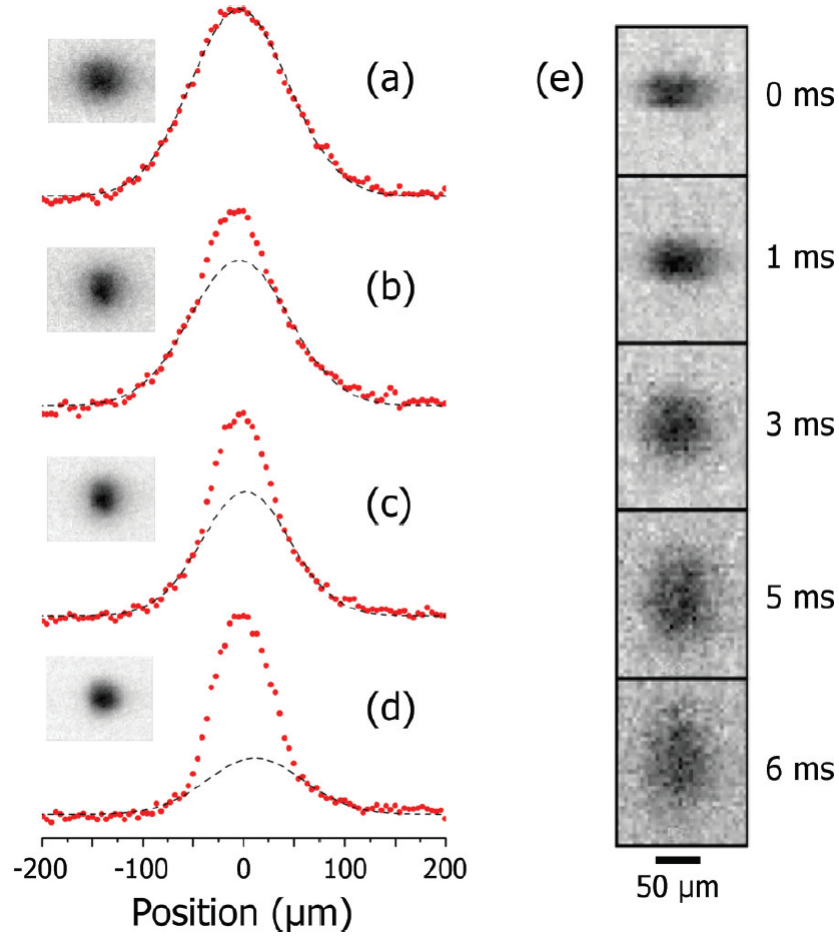
Figure 2.20: Absorption images and resulting horizontal density profiles of $^6\mathrm{Li}_2$ Feshbach molecules after a 3 ms time of flight expansion at a magnetic field of $B = 690$ G for different ensemble temperatures, (a) $T = 710$ nK ($T//T_\mathrm{C} \sim 1.2$), (b) $T = 230$ nK ($T//T_\mathrm{C} \sim 0.9$), (c) $T = 110$ nK ($T/T_\mathrm{C} \sim 0.8$), (d) $T = 65$ nK ($T/T_\mathrm{C} \sim 0.6$). The wings of the profiles are fit to a Gaussian function and the bimodal character of the density profile is evident for temperatures well below the critical temperature. For the coldest molecular cloud (d) we show in (e) the absorption images after different free expansion times. The in-situ shape of the molecular cloud (image taken at 0 ms) has the anisotropic shape of the CDT, and the cloud anisotropy reverses during the time-of-flight expansion. Figure taken from [50].
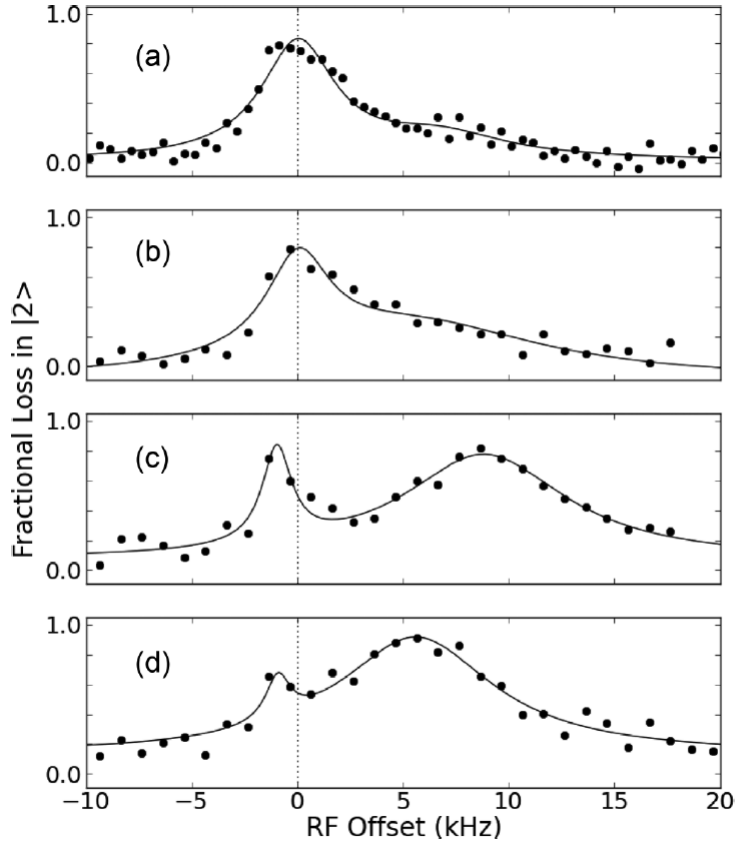
Figure 2.21: RF spectroscopy of the degenerate Fermi gas at 840 G. Initially only free atoms peak is present (a) but as the final temperature of the sample decreases the atoms form BCS-like pairs which presence shows up as an additional loss feature [(b) to (d)]. Figure taken from [50].

energies). We note that when the loss of atoms from state $|1\rangle$ is monitored instead of the loss from state $|2\rangle$ the spectrum is the same. This is likely due to the loss of atoms in state $|1\rangle$ due to the collisional instability of these mixtures when $|3\rangle$ state atoms are present [91, 92].

In Fig. 2.21(a) and (b) where the temperature is above the pair dissociation temperature, T^*, the rf-spectrum shows a single resonance peak at a frequency offset of zero. This corresponds to the energy required to flip the spin of an unpaired atom. In (c) and (d), the ensemble temperature is $T < T^*$, and a second maximum

appears at higher energy. Unpaired $|2\rangle$ atoms undergo the transition at a zero offset whereas an additional energy due, in part to the pairing gap, must be added to flip those bound to a $|1\rangle$ state atom as a pair. Here the temperature is slightly above the critical temperature for pair condensation, and these so-called pre-formed pairs exist in what is known as the "pseudogap" region [90, 93]. In Fig. 2.21(d) where the temperature is lower than in (c), the ratio of pairs to free atoms is larger as expected; however, the gap energy is less because the Fermi temperature in (d) is smaller than in (c). In addition, the unpaired spin flip energy is shifted to a negative offset in (c) and (d). This is because we produce a colder ensemble by evaporating to a lower trap depth and this changes the atomic density producing a different differential mean field interaction energy for the unpaired atom transition [73].

2.3.4 Fermi gas at 0 gauss

The most spectacular experiments with fermionic ^{6}Li have been performed near either $B = 543.3$ G [88, 94] or $B = 832.18$ G [85] Feshbach resonance but there has been very little work done on the weakly interacting gas at 0 G beyond initial experiments reporting fermionic degeneracy [66, 95, 96]. This regime does not seem to be of any significant interest, possibly because its main advantage, vanishing interactions between states $|1\rangle$ and $|2\rangle$, can be also reproduced at the zero crossing of the s-wave scattering length ($B = 527.5$ G [88, 97]), while benefiting from the rapid control of interactions as the magnetic field is varied in the vicinity of the crossing.

Our experiments are the first that perform systematic photoassociation spectroscopy of ^{6}Li in a dipole trap. This allows us to remove magnetic field as a source of systematic shifts, a step impossible if photoassociation spectroscopy is done in a MOT. This is especially important for high precision studies of molecular structure using dark states.

The sample confined by the IPG CODT is evaporatively cooled at 300 G to a final trap depth at which the spectroscopy measurements are done. The MOT coils and the gradient coil are then turned off, while simultaneously a uniform magnetic field is applied with a set of three pairs of compensation coils (the same that are used to move the MOT for dipole trap loading). This additional uniform field is
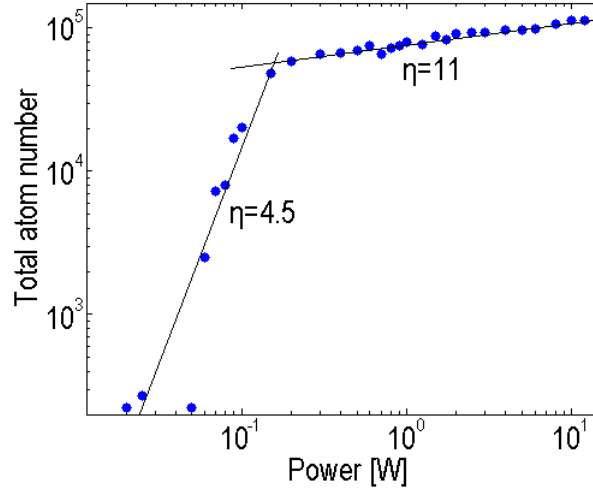
Figure 2.22: The evaporation curve at 0 G. The atom number drops suddenly when the trap becomes too shallow to support atoms against gravity. This sets a limit for the evaporation ramp and thus the atom number and temperature that can be achieved with the degenerate Fermi gas at 0 G. Two different evaporation trajectories are clearly visible: the steeper one corresponds to an inefficient evaporation with $\eta = 4.5$.

used to compensate for any residual magnetic fields that might be present in the system, including the magnetic field of Earth. Fitting the equation 2.15 to the data obtained for the evaporation at 300 G and subsequent turn off of the magnetic field (shown in Fig. 2.22) indicates that the process is very efficient for a range of final trap depths, with $\eta = U/k_B T = 11$.

At low laser powers the trap depth decrease due to the gravitational potential becomes significant. This results in spilling of atoms out of the trap and severely limits the atom number at the lowest ODT powers. Turning off the gradient coil effectively corresponds to a sudden decrease of the trap depth which is a sum of optical and gravitational potentials as well as a contribution from the magnetic gradient. Past certain point switching to 0 G and turning off the gradient coil dramatically limits the trap depth leading to atom loss by spilling, seen as a change in the slope of the evaporation curve in Fig. 2.22, corresponding to $U/k_B T = 4.5$. We avoid this problem at non-zero magnetic fields by using a gradient coil throughout
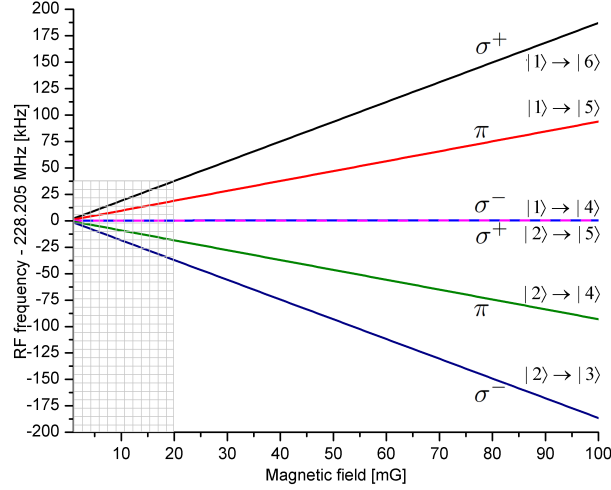
Figure 2.23: The frequency of the σ^+, σ^- and π RF transitions between Zeeman sublevels of F=1/2 and F=3/2 manifolds of the $2^2S_{1/2}$ ground state. The states $|i\rangle$ correspond to $|F, m_F\rangle$ as shown in figure 2.12, Section 2.2.4. The grid indicates the magnetic field region below 20 mG - relevant to the compensation of the day-to-day magnetic field drift in the experimental setup.

the entire experimental cycle but it is not feasible at 0 G because the field could not be canceled across the entire cloud, distorting precision spectroscopy measurements. Fig.2.19 and Fig. 2.22 show the striking difference between evaporation and imaging at high magnetic fields, and evaporation at 300 G with subsequent switching to 0 G.

Cancellation of the residual magnetic field

As a result of the regular operation of the experimental setup there is always some residual magnetic field present even if all the sources are off. This is mainly due to the magnetic field of Earth but it is likely that the magnetization of some elements of the setup also plays a role. Even a small magnetic field B of some tens of mG can change the energies of the hyperfine levels in the $2^2S_{1/2}$ state according to

$$\Delta E = \frac{\mu_B}{\hbar} g_F m_F B, \tag{2.16}$$

52

where $\mu_B = 9.27400968(20) \times 10^{-24}$ J/T is Bohr magneton, m_F the projection of the total atomic angular momentum F on the quantization axis and g_F for the $2^2S_{1/2}$ state is given by

$$g_F = g_J \frac{F(F+1) - 5/4}{2F(F+1)} + g_I \frac{F(F+1) + 5/4}{2F(F+1)} \qquad (2.17)$$

with $g_J = 2.002301$ and $g_I = -0.0004476540$ being the electronic and nuclear g-factor of the $2^2S_{1/2}$ state, respectively. This property is exploited to characterize the magnetic field by driving σ^+, σ^- and π rf transitions between $|1\rangle$, $|2\rangle$ and $|F = 3/2, m_F\rangle$ Zeeman sublevels as shown in figure 2.12, Section 2.2.4).

After major changes to the setup like coil replacement or dipole trap rearrangement the residual magnetic field can reach few hundreds of mG. Rf spectroscopy of the sample reveals multiple peaks [Fig. 2.24(a)] corresponding to transitions shown in Fig. 2.23. A sequence: "change magnetic field using compensation coils and then perform rf spectroscopy" if repeated many times lets us track the behavior of the peaks by comparing the measured frequencies with theoretical calculations. In practice, the $|2\rangle \rightarrow |3\rangle$. transition is followed because it is the most sensitive to the magnetic field. As the residual field approaches 0 G the levels become degenerate and there is only one transition, corresponding to the 228.205 MHz $2^2S_{1/2}$ hyperfine splitting. A signal as shown in Fig. 2.24(b) is treated as "good enough" because further cancellation becomes very time consuming without providing any obvious benefits. We believe that a residual field of 15 mG is acceptable for our applications.
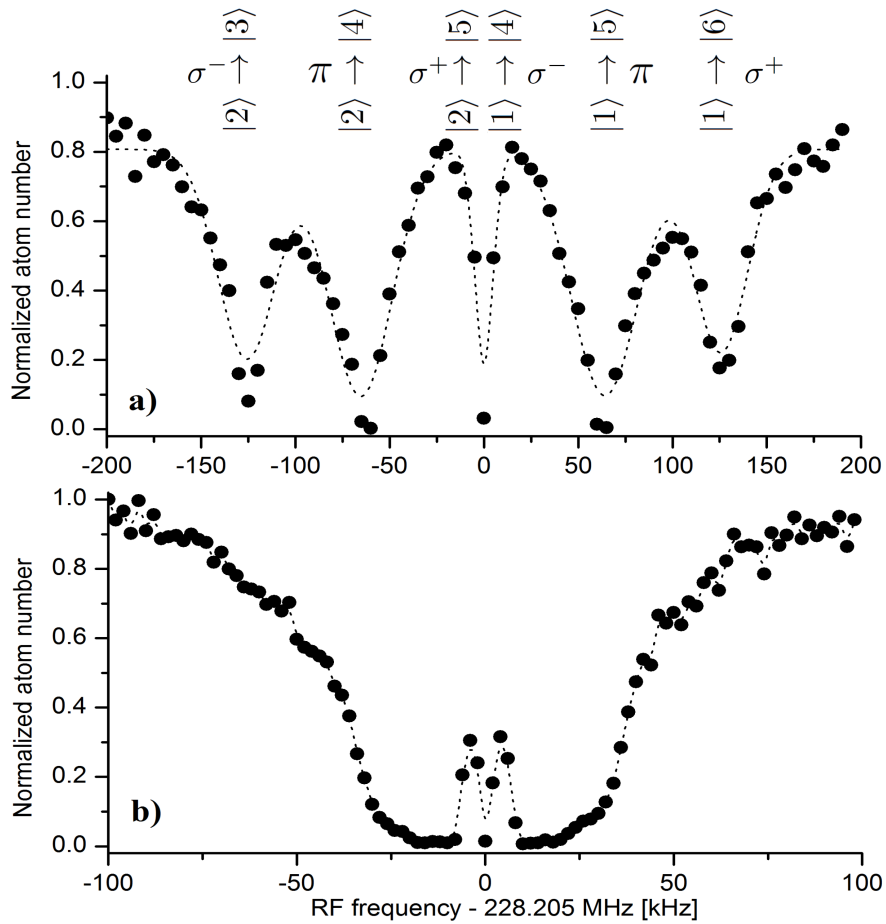
Figure 2.24: Loss induced by driving σ^+, σ^- and π RF transitions between Zeeman sublevels of $2^2S_{1/2}$ level. a) The magnetic field sources are off but the residual field is not canceled. Signals like this, here corresponding to about 130 mG, are typically observed after major changes to the setup, like the magnetic coils replacement or rearrangement of the dipole trap. Zeeman splitting between sublevels can be resolved. b) At very low magnetic fields all transitions become nearly degenerate. From the shape of the loss feature the residual magnetic field could be estimated to be below 15 mG.

Chapter 3

Single color photoassociation

The main results of this Chapter have been published in

- **M. Semczuk**, *X. Li, Xuan, W. Gunton, M. Haw, N. S. Dattani, J. Witz, A. K. Mills, D. J. Jones and K. W. Madison, "High–resolution photoassociation spectroscopy of the $^6Li_2$ $1^3\Sigma_g^+$ state.", Phys. Rev. A **87**, 052505, May (2013)* [49].

- *W. Gunton,* **M. Semczuk**, *N. S. Dattani and K. W. Madison, "High–resolution photoassociation spectroscopy of the $^6Li_2$ $A(1^1\Sigma_u^+)$ state.", Phys. Rev. A **88**, 062510, December (2013)* [51].

Single color photoassociation spectroscopy has proven to be a very powerful technique for precise measurements of binding energies of cold molecules [98], pairing in the BEC-BCS crossover regime [99], optical control of Feshbach resonances in bosonic [100] and fermionic [101] species. Recently, coherent one-color photoassociation of a Bose-Einstein condensate of ^{88}Sr was demonstrated by Yan *et al.* [102].

Under certain conditions adding a photon of a proper energy to a colliding pair of atoms can result in association of atoms and formation of an excited molecule. The required energy is the difference between the energies of the excited level and the initial state (molecules or colliding atoms). In the ultracold regime the photoassociation relies mainly on the s-wave collisions between atoms because at sub-μK temperatures higher partial waves do not play a significant role. In this work a spin mixture of ^{6}Li is used because the photoassociation rate of a spin polarized sample of fermions is highly suppressed at ultra-low temperatures. This is due to the Pauli exclusion principle that prevents a single component Fermi gas from interacting via s-wave collisions and all higher partial wave collisions are suppressed by an amount proportional to T^2 [103].

The experimental work on the single color photoassociation spectroscopy of $^6\text{Li}_2$ preceding the research presented in this thesis has been done with atoms in magneto-optical traps (MOT) [104, 105] and was limited to the $c(1^3\Sigma_g^+)$ and $A(1^1\Sigma_u^+)$ potentials. In MOTs atoms are trapped in the two hyperfine levels of the $2S_{1/2}$ electronic ground state. Additionally, MOT temperatures are typically on the order of 400 μK and are high enough for p-wave (and sometimes higher order) collisions to take place. This allows access to multiple ro-vibrational levels in the excited potentials but at the same time these traps suffer from hard to control systematic effects induced by the presence of high magnetic field gradients and the MOT cooling light.

In the experiments presented in this work we confine a two-component degenerate Fermi gas in an optical dipole trap, as described in Chapter 2. With no magnetic field present the only systematics come from the frequency uncertainty of the photoassociation (PA) laser and the ac Stark shift of the initial and final levels introduced by the dipole trap and the photoassociation laser. The frequency uncertainty of the PA laser is estimated as discussed in Section 2.2.5. The ac Stark shifts are quantified by performing spectroscopy at different trap strengths and for different photoassociation laser powers. Finally, the measurements are extrapolated to the field free values.

Figure 3.1 shows seven lowest lying potentials of ^6Li. The specific vibrational levels in the five potentials that can be probed with our PA laser system are listed in Table 3.1. It is worth noting that except for the c- and A-states these potentials have never been studied with photoassociation spectroscopy. In fact, the experimental data (including other techniques) is rather scarce and it is not clear to what degree one can trust the theoretical predictions in the context of photoassociation spectroscopy. The characterization of these levels is expected to be very time consuming and for the time being is not a part of our research program. Long term, however, these levels might be important because it is very likely that they could be used for direct absorption imaging of ultracold ground state molecules as has been demonstrated in the case of KRb [106]. In this Chapter only two potentials, $c(1^3\Sigma_g^+)$ and $A(1^1\Sigma_u^+)$, are studied, mainly because these are the most relevant to our long term goals. The theoretical predictions guiding the initial measurements were expected to be accurate to $\sim$1 GHz for the range of frequencies covered in
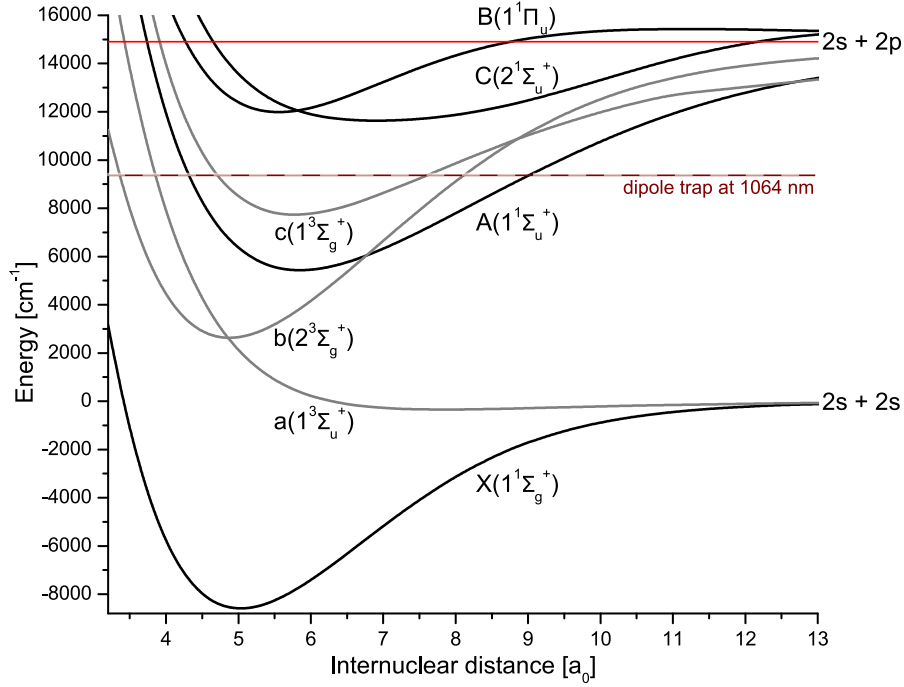
Figure 3.1: Seven lowest lying singlet (black) and triplet (grey) potentials of $^6Li_2$. The shaded area corresponds to the tuning range of our PA laser system, 760 to 830 nm. The energy corresponding to the dipole trap laser (1064 nm) is highlighted in maroon (dashed line). The $2s + 2P$ asymptote is shown in red, corresponding to the $D1/D2$ atomic transition. Figure based on numerical form of potentials published in [107]

Table 3.1: Potentials and the corresponding vibrational levels that can be probed by photoassociation spectroscopy in the range of 760-830 nm.

Molecular potential	$c(1^3\Sigma_g^+)$	$b(1^3\Pi_u)$	$A(1^1\Sigma_u^+)$	$B(1^1\Pi_u)$	$C(2^1\Sigma_g^+)$
Vibrational levels	$20 - 26$	$32 - 38$	$29 - 35$	$0 - 4$	$0 - 4$

this work, making the initial search easier than it would be with other potentials shown in Table 3.1.

The measurements presented in this chapter probe not only the previously unexplored range of the $c(1^3\Sigma_g^+)$ and $A(1^1\Sigma_u^+)$ potentials but also enter a new regime of atomic densities and temperatures, not addressed in previous photoassociation experiments with ^6Li. For these reasons in the initial measurements we employed

all the available techniques that we believed would increase the photoassociation rate:

- the atoms were trapped in a cross beam to increase the density of the cloud (reaching 5×10^{11} cm^{-3}),

- the temperature was kept relatively high (about 20 μK),

- the maximum available photoassociation power was used and the atoms were exposed to the light for as long as it was reasonable (at times up to 10 s),

- for the c-state the process took place at 800 G to enhance the collision rate due to the proximity of a broad Feshbach resonance (FR) at 834 G and then the features were traced back to 0 G. The method resulted in very broad (several hundred of MHz) loss features, significantly broader than expected based on the predicted natural lifetimes of these levels [108]. To access rotational levels $N' = 0, 2$ in the excited c-state the collisions in the initial state needed to have a rotational number $N = 1$, corresponding to the p-wave collisions, which are strongly suppressed at sub-μK temperatures. For this reason the photoassociation rate to $N' = 0, 2$ was negligibly small and had to be enhanced by increasing the p-wave collision rate in the proximity of a p-wave Feshbach resonance at 185 G [109]. The p-wave enhancement should also work for the singlet A($1^1\Sigma_u^+$) state.

The initial search for the photoassociation features and p-wave enhanced photoassociation measurements was performed with a Ti:Sapphire laser locked to its cavity and laser frequency was determined by a commercial wavemeter (Bristol 621A-NIR) with an absolute accuracy of 60 MHz and a shot-to-shot repeatability (i.e. precision) of 10 MHz in the frequency range of this work. All the measurements (except for the p-wave enhanced photoassociation) were refined with the photoassociation laser locked to the frequency comb (see Section 2.2.5).

3.1 A note about Feshbach resonances

The properties of magnetic Feshbach resonances [110, 111] are extensively used in experiments with ultracold atoms. Since the initial observation in a Bose-Einstein

condensate of sodium [112] they have become indispensable for control of interactions between alkali atoms. The associated phenomenon of formation of loosely bound states near such resonances, so-called Feshbach molecules, resulted in the production of Bose-Einstein condensates of weakly molecules of ^{6}Li [113] and ^{40}K [114], and proved to be an essential step in obtaining near degenerate ground-state molecules of KRb [23]. Recently, magnetic Feshbach resonances have been also observed in dipolar gases of chromium [115], erbium [116] and dysprosium [117], further extending the scope of systems with magnetically tunable interactions.

The literature on Feshbach resonances in ultracold gases is very extensive, including an excellent review by Chin *et al.* [118]. For the purpose of this thesis only a brief discussion is presented.

A Feshbach resonance occurs when the energy of the bound molecular state in the closed channel (e.g., ground state molecular potential) approaches the energy of the scattering state in the open channel (colliding atoms or molecules). When the corresponding magnetic moments are different, the energy difference between the open and the closed channel can be controlled via magnetic field, leading to a magnetically tuned Feshbach resonance. In ^{6}Li, *s*-wave Feshbach resonances located at magnetic fields $\sim$ 543 G and 832.2 G arise from the $v'' = 38$, $N = 0$ rovibrational level in $X(1^1\Sigma_g^+)$ potential with nuclear spin $I = 0$ or $I = 2$ (Fig. 3.2). In the vicinity of a resonance located at B_0 with a width Δ the *s*-wave scattering length a changes as a function of the magnetic field B

$$a(B) = a_{bg}\left(1 - \frac{\Delta}{B - B_0}\right),\tag{3.1}$$

where a_{bg} is the background (off-resonant) scattering length associated with the interaction potential between colliding atoms. In this formalism both a_{bg} and Δ can be both positive and negative. The scattering length associated with the Feshbach resonance vanishes at a magnetic field $B_{cross} = B_0 + \Delta$. The parameters characterizing the broad Feshbach resonance in ^{6}Li occurring at $B_0 = 832.18(8)$ are $a_{bg} = -1582(1)a_0$ and $\Delta = -262.3(3)$ G, with $a_0 = 0.529177$ nm [85].

The tunability of the scattering length with the magnetic field is often exploited
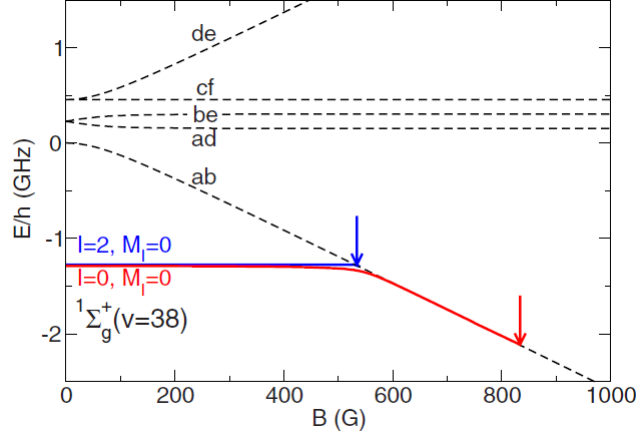
Figure 3.2: Coupled-channels calculation of ^{6}Li$_2$ bound states, which give rise to *s*-wave Feshbach resonances at threshold. The two-atom states (dashed line) are indicated by their quantum numbes $(F_1, m_{f_1}; F_2, m_{f_2})$ and are: $ab = (1/2, 1/2; 1/2, -1/2)$, $ad = (1/2, 1/2; 3/2, -1/2)$, $be = (1/2, -1/2; 3/2, 1/2)$, $cf = (3/2, -3/2; 3/2, 3/2)$, $de = (3/2, 1/2; 3/2, -1/2)$ while the bound states (blue and red lines) are labeled by the molecular quantum numbers S and M_L, where M_L is the projection of total angular momentum on the quantization axis. The arrows indicate the locations of the 543 and 832.2 G Feshbach resonances, where the binding energy of a threshold bound state equals 0. While the low B field $I = 2$ $X(1^1\Sigma_g^+)(v"=38)$ level retains its spin character as it crosses threshold near 543 G, the $I = 0$ level mixes with the entrance channel and switches near $\approx$550 G to a bound level with *ab* spin character, eventually disappearing as a bound state when it crosses threshold at 832.2 G. The figure and caption adapted from Chin *et al.* [118].

to increase the elastic scattering cross-section

$$\sigma_e = \frac{4\pi a^2}{1 + k^2 a^2},\tag{3.2}$$

which enhances the elastic collision rate. This leads to faster thermalization and as a consequence enables rapid and efficient evaporative cooling of atoms confined in a dipole trap. Equation 3.2 holds true for *s*-wave scattering of distinguishable particles, e.g different spin states of an atom as is the case in our experiments. As

is shown in this chapter, such an enhancement was crucial in the early stages of the photoassociation spectroscopy experiments where it was used to enhance the photoassociation rate [54, 108].

The scattering process (here for distinguishable particles) is characterized by its cross-section

$$\sigma(k) = \frac{4\pi}{k^2} \sum (2l+1) \sin^2 \delta_l(k) \tag{3.3}$$

and can be described by a scattering phase shifts δ_l of different partial waves l. δ_l incorporate the effect of the whole potential on the collision event. In the ultracold regime the relative momentum $\hbar\mathbf{k}$ of colliding atoms typically tends to zero and for the van der Walls potential one finds that $\tan \delta_l$ varies as k and k^3 for s $(l = 0)$ and p $(l = 1)$ waves, respectively [119]. For the s-wave collisions near the resonance a more precise statement relating $\tan \delta_0$ and k is often required:

$$k \cot \delta_0(E) = -1/a + \frac{1}{2} r_0 k^2. \tag{3.4}$$

Equation 3.4 is called the effective range expansion and r_0 is the effective range - a parameter that takes into account that the scattering phase shift and thus the collision cross section depends on the collision energy and the $k \neq 0$ condition is not strictly fulfilled in experiments.

p-wave Feshbach resonances

For the case of p-wave resonances in fermionic systems the scattering in spin polarized samples is possible, as opposed to s-wave case. For ^{6}Li with $f = 1/2$, one expects three p-wave Feshbach resonances corresponding to three possible combinations of $|f = 1/2, m_f\rangle + |f = 1/2, m'_f\rangle$, denoted as (m_f, m'_f). They appear at fields $B = 159.1$ G, 185.1 G and 215 G corresponding to $(1/2, 1/2)$, $(1/2, -1/2)$ and $(-1/2, -1/2)$, respectively [109, 120], and are relatively narrow (~ 0.4 G). Their presence is a consequence of crossing of the free atom threshold by the $v'' = 38$ level in the $X(1^1\Sigma_g^+)$ $(S = 0)$ molecular potential with a rotational quantum number $N'' = 1$ (see Fig. 3.3). As a result of the symmetrization requirements of the two-body wave function this state has a nuclear spin $I = 1$ [120].

At ultracold temperatures p-wave collisions are strongly suppressed and the
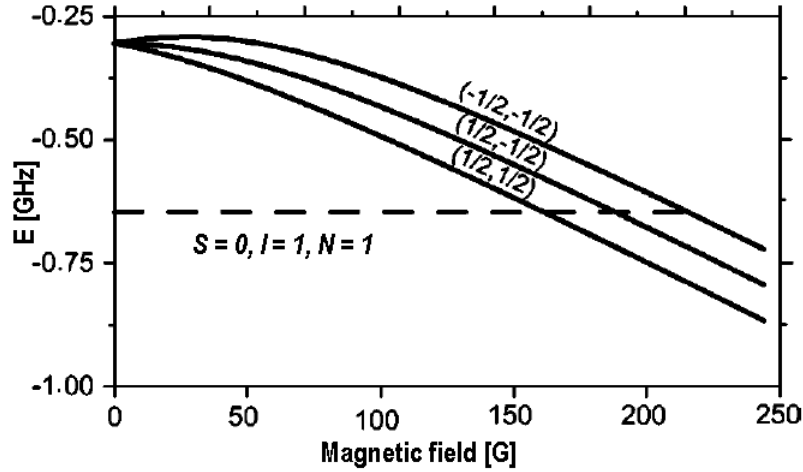
Figure 3.3: Coupled channels calculation of *p*-wave binding energies of $^6\text{Li}_2$, which give rise to Feshbach resonances at threshold. The two-atom states (full line) are indicated by their quantum number (m_{f_1}, m_{f_2}), while the bound state (dashed line) is labeled by the molecular quantum numbers S, I, and N. The figure and caption taken from [120].

only method to enhance them is by tuning the field to one of the resonances. We exploited this property to perform single color photoassociation to the rotational molecular levels $N = 0$ and 2 that are inaccessible if atoms collide in the *s*-wave channel. To our knowledge, this is the first example of FOPA (Feshbach-Optimized Photoassociation) [54] for a *p*-wave Feshbach resonance.

3.2 Theory of diatomic molecules

Molecules in the $1^3\Sigma_g^+$ and $A^1\Sigma_u^+$ excited states are characterized by the Hund's case "b" coupling scheme in which the total electronic (nuclear) spin $\vec{S} = \vec{s}_1 + \vec{s}_2$ ($\vec{I} = \vec{i}_1 + \vec{i}_2$) is completely uncoupled from the internuclear axis. Here $\vec{s}_j$ ($\vec{i}_j$) is the electronic (nuclear) spin of atom "*j*". This occurs when $\Lambda = 0$, the projection of the orbital angular momentum of the electrons along the internuclear axis is zero, and there is therefore no axial magnetic field to couple the total spin to the axis. For "Σ" states, the orbital angular momentum of the electrons is zero and therefore Λ is always identically zero; however, even in some cases where $\Lambda \neq 0$,

especially for light molecules, the coupling is sufficiently weak that Hund's case "b" is still the appropriate scheme [121]. The total angular momentum, apart from the spin, is $\vec{K} \equiv \vec{N} + \vec{\Lambda}$, the vector sum of $\vec{\Lambda}$ and the rotational angular momentum of the nuclei $\vec{N}$. Therefore for "Σ" states $\vec{K} = \vec{N}$, and thus $\vec{K}$ is perpendicular to the internuclear axis. The total spin of the molecule is $\vec{G} = \vec{S} + \vec{I}$ and is a good quantum number so long as the hyperfine interaction and spin-rotational couplings are small. The total spin combines with the total angular momentum apart from spin $\vec{K}$ to result in the total angular momentum including spin as $\vec{J} = \vec{K} + \vec{G}$. For electric dipole radiation, the selection rule is that $\Delta J = 0, \pm 1$ with the restriction that $J = 0 \nleftrightarrow J = 0$. In addition, under the emission or absorption of a photon the parity of the electronic orbital must change $(+ \leftrightarrow -)$ and for a homonuclear molecule, the symmetry of the coordinate function under interchange of the two nuclei must change from symmetric to anti-symmetric or vice versa $(g \leftrightarrow u)$. In the present scenario of Hund's case "b" coupling, the spin is so weakly coupled to the other angular momenta that both quantum numbers S and K are well defined and we have in addition the selection rules $\Delta S = 0$ (or equivalently $\Delta G = 0$) and therefore $\Delta K = 0, \pm 1$ with the restriction that $\Delta K = 0$ is forbidden for $\Sigma \rightarrow \Sigma$ transitions. Since this chapter is only concerned with transitions to the $A^1\Sigma_u^+$ and $c(1^3\Sigma_g^+)$ excited states, we have that $\Delta N = \pm 1$ and $\Delta G = 0$.

3.2.1 Initial state of colliding atoms

In this work, we only consider collisions between two ^{6}Li atoms, which are composite fermions (consisting of 9 fermions: 3 protons, 3 neutrons, and 3 electrons), and we note that the 2-body eigenstates, composed of a spin part and an orbital part, must be antisymmetric upon exchange of the two atoms. The consequence is that only certain spin states are possible given a particular orbital state. An important example of this constraint imposed by exchange symmetry is that the two-body position wave function (sometimes called the "coordinate function" or orbital state) must be antisymmetric for a collision between two fermions in the same spin state (for which the spin wave function is manifestly symmetric). Thus a spin polarized Fermi gas can only have odd partial wave collisions (p-, f-, h-wave, etc...) corresponding to odd values of the rotational angular momentum of the complex

($N = 1, 3, 5 \ldots$), which are antisymmetric with respect to atom exchange. For a gas composed of two distinct spin states, even partial wave collisions can occur (s-, d-, g-wave, etc...) so long as the spin wave function is antisymmetric upon atom exchange. The ability to turn off s-wave collisions by spin polarizing the gas is a useful feature of our system that we use to validate our assignment of the PA lines.

The total spin angular momentum of the initial unbound molecular state is given by the vector sum of the f quantum numbers for the isolated atoms: $\vec{G} = \vec{f_1} + \vec{f_2}$. Here $\vec{f_1} = \vec{s_1} + \vec{i_1}$. In our experiment, the atoms are optically pumped to the lowest hyperfine state before being exposed to the photoassociation light. Therefore we have that $f_1 = f_2 = \frac{1}{2}$ and there are two allowed values of the total spin: $G = 0, 1$. Certain values of G (specifically $G = f_1 + f_2, f_1 + f_2 - 2, \ldots$) are associated with spin states symmetric with respect to interchange of the atoms while the orbital states with even values of N are symmetric under the interchange of the atoms. Therefore all even partial wave collisions ($N = 0, 2, 4, \ldots$) have a total spin of zero ($G = 0$) and all odd partial wave collisions ($N = 1, 3, 5, \ldots$) have a total spin of one ($G = 1$).

Following [122], the initial antisymmetric unbound molecular state can be written in the $|S, M_S; I, M_I\rangle$ basis states, where M_S and M_I are projections of the total electronic end nuclear spin on the quantization axis, respectively. A general expression that holds also for non-zero magnetic fields B

$$|\Psi_B\rangle = \sin\theta_+ \sin\theta_- |1, 1; 1, -1\rangle + \sin\theta_+ \cos\theta_- \left(\frac{1}{\sqrt{3}} |0, 0; 0, 0\rangle - \frac{2}{\sqrt{3}} |0, 0; 2, 0\rangle \right)$$

$$\tag{3.5}$$

$$+ \cos\theta_+ \sin\theta_- \left(\frac{1}{\sqrt{3}} |0, 0; 0, 0\rangle + \frac{1}{\sqrt{6}} |0, 0; 2, 0\rangle - \frac{1}{\sqrt{2}} |1, 0; 1, 0\rangle \right)$$

$$+ \cos\theta_+ \cos\theta_- |1, -1; 1, 1\rangle$$

at $B = 0$ simplifies to

$$|\Psi\rangle = \sqrt{2/3} \left(\sqrt{1/3} |1, 1; 1, -1\rangle + \sqrt{1/3} |1, -1; 1, 1\rangle - \sqrt{1/3} |1, 0; 1, 0\rangle \right) \tag{3.6}$$
$$+ \sqrt{1/3} |0, 0; 0, 0\rangle.$$

Here $\sin\theta_\pm = 1/\sqrt{1+(Q^\pm+R^\pm)^2/2}$, $Q^\pm = (\mu_N+2\mu_e)B/a_{hf} \pm 1/2$, $R^\pm = \sqrt{(Q^\pm)^2+2}$, μ_N and μ_e are, respectively, the nuclear and electronic magnetic moments, and a_{2S} is the hyperfine constant.

The state $|\Psi\rangle$ at $B = 0$ is a linear superposition of a singlet and a triplet state, therefore allowing photoassociation spectroscopy of excited molecular states with both singlet and triplet characters. For the purpose of this thesis it is useful to rewrite Eq. 3.6 in the molecular basis $|N,S,I,J,F\rangle$

$$\begin{aligned}|\Psi\rangle &= \sqrt{2/3}|\text{Triplet}\rangle + \sqrt{1/3}|\text{Singlet}\rangle \\ &= \sqrt{2/3}|0,1,1,1,0\rangle + \sqrt{1/3}|0,0,0,0,0\rangle.\end{aligned} \tag{3.7}$$

3.2.2 Final excited molecular states

The final state is a molecule in the $c(1^3\Sigma_g^+)$ or $A^1\Sigma_u^+$ potentials. For the triplet state, the total electronic spin is well defined ($S = 1$) and the "gerade" symmetry signified by a sub-script "g" denotes that all states with an even rotational quantum number ($N = 0,2,4,\ldots$) are symmetric under the interchange of the two nuclei [104]. Because the electronic spin is well defined and fixed for this excited state, we now consider interchanging just the *nuclei* while leaving the electrons untouched. There are three possible values of the total nuclear spin ($I = 0,1,2$) since the nuclear spin of each atom is $i = 1$. Similar to the symmetry of G, states with $I = i_1+i_2, i_1+i_2-2\ldots$ (corresponding here to $I = 0$ and $I = 2$) are symmetric with respect to interchange of the nuclei whereas the $I = 1$ state is antisymmetric. Since the nuclei are *bosons* the total wave function must be symmetric under the interchange of the nuclei. Putting this together, we have that the even (odd) values of I occur with even (odd) values of N.

The final singlet state $A^1\Sigma_u^+$ has a well defined total electronic spin $S = 0$. The sub-script "u" refers to the "ungerade" symmetry, therefore all states with an even rotational quantum number ($N = 0,2,4,\ldots$) are antisymmetric under the interchange of the two nuclei [104]. Due to the bosonic character of the final ^{6}Li molecules the reasoning as presented for the triplet state leads to the conclusion that $I = 0,2$ correspond to states with odd N and $I = 1$ corresponds to states with even N. The total spin angular momentum quantum number G can take on all values

Table 3.2: Allowed rotational levels and corresponding nuclear spin configurations for $^6\text{Li}_2$ molecules in the limit that spin-spin and spin-rotation couplings are small enough that G is a good quantum number.

State	Electronic spin	Nuclear spin	Allowed rotational states	Total Spin
ground states				
-	-	-	$N = 0,2,4\ldots$	$G = 0$
-	-	-	$N = 1,3,5\ldots$	$G = 1$
excited states				
$c(1^3\Sigma_g^+)$:	$S = 1$	$I = 0$	$N = 0,2,4\ldots$	$G = 1$
		$I = 1$	$N = 1,3,5\ldots$	$G = 0,1,2$
		$I = 2$	$N = 0,2,4\ldots$	$G = 1,2,3$
$A(1^1\Sigma_u^+)$:	$S = 0$	$I = 0$	$N = 1,3,5\ldots$	$G = 0$
		$I = 1$	$N = 0,2,4\ldots$	$G = 1$
		$I = 2$	$N = 1,3,5\ldots$	$G = 2$

between and including $|I + S|$ and $|I - S|$.

The possible quantum numbers for the ground and excited states are tabulated in Table 3.2. For a ground state s-wave collision ($N = 0$) we find that there is only one allowed value for the total spin: $G = 0$. From an initial state with $N = 0$ and $G = 0$, we see that there is only one possible transition to an excited "Σ" state: $(N = 0, G = 0) \to (N' = 1, G' = 0)$. For a ground state p-wave collision, the initial state is $(N = 1, G = 1)$ and there are two possible transitions to the excited triplet state: $(N = 1, G = 1) \to (N' = 0, G' = 1)$ and $(N = 1, G = 1) \to (N' = 2, G' = 1)$. In both cases, there are two possible values of the total nuclear spin: $I = 0$ or 2.

The initial energy of the colliding complex is lower than the hyperfine center of gravity by a factor of $2a_{2S}$. This extra energy must be added to the D1 transition frequency when determining the binding energies of each vibrational level in the studied states.

3.3 Spectroscopy of the $c(1^3\Sigma_g^+)$ potential

The measurements of the seven vibrational levels $v' = 20 - 26$ of the $1^3\Sigma_g^+$ excited state of $^6\text{Li}_2$ molecules cover a completely unexplored spectral range for this
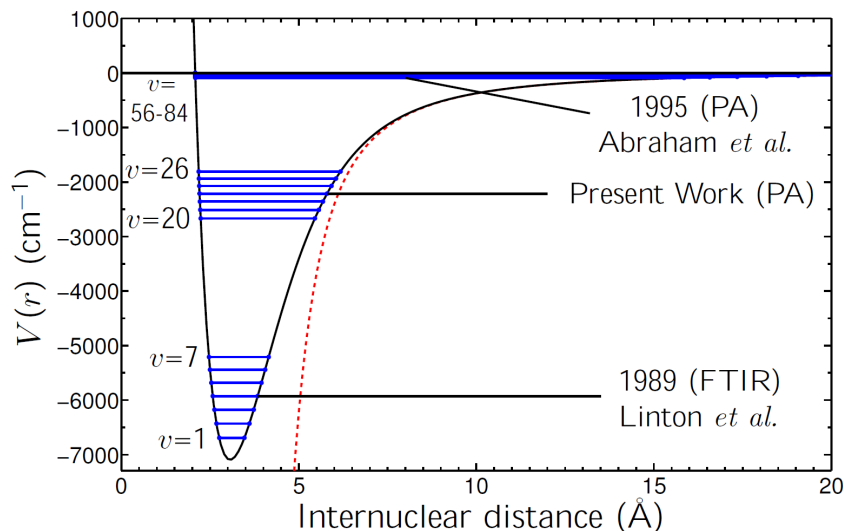
Figure 3.4: The $1^3\Sigma_g^+$ potential studied in this work (solid line). The horizontal lines indicate experimentally measured bound levels for $^{6,6}\text{Li}_2$. The present work includes high resolution data from seven new vibrational states ($v' = 20$ to 26) including the $N' = 0, 1, 2$ rotational states in each case. The theoretical long-range potential according to [126] is shown by the dotted line. Figure taken from [49].

molecule. As shown in Fig. 3.4 we bridge a gap between measurements of the deeply lying $v' = 1 - 7$ levels by Fourier transform spectroscopy (of both $^{7,7}\text{Li}_2$ and $^{6,6}\text{Li}_2$ molecules) [123, 124] and measurements of the binding energies of levels $v' = 62 - 90$ of $^{7,7}\text{Li}_2$ and $v' = 56 - 84$ of $^{6,6}\text{Li}_2$ by photoassociation of atoms in a magneto-optic trap [125].

The experiments are performed in an ensemble prepared as described in Section 2.3.4 using the trap arrangement shown in Fig. 2.11a. At the end of the final evaporation step the magnetic field is lowered to a very small value and PA light from a single-frequency, tunable Ti:sapphire laser beam illuminates the atomic cloud for a certain exposure time. The PA light is a single beam that propagates co-linearly with one of the arms of the lower-power CDT and is focused to a waist ($1/e^2$ intensity radius) of $50\ \mu$m. The light is linearly polarized and aligned along the direction of the bias magnetic field used for the measurements of p-wave Fes-

hbach enhanced PA. When the bias field is off, there persists a residual magnetic field below 400 mG. For these experiments, the power of the PA light is up to 100 mW corresponding to an intensity of 1270 W/cm^2. When the photon energy $h\nu_{PA}$ equals the energy difference between the unbound state of a colliding atomic pair and a bound molecular excited state, molecules form at a rate proportional to the atom-atom collision rate and atoms are subsequently lost from the trap. This loss occurs because the excited state molecule either decays into the unbound continuum of two free atoms with sufficient energy to be lost from the shallow CDT or it spontaneously decays into a bound state molecule which is not detected in our atom number measurement. The probability of this latter event (called fluorescence) can be quite high when exciting particular vibrational levels in the $1^3\Sigma_g^+$ excited state [127]. The excited lithium molecules gain kinetic energy on the order of the recoil energy $E_{rec} = p^2/2M = h^2\nu^2/(2Mc^2)$ as a result of the decay to the ground state. Here, p is the momentum of the emitted photon with frequency ν, M is the mass of a lithium molecule, h and c are the Planck's constant and the speed of light, respectively. In units of temperature we typically have $E_{rec} \sim 1-4\mu K$, depending on the final state of the ground state molecule. Such energy is usually below the trap depths used in the experiments $(1 - 10\mu K)$ therefore the fluorescence decays of the excited molecules result in *trapped* ground state molecules. After the atoms are illuminated by the photoassociation light for some exposure time, the number of *atoms remaining* is determined by an absorption image of the cloud immediately after the extinction of the CDT.

We observed that the PA spectrum of each vibrational level had associated with it three narrow (below 10 MHz FWHM) features distributed across a range of 0.7 GHz as shown in Fig. 3.5. Figure 3.6 shows a higher resolution scan of the second feature shown in Fig. 3.5. In order to reduce as much as possible the thermal broadening and the inhomogeneous AC Stark shift produced by the optical dipole trapping potential, these data were obtained in a very shallow trap $(U_{trap}/k_B \sim 8\mu K)$ and an ensemble temperature of 800 nK, a temperature well below the Fermi temperature for this two component Fermi-gas $(T/T_F = 0.4)$. We then verified that these PA resonances arise from collisions between atoms in states $|1\rangle$ and $|2\rangle$ by using a state-selective resonant pulse of light to remove all atoms in either of the two states. The spin purification was done at the end of the preparation
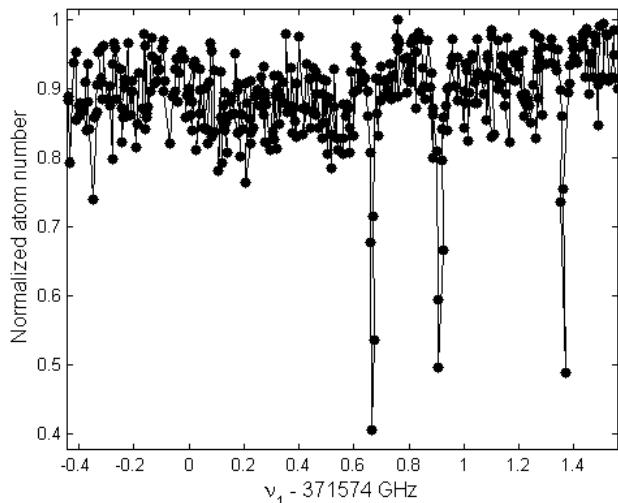
Figure 3.5: Normalized ^{6}Li atom number as a function of photo-association laser energy $h\nu_{PA}$ after a 2 second hold time with a residual magnetic field below 400 mG and a PA laser intensity of $I_{PA} = 635$ W/cm^2. These three resonances correspond to a transition from an initial unbound molecular state with $N = 0, G = 0$ to the $v' = 21$ vibrational level of the $1^3\Sigma_g^+$ excited state with $N' = 1$, $G' = 0$. The ensemble temperature was 15 μK.

sequence, and we observed the absence of these atom loss features with either one of the states removed. The spin purification was performed at a high magnetic field (typically 700 G), where the optical transitions from the $|1\rangle$ and $|2\rangle$ states to the excited $2p_{3/2}$ manifold are well separated. In addition, the field is sufficiently large to disrupt the hyperfine coupling and these transitions become approximately "closed" such that the excited state atom returns to the original ground state with a large probability allowing each atom to scatter many photons during the pulse and subsequently leave the trap. To rule out the absence of these loss features due to a simple reduction of the density, we observed a reappearance of the PA features when using an incoherent mixture of the $|1\rangle$ and $|2\rangle$ states with the same total number of particles and temperature as the ensembles after spin purification. Given that p-wave collisions are dramatically suppressed at these temperatures and that these PA loss features were visibly enhanced by the s-wave FR, we inferred

Table 3.3: Experimentally measured PA resonances for *s*-wave collisions in an incoherent mixture of the $|1\rangle$ and $|2\rangle$ states of ^{6}Li. These three PA resonances correspond to a transition from an initial unbound molecular state with $N = 0$, $G = 0$ to the vth vibrational level of the $1^3\Sigma_g^+$ excited state with $N' = 1$. The spin-spin and spin-rotation coupling split the excited state into three sub-levels producing the three PA features corresponding to quantum numbers $(N' = 1, J' = 1)$, $(N' = 1, J' = 2)$, and $(N' = 1, J' = 0)$ respectively. The absolute uncertainty in each of these measurements is ± 0.00002 cm^{-1} (± 600 kHz).

v'	1st cm^{-1} GHz	2nd cm^{-1} GHz	3rd cm^{-1} GHz
20	12237.17755	12237.18587	12237.20126
	366861.3537	366861.6031	366862.0645
21	12394.39726	12394.40535	12394.42039
	371574.6820	371574.9245	371575.3754
22	12546.06767	12546.07552	12546.09025
	376121.6465	376121.8818	376122.3234
23	12692.17316	12692.18080	12692.19509
	380501.7789	380502.0079	380502.4363
24	12832.70080	12832.70820	12832.72214
	384714.6916	384714.9134	384715.3313
25	12967.64150	12967.64862	12967.66219
	388760.1018	388760.3254	388760.7322
26	13096.99114	13096.99804	13097.01125
	392637.9166	392638.1235	392638.5195

that they arise from *s*-wave collisions between atoms in states $|1\rangle$ and $|2\rangle$. Thus, they correspond to a transition from an initial unbound molecular state with $N = 0$, $G = 0$ to an excited state with $N' = 1, G' = 0$ (assuming G is a good quantum number). The locations of these three features for each of the seven vibrational levels is provided in Table 3.3.

3.3.1 p-wave Feshbach resonance enhanced photoassociation

For each of the vibrational states we probed in the c-state potential, we located the PA resonances to the N'=0 and N'=2 rotational levels associated with p-wave
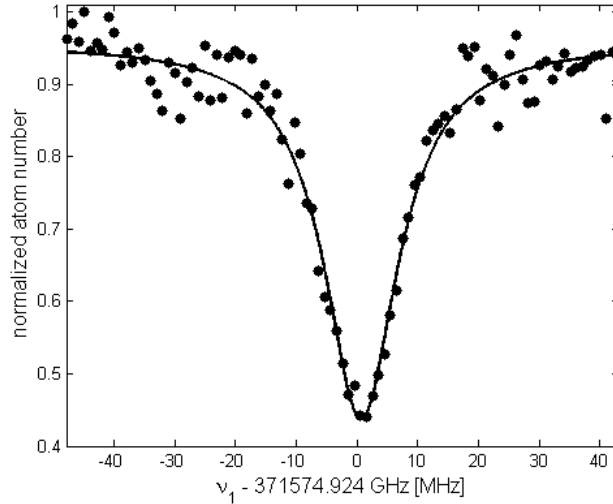
Figure 3.6: High resolution scan of the normalized ^{6}Li atom number as a function of photo-association laser energy $h\nu_{PA}$ after a 750 ms hold time with zero bias magnetic field and a PA laser intensity of $I_{PA} = 635$ W/cm^2. This is the second of the three resonances shown in Fig. 3.5 corresponding to a transition from an initial unbound molecular state with $N = 0$, $G = 0$ to the $v' = 21$ vibrational level of the $1^3\Sigma_g^+$ excited state with $N' = 1$, $G' = 0$. The ensemble temperature was 800 nK. The FWHM of this loss peak is 0.00048 cm^{-1} (14.4 MHz).

ground-state collisions. However, these features were *only* observable in our experiment when measures were taken to enhance the PA scattering rate. In order to observe these PA resonances, we enhanced the *p*-wave scattering rate by stopping the evaporation at an ensemble temperature of 250 μK and by holding the magnetic field at 185 G during the PA stage. This magnetic field is near the *p*-wave Feshbach resonance between the $|1\rangle$ and $|2\rangle$ states at 185.1 G [109]. Due to the Feshbach resonance enhancement of inelastic ground-state collisions, the ensemble particle loss in the absence of the PA light was approximately 50% during the 2 second hold time. Additional loss was induced when the light was near a PA resonance. Figure 3.7 shows the loss spectrum for a transition from an initial unbound molecular state with $N = 1, G = 1$ to the $v' = 20$ vibrational level of the $1^3\Sigma_g^+$ excited state with $N' = 2, G' = 1$. For each of the seven vibrational levels,
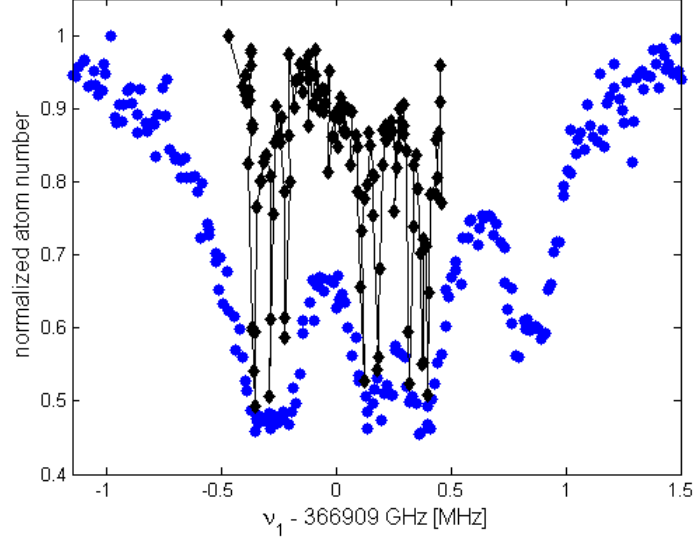
Figure 3.7: Normalized ^{6}Li atom number as a function of photo-association laser energy $h\nu_{PA}$ after a 2 second hold time. The circles are for an ensemble temperature of 250 μK at 185 G, and four distinct features are observed. The diamonds denote the atom loss for an ensemble temperature of 15 μK and at a magnetic field of 184.7 G. At this lower temperature, these loss features are seen to result from multiple PA resonances that are unresolvable at 250 μK. These PA features arise from p-wave ground-state collisions and are enhanced by proximity to a p-wave Feshbach resonance between the $|1\rangle$ and $|2\rangle$ states at 185.1 G. The ro-vibrational level shown here is $v' = 20, N' = 2$

we observed at least 4 (3) distinct loss features for transitions to the $N' = 2, G' = 1$ ($N' = 0, G' = 1$) final state. By evaporating the ensemble to 15 μK and holding the magnetic field at 184.7 G, we observed that each of these loss features results from multiple PA resonances that are unresolvable at 250 μK. The locations of the loss features observed at 250 μK for each of the seven vibrational levels is provided in Tables 3.4 and 3.5. These measurements were performed in the absence of the comb stabilization. Instead, the Ti:sapphire laser was referenced to the wavemeter whose uncertainty is 60 MHz.

To our knowledge, the enhancement of photoassociation with a p-wave Fesh-

Table 3.4: Experimentally measured PA resonances for *p*-wave collisions in an incoherent mixture of the $|1\rangle$ and $|2\rangle$ states of ^{6}Li held at a magnetic field of $B = 185$ G. Each of these values was extracted by fitting a loss spectrum like that shown in Fig. 3.7. These PA resonances correspond to a transition from an initial unbound molecular state with $N = 1, G = 1$ to the vth vibrational level of the $1^3\Sigma_g^+$ excited state with $N' = 0, G' = 1$. While the precision in these measurements is 0.001 cm^{-1}, the uncertainty, limited by the wavemeter, is ± 0.002 cm^{-1}

v'	1st cm^{-1} GHz	2nd cm^{-1} GHz	3rd cm^{-1} GHz
20	12236.388	12236.407	12236.424
	366837.68	366838.25	366838.76
21	12393.629	12393.648	12393.664
	371551.65	371552.22	371552.70
22	12545.320	12545.338	12545.355
	376099.23	376099.77	376100.28
23	12691.446	12691.465	12691.480
	380479.98	380480.55	380481.00
24	12831.995	12832.012	12832.029
	384693.53	384694.04	384694.55
25	12966.957	12966.975	12966.991
	388739.59	388740.13	388740.61
26	13096.326	13096.346	13096.362
	392617.98	392618.58	392619.06

bach resonance is the first example of FOPA (Feshbach-Optimized Photoassociation) [54] for a *p*-wave FR.

3.3.2   Spin-spin and spin-rotation constants

In order to properly label the three PA resonances (associated with ground state *s*-wave collisions) observed for each ro-vibrational state given spin-spin and spin-rotational coupling, we redefine $\vec{J}$ to be the total angular momentum *apart from nuclear spin*, $\vec{J} \equiv \vec{N} + \vec{S}$. Here, a magnetic coupling between $\vec{S}$ and $\vec{N}$ (involving an interaction term of the form $\hat{H}_{\text{spin}-\text{rot}} = \gamma_v \vec{N} \cdot \vec{S}$) as well as a spin-spin coupling term (of the form $\hat{H}_{\text{spin}-\text{spin}} = 2\lambda_v[\hat{S}_z^2 - \hat{S}^2/3]$) cause a splitting of the rotational levels,

Table 3.5: Experimentally measured PA resonances for *p*-wave collisions in an incoherent mixture of the $|1\rangle$ and $|2\rangle$ states of ^{6}Li held at a magnetic field of $B = 185$ G. Each of these values was extracted by fitting a loss spectrum like that shown in Fig. 3.7. These PA resonances correspond to a transition from an initial unbound molecular state with $N = 1, G = 1$ to the vth vibrational level of the $1^3\Sigma_g^+$ excited state with $N' = 2, G' = 1$. While the precision in these measurements is 0.001 cm^{-1}, the uncertainty, limited by the wavemeter, is ± 0.002 cm^{-1}

v'	1st cm^{-1} GHz	2nd cm^{-1} GHz	3rd cm^{-1} GHz	4th cm^{-1} GHz
20	12238.757	12238.772	12238.780	12238.795
	366908.70	366909.15	366909.39	366909.84
21	12395.936	12395.951	12395.958	12395.973
	371620.81	371621.26	371621.47	371621.92
22	12547.567	12547.579	12547.587	12547.601
	376166.60	376166.96	376167.19	376167.61
23	12693.628	12693.642	12693.648	12693.665
	380545.39	380545.81	380545.99	380546.50
24	12834.113	12834.128	12834.134	12834.150
	384757.03	384757.48	384757.66	384758.14
25	12969.011	12969.026	12969.032	12969.047
	388801.17	388801.62	388801.80	388802.25
26	13098.315	13098.332	13098.339	13098.355
	392677.60	392678.11	392678.32	392678.80

previously labeled by N, according to the J quantum number, given by $J = (N+S)$, $(N+S-1)$, $(N+S-2)$, $\cdots$, $|N-S|$. Therefore, each level with a given $N (\geq S)$ consists of $2S+1$ sub-levels, and the number of sub-levels is equal to the spin multiplicity. However, for $N < S$, the number of sub-levels is equal to $2N+1$ (the rotational multiplicity). Hence, all $N = 0$ levels do not split. For a particular ro-vibrational state, $|v, N\rangle$, with a total spin $S = 1$, the rotational energy is given
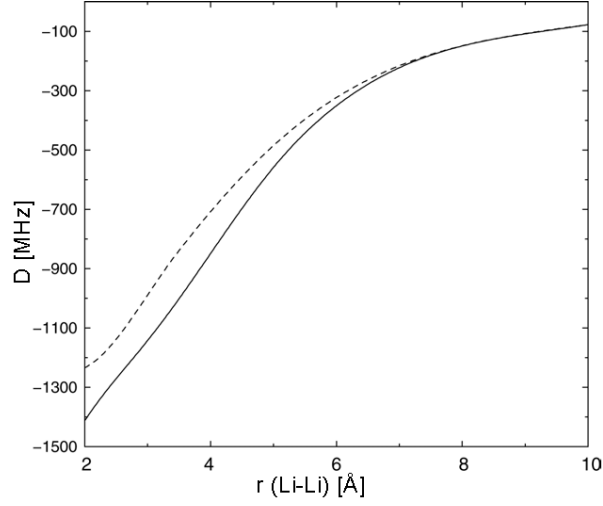
Figure 3.8: Spin-splitting parameter D = 2λ for the lowest triplet a($1^3\Sigma_u^+$) state (dashed line) and for the c($1^3\Sigma_g^+$) state (solid line) of Li$_2$ molecule. The figure taken from [129].

by [121, 128]

$$
\begin{aligned}
F_{J=N+1} &= B_v N(N+1) + (2N+3)B_v - \lambda_v \\
&\quad - \sqrt{(2N+3)^2 B_v^2 + \lambda_v^2 - 2\lambda_v B_v} + \gamma_v(N+1) \\
F_{J=N} &= B_v N(N+1) \\
F_{J=N-1} &= B_v N(N+1) - (2N-1)B_v - \lambda_v \\
&\quad + \sqrt{(2N-1)^2 B_v^2 + \lambda_v^2 - 2\lambda_v B_v} - \gamma_v N,
\end{aligned}
\tag{3.8}
$$

where λ_v and γ_v are constants. Here, λ_v is related to the spin-spin interaction and it describes the coupling between total spin, $\vec{S}$, and the molecular axis; γ_v is related to the spin-rotation interaction and it is a measure of the coupling between $\vec{S}$ and $\vec{N}$. Under most circumstances, these two constants describe small effects which are not spectroscopically resolvable and are typically ignored in the Dunham expansion. However, at the level of resolution in the current experiment, one needs to take into account these second-order perturbations.

When spin-spin and spin-rotation couplings are small ($B_v \gg |\lambda_v|, |\gamma_v|$) we can

75

Table 3.6: The values for the spin-spin interaction constant, λ_v, and the spin-rotation interaction constant, γ_v, determined from Eq. 3.9 and the peak spacings reported in Table 3.3. The uncertainty in these values is ± 400 kHz. The λ_v values are plotted in Fig. 3.9 along with their expected values determined from *ab initio* calculations.

v'	λ_v (MHz)	γ_v (MHz)
20	-348.2	-14.5
21	-339.4	-14.5
22	-331.1	-14.7
23	-321.7	-14.2
24	-312.2	-14.4
25	-303.6	-14.0
26	-294.3	-14.3

simplify Eq. 3.8 to

$$
\begin{aligned}
F_{J=N+1} &= B_v N(N+1) - \frac{2N+2}{2N+3}\lambda_v + \gamma_v(N+1) \\
F_{J=N} &= B_v N(N+1) \\
F_{J=N-1} &= B_v N(N+1) - \frac{2N}{2N-1}\lambda_v - \gamma_v N.
\end{aligned}
\tag{3.9}
$$

In addition, when spin-spin coupling is much more important than spin-rotation coupling ($|\lambda_v| \gg |\gamma_v|$), the energy ordering results from the λ_v terms, and we can label these three peaks in Table 3.3, energetically from low to high, as $(N'=1, J'=1)$, $(N'=1, J'=2)$, and $(N'=1, J'=0)$ because λ_v is negative.

Using the peak spacings reported in Table 3.3 and Eq. 3.9, we extract the two parameters, λ_v and γ_v. The determined λ_v constants as a function of v' are plotted in Fig. 3.9. The dashed line is provided to show its trend. These results agree well with the previous *ab initio* calculation for lithium diatoms [129]. By using Fig. 3.8 (taken from Ref. [129]) and averaging $\lambda(R)$ over the internuclear distance R using the wave functions corresponding to the eigenfunctions of the excited state potential curve we refined with our data, we estimate these *ab initio* λ_v constants for all v' states and plot those also in Fig. 3.9. Note, the uncertainty of the *ab initio* results given in Fig. 3.9 is at least a few tens of MHz. This results from the es-
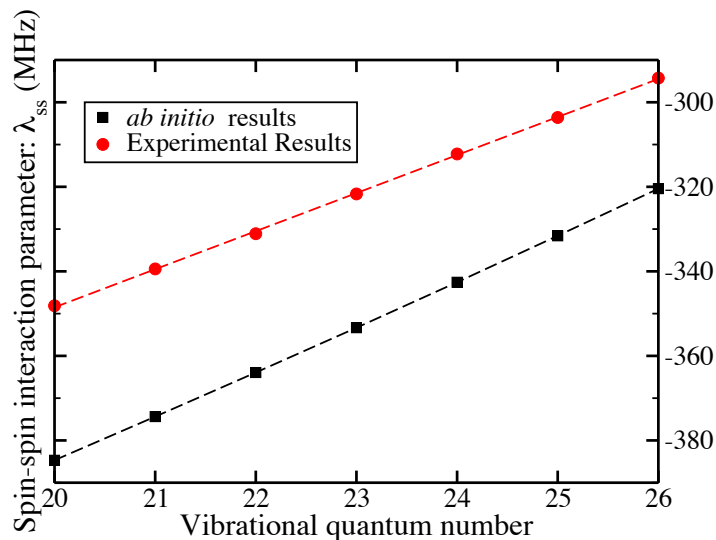
Figure 3.9: The experimentally determined (circles) and *ab initio* computed (squares) spin-spin interaction constants, λ_v, as a function of the vibrational quantum number for the $1^3\Sigma_g^+$ electronic state. These constants were determined from the frequency splittings of the three features observed for the $N = 0 \rightarrow N' = 1$ transition. The uncertainty in these values is ±400 kHz. The dashed lines are guides to the eye. Figure taken from [49].

timated error of the original *ab initio* calculation (a few percent corresponding to $\approx 10 - 30$ MHz) and the error (≈ 10 MHz) associated with our digitization of the data in Fig. 3.8, as well as the fact that the *ab initio* calculation was likely done for ^{7,7}Li$_2$ rather than ^{6,6}Li$_2$. This comparison of λ_v obtained from experimental data and that obtained from *ab initio* calculations clearly demonstrates the validity of the current model to label separate peaks in Table 3.3. The values for λ_v and γ_v determined from our data are provided in Table 3.6. The uncertainty in these parameters is ±400 kHz and results from the uncertainty in the PA resonance positions. Using Eq. 3.8, we verified that the uncertainty in the exact value for B_v does not contribute significantly to the uncertainty in these parameters. We note that this is the first direct measurement of the spin-spin and spin-rotation coupling
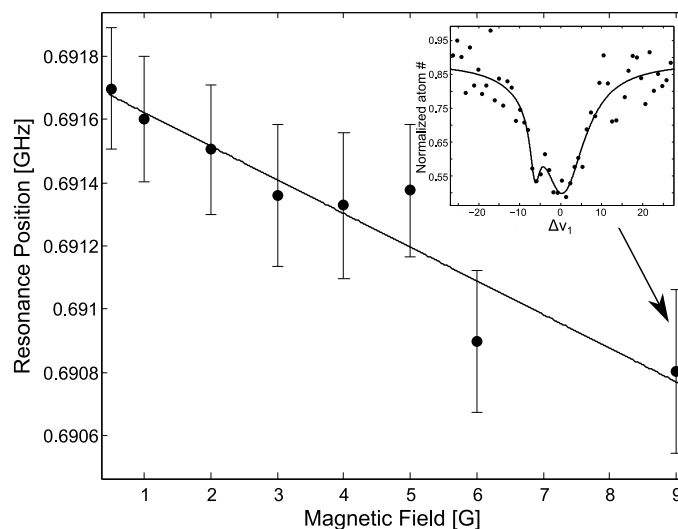
Figure 3.10: $v' = 24, N' = 1, J' = 1$, magnetic field dependence for low magnetic fields. Around 10 G the line shows signs of splitting into Zeeman sublevels (inset).

constants in a diatomic lithium system.

3.3.3 Systematic shifts

While the absolute uncertainty of our PA measurements made using the frequency comb is ± 600 kHz, the data was taken in the presence of a small but non-zero magnetic field and in an optical dipole trap with a known intensity. These residual fields as well as the PA laser itself can lead to a systematic shift of the resonance positions from their zero-field values. Therefore, in an effort to quantify the role of the PA laser intensity, the CDT laser intensity, and the residual magnetic field on the PA loss features, we varied each one and measured the PA resonance position and width for various excited states. In each case, we assumed a linear dependence and determined a shift rate of the resonance position with the corresponding field strength. The uncertainty in this rate is a one-sigma statistical uncertainty on the slope of the linear fit.

When varying the photoassociation laser intensity from $I_{PA} = 0.19$ kW/cm^2 to $I_{PA} = 1.27$ kW/cm^2 we observed that the centroid of the first feature ($J' = 1$)
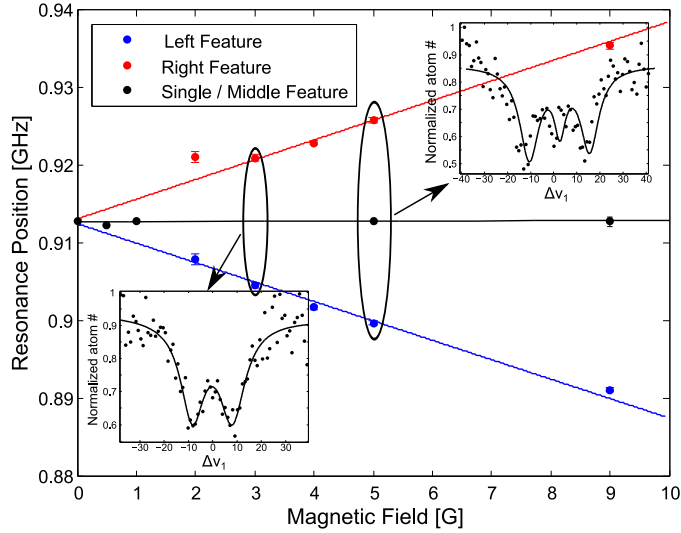
Figure 3.11: $v' = 24$, $N' = 1$, $J' = 2$, magnetic field dependence for low magnetic fields. The loss feature splits into peaks corresponding to Zeeman sublevels (insets). To estimate the influence of the magnetic field on the position of the photoassociation feature the center of gravity of the line at each magnetic field has been determined (near horizontal line).

associated with the $v' = 26$ excited state shifted to higher frequencies at a rate of 471 ± 433 kHz per kW/cm^2. When the CDT laser (1064 nm) intensity was varied from 5.4 kW/cm^2 (145 mW total CDT power) to 140 kW/cm^2 (3.1 W total CDT power) the PA feature centroid associated with the $v' = 24$, $J' = 1$ state shifted down in frequency at a rate of $-(19 \pm 1.2)$ kHz per kW/cm^2. The resonance positions reported in Table 3.3 were determined using a PA laser intensity of $I_{PA} = 635$ W/cm^2, and a CDT intensity of 7.5 kW/cm^2. Assuming the differential ac Stark shift is the same for all excited states, the reported values are therefore shifted lower by 142 ± 9 kHz due to the CDT and higher by 300 ± 274 kHz due to the PA laser than their extrapolated position at zero differential ac Stark shift. The overall AC Stark shift of the resonance positions is thus higher by 157 kHz with an uncertainty of ± 274 kHz. Both this shift and uncertainty are small compared to the absolute uncertainty of the frequency comb. For the resonance positions reported in Tables 3.4 and 3.5, the trapping power was larger (40 W total) and the differential AC Stark shift due to the CDT is estimated to be $-(15 \pm 1)$ MHz.
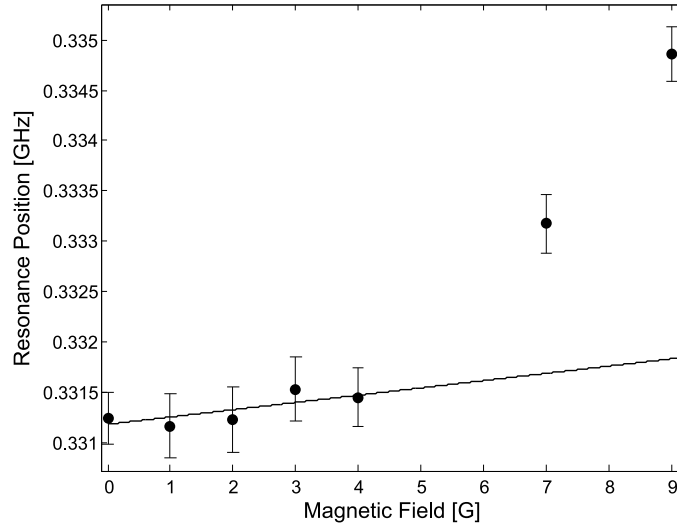
Figure 3.12: $v' = 24$, $N' = 1$, $J' = 0$, magnetic field dependence for low magnetic fields. No Zeeman splitting has been observed, as opposed to the measurements of the $J' = 1$ and $J' = 2$ levels. To estimate the systematic shift a linear dependence near 0 G has been assumed.

When the magnetic field was varied from 0 G to 10 G the PA features associated with the $v' = 24$, $J' = 1$, $J' = 2$, and $J' = 0$ states were observed to shift and, in the case of $J' = 1$ and $J' = 2$, to broaden and eventually split into multiple resolvable peaks (see Figs. 3.10,3.11,3.12). In each case, we measured the PA feature center of mass and found that when the magnetic field was varied from 0 to 1 G, the barycenter of the PA features moved by $-(91.2 \pm 18.3)$ kHz for the $J' = 1$ state, $+(46 \pm 28)$ kHz for the $J' = 2$ state, and $+(74.5 \pm 30.1)$ kHz for the $J' = 0$ state. Since the resonance positions reported in Table 3.3 were determined in the presence of a residual magnetic field below 400 mG, the uncertainty in their positions due to the magnetic field was below 50 kHz for all J states and thus small compared to the absolute uncertainty of the frequency comb.
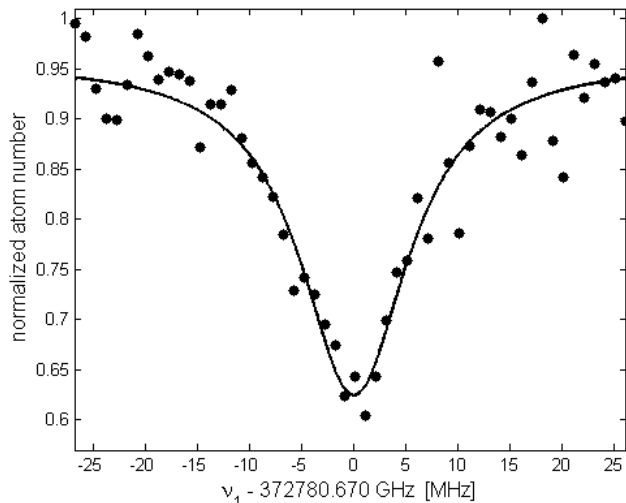
Figure 3.13: High resolution scan of the normalized ^{6}Li atom number as a function of photoassociation laser energy $h\nu_{PA}$ after a 1 s hold time with zero bias magnetic field and a PA laser intensity of $I_{PA} = 755$ W/cm^2. The feature corresponds to a transition from an initial unbound molecular state with $N = 0$, $G = 0$ to the $v' = 31$ vibrational level of the $1^1\Sigma_u^+$ excited state with $N' = 1$, $G' = 0$. The ensemble temperature was 600 nK. The FWHM of the loss signal is 13 MHz.

3.4 Spectroscopy of the A($1^1\Sigma_u^+$) potential

In its gaseous form ^{6}Li$_2$ exists predominantly in the ground state, X($1^1\Sigma_g^+$). For this very reason various spectroscopy methods can be easily applied to probe excited state levels of singlet potentials. The A($1^1\Sigma_u^+$) potential (in conjunction with the ground X-state), especially, has been extensively studied and many rovibrational levels in the range $v = 0 - 88$ have been measured [130] prior to this work. However, the only photoassociation spectroscopy of this potential that precedes our work has been done in a MOT and $v' = 62 - 88$ levels have been reported [104, 125]. Here we present the binding energy measurements of seven vibrational levels $v' = 29 - 35$ of the A($1^1\Sigma_u^+$) excited state of ^{6}Li$_2$ molecules with an absolute uncertainty of ± 600 kHz by photoassociating a quantum degenerate Fermi gas of lithium atoms held in a shallow optical dipole trap, with the atomic

ensemble prepared as described in Section 2.3.4. These measurements represent an observation of the $N' = 1$ rotational level [1] for each of the reported vibrational levels and have absolute uncertainties that are 25 to 500 times smaller than other data available for the A-state.

The experiments are performed in an ensemble of 4×10^4 atoms with equal populations in the states $|1\rangle$ and $|2\rangle$. After the preparation stage, we apply a homogeneous magnetic field that cancels any residual field remaining at the location of the atoms. The background field after cancellation is verified to be less than 20 mG via rf spectroscopy between the $F = 1/2$ and $F = 3/2$ ground hyperfine levels of ^{6}Li (for details see Section 2.3.4). The dipole trap arrangement used for these measurements is shown in Fig. 2.11b. The photoassociation light propagates colinearly with the recycled crossed optical dipole trap (Fig. 2.11b) and illuminates the cloud for 2 s. The atom number is then measured and from the loss of atoms the location of a PA resonance can be extracted. Figure 3.13 shows an example of a resulting feature.

The photoassociation spectrum observed for seven vibrational levels ($v' = 29 - 35$) of the A($1^1\Sigma_u^+$) state arises from s-wave collisions between atoms in states $|1\rangle$ and $|2\rangle$; see Table 3.7. To reduce thermal broadening and the inhomogeneous ac Stark shift produced by the CDT potential, these data were obtained in a low intensity trap ($I_{CDT} = 9.6$ kW/cm^2). At this low trap power, the ensemble temperature is 800 nK ($T/T_F = 0.4$). In order to fully characterize the systematic shifts of the resonance location due to the CDT and PA laser, we varied the CDT intensity from 9.6 to 55 kW/cm^2 and the PA laser intensity from 65 to 760 kW/cm^2 for each of the seven vibrational levels.

Assuming that the ac Stark shift from each laser is independent, and the shift of the resonance position is proportional to the laser intensity, the shift in the resonance locations can be fit to extract the shift rate due to the dipole trap and PA beam (Table 3.7). In addition, the field free resonance location can be inferred (Table 3.8).

The 1σ statistical error on the fit to the resonance location, and to the extrapolated field free resonance location is typically 250 kHz, which is small compared

---

[1] For levels $v' = 29 - 35$ the rotational levels $N' = 1$ have not been observed in previous experiments (Refs. [130, 131]).

Table 3.7: Experimentally measured PA resonances for *s*-wave collisions in an incoherent mixture of the $|1\rangle$ and $|2\rangle$ states of ^{6}Li. These PA resonances correspond to a transition from an initial unbound molecular state with $N = 0$, $G = 0$ to the vth vibrational level of the $A^1\Sigma_u^+$ excited state with $N' = 1, G' = 0$. For these measurements, the CDT intensity was 9.6 kW/cm^2 and the PA laser intensity was 65 W/cm^2. The absolute uncertainty in each of these measurements is ± 600kHz. The ac Stark shift of each resonance induced by the PA laser and the CDT laser is also listed, where the number in brackets is an estimation of the 1σ error on the last digit(s).

v	Feature (GHz)	ODT Shift Rate kHz / (kW/cm^2)	PA Shift Rate kHz / (kW/cm^2)
29	363113.1067	199(6)	-745(661)
30	368015.0436	-546(11)	-2120(783)
31	372780.6714	44(4)	-73(228)
32	377406.2393	-79(6)	803(707)
33	381887.7859	100(5)	80(253)
34	386221.1190	73(5)	272(265)
35	390401.8749	-9(10)	-826(437)

Table 3.8: Extrapolated field free resonance locations based on the table 3.7.

v'	Field free feature cm^{-1}	GHz
29	12112.14946	363113.1058
30	12275.66069	368015.0492
31	12434.62472	372780.6709
32	12588.91710	377406.2401
33	12738.40534	381887.7848
34	12882.94978	386221.1181
35	13022.40482	390401.875

to the absolute uncertainty of the frequency comb. Since the magnetic field is confirmed to be less than 20 mG, any systematic shifts due to the residual magnetic field are negligible. Note that at low dipole trap intensities, the CDT potential is tilted due to gravity which leads to a spilling of atoms out of the trap. Typically, this tilt can be offset using a magnetic field gradient. However, it is not feasible to compensate for the tilt due to gravity and keep the magnetic field in (and across) the region of the atoms at a small (less than 20 mG) value. Therefore, 9.6 kW/cm^2 is the lowest CDT intensity we can use for PA spectroscopy without incurring large atom loss.

3.4.1 $v' = 30$ anomaly

Unlike for the other vibrational levels probed, for the $v' = 30$ vibrational level we observe a splitting of the resonance into many distinctive features shown in Figs. 3.14a to d. The splitting does not depend on the PA light intensity as confirmed by the measurements for different PA light intensities that varied by a factor of 30. For the lowest PA and dipole trap intensities, 0.13 kW/cm^2 and 9.7 kW/cm^2, respectively, the splitting is not present (Fig. 3.14d). When the dipole trap intensity is increased by a factor of five the level experiences a strong ac Stark shift and two distinct loss features separated by 18 MHz appear (Fig. 3.14e to f). We attribute this splitting to a CDT laser-induced coupling of $v' = 30$ to another molecular level in one of the potentials dissociating to the $2p + 2p$ asymptote. Performing spectroscopy in a dipole trap operating at various frequencies would allow us to modify the strength of the coupling thus verifying our assertion. In our setup this could be achieved by changing the temperature of the laser used for optical trapping, resulting in a frequency change on the order of 10 GHz. Such a test has not been performed yet.
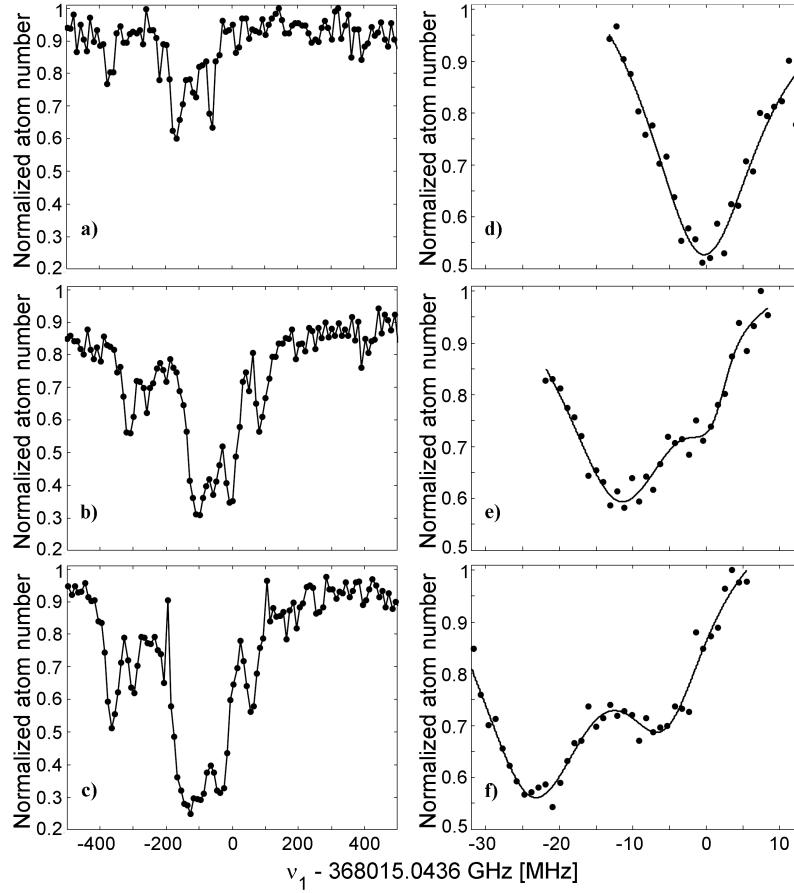
Figure 3.14: Normalized ^{6}Li atom number as a function of photoassociation laser energy $h\nu_{PA}$ after a 1 s hold time with zero bias magnetic field. a)-c) The photoassociation laser is locked to its cavity and the accuracy is on the order of the wavemeter read out accuracy, 60 MHz. The data is taken for three different PA laser intensities I_{PA} a) 0.13 kW/cm^2, b) 1.3 kW/cm^2 and c) 3.3 kW/cm^2 at the dipole trap intensity of 410 kW/cm^2 with the sample temperature of 25 μK. d)-f) The photoassociation laser is locked to the frequency comb. The data is taken with $I_{PA} = 0.13$ kW/cm^2 for three different dipole trap intensities d) 9.7 kW/cm^2, e) 32.5 kW/cm^2 and f) 54 kW/cm^2. The feature corresponds to a transition from an initial unbound molecular state with $N = 0$, $G = 0$ to the $v' = 30$ vibrational level of the $1^1\Sigma_u^+$ excited state with $N' = 1$, $G' = 0$. The splitting has not been observed in other measured levels.

85

Chapter 4

Dark state spectroscopy of bound molecular states

The main results of this Chapter are based on

- **M. Semczuk**, *W. Gunton, W. Bowden and K. W. Madison, "Anomalous behavior of dark states in quantum gases of ^{6}Li.", Phys. Rev. Lett.* **113**, *055302, July (2014)* [52].

Coherent dark states [132] in ultracold atomic gases lie at the heart of phenomena such as electromagnetically induced transparency [133], slow light [134] and coherent population transfer [135, 136]. They are useful for precision spectroscopy of molecular levels [137] and studies of their properties [138]. In recent years such superposition states between atoms and molecules have been demonstrated in ultracold metastable ^{4}He [137] and ^{23}Na [139] as well as in a Bose-Einstein condensate of ^{87}Rb atoms [140]. Other important examples of systems where molecule-molecule dark states have been created include ^{87}Rb [141, 142], ^{84}Sr [143] and ^{133}Cs [144]. Due to the nature of dark states, coherence is achieved between the initial and the final state and as a result of destructive interference, no intermediate molecular levels are populated. The experiments prior to our work focused on bosonic atomic species with a notable exception of a non-degenerate fermionic molecules of KRb [23, 145]. Most of these experiments have been restricted to magnetic fields close to Feshbach resonances, and due to the increased three-body recombination [146] the sample would rapidly decay (typically in less than 10 ms).

The ability to create atom-molecule or molecule-molecule dark states is a prerequisite to coherently transfer weakly bound Feshbach molecules to a deeply bound level in the electronic ground state using stimulated Raman adiabatic pas-

sage technique (STIRAP) [136]. When the initial state is a Feshbach molecule and the final state a deeply bound level in the lowest singlet or triplet potential (including the rovibratonal ground state), this method has been shown to work remarkably well with ^{87}Rb [141, 142], ^{84}Sr [143], ^{133}Cs [144, 147], ^{40}K^{87}Rb [23, 145], ^{87}Rb^{133}Cs [148, 149] and ^{23}Na^{40}K [150]. The initial Feshbach molecules are, however, short lived (on the order of 10 ms) [151] if they consist of bosonic atoms; therefore to improve the efficiency of the transfer they needed to be separated in a 3D optical lattice to avoid three-body recombination. One of the main goals of these experiments has been to create a Bose-Einstein condensate (BEC) or a degenerate Fermi gas (DFG) of molecules in the absolute rovibrational ground state. The required temperatures and phase space densities have not been achieved yet and so far it is not clear if simply melting the 3D lattice as proposed by Jaksch *et al.* [152] can lead to the final goal.

Theoretical proposals suggest that dark states can also be created in degenerate Fermi gases [153, 154] and they have great potential as a probe of many-body physics (e.g. BCS pairing and superfluidity) [153, 155–157] avoiding the final state effects that complicate the interpretation of the rf spectra of the BCS pairs [74, 90]. As proposed in the context of ^{6}Li, molecular dark states can be used for the optical control of magnetic Feshbach resonances (FR) [158, 159]. This method not only suppresses spontaneous scattering but also provides larger tuning of the interactions than a single frequency approach [100, 101] while enabling independent control of the effective range. The proposal applies to all alkali species and has important consequences to anyone interested in the dynamics of Bose and Fermi gases at unitarity.

As opposed to molecules consisting of bosons, a two-component Fermi gas of ^{6}Li forms Feshbach molecules that are long lived, with lifetimes approaching 10 s [160]. This is a direct consequence of the Fermi statistics for the ^{6}Li atoms that leads to the suppression of the collisional relaxation of the weakly bound dimers to deep bound states [87]. Additionally, depending on the value of the magnetic field B with respect to the Feshbach resonance at $B = 832.18$ G, a Bose-Einstein condensate of Feshbach molecules [65, 113] ($B < 832.18$ G) or BCS-like pairs [161] ($B > 832.18$ G) can be created. The demonstration of dark states in the BEC-BCS crossover regime (Section 4.6) opens up possibilities of using STIRAP to transfer

the initial Bose-condensed state to a sample of ground state molecules that is expected to be also Bose-condensed. [1] The sample is also "bulk" as no separation using a 3D lattice is required, a feature not presently available with non-fermionic systems currently under consideration and allowing greater flexibility of studies of eventual ground-state molecules.

Building on the method demonstrated by Moal *et al.* [137] we have used dark states created in the non-interacting Fermi gas at 0 G to determine the binding energy of the $v'' = 9$, $N'' = 0$ ro-vibrational level of the $a(1^3\Sigma_u^+)$ potential with accuracy improved by a factor of 500 over [162] and [163]. The molecular hyperfine structure of this level has been resolved and the binding energy of the $v'' = 38$, $N'' = 0$ ro-vibrational level of the $X(1^1\Sigma_g^+)$ potential has been measured for the first time in the ultracold regime. Measurements of this type do not require dark state spectroscopy method but they benefit significantly from the superior accuracy that is hard to reach with commonly used two-color photoassociation spectroscopy [162–164]. Since both the hyperfine structure of $v'' = 9$ and the binding energy of $v'' = 38$ have not been observed prior to this work our result might be of interest to spectroscopists because Li_2 is the simplest neutral diatomic molecule after H_2. Additionally, the $a(1^3\Sigma_u^+)$ state of H_2 is not bound [165] therefore Li_2 seems like the best candidate to study the properties of this potential. Our results might have impact not only on the models for molecular potentials but, more importantly, on the molecular theory itself because the observed hyperfine splittings do not match what is expected based on the theory outlined by A. J. Moerdijk and B. J. Verhaar [166] (see Section 4.4).

4.1 Two-color photoassociation and dark states: theory

Here we present a brief overview of the scattering process in the presence of two laser fields based on the theory of laser assisted collisions developed by Bohn and Julienne (for a detailed discussion see [167, 168]). The analysis presented here is limited to three-level systems in the Λ configuration as shown in Fig. 4.1, which are the most relevant to the experiments discussed in this Chapter.

---

[1]The result depends, among other factors, on the polarizbility of the ground state molecules as this influences the trapping frequencies and, consequently, changes the critical temperature.

In a collision process a pair of cold atoms with relative energy E (typically $< 10\,\mu$K in our experiments) approaches one another guided by their interaction potential U_0. In the presence of two laser fields the atom pair can be promoted by the first laser with frequency $\omega_1/2\pi$ to a bound molecular state $|b\rangle$ with energy E_b. From the level $|b\rangle$ the second laser with frequency $\omega_2/2\pi$ can drive the atom pair to another bound molecular level $|g\rangle$ with energy E_g, here chosen to belong to either singlet or triplet ground molecular potential.

There exists the possibility of a spontaneous emission event in which the excited molecule decays into bound ground states or into dissociative continuum of two ground-state atom which may have enough kinetic energy to leave the trap. In both cases the observed trapped atom number decreases. Another trap loss mechanism is caused by nonradiative decay to other molecular states that cannot be detected in a typical experiment.

The formalism developed by Bohn and Julienne relates the two-color photoassociative loss to the thermally averaged value of the loss of population from the excited state $|b\rangle$ ($|S_b|^2$) and decay of molecules in the probed ground singlet or triplet potential $|g\rangle$ ($|S_g|^2$)^2:

$$K(T,\Delta_1,\Delta_2,I_1,I_2,\gamma_b,\gamma_g) = \langle \frac{\pi v}{k^2} \sum_{l=0}^{\infty}(2l+1)(|S_b|^2+|S_g|^2)\rangle. \qquad (4.1)$$

The brackets denote the appropriate thermal average over a distribution of relative velocities v, at temperature T, and $k = \sqrt{2\mu E/\hbar^2}$, where μ and E are the reduced mass and kinetic energy of the colliding par. The detunings Δ_1 and Δ_2 of lasers with intensities I_1 and I_2 are defined in Fig. 4.1. Assuming Maxwellian distribution at temperature T and taking into account that for lithium only s-wave ($l = 0$) collisions take place at temperatures in the microkelvin range (and below), we obtain

$$K(T,\Delta_1,\Delta_2,I_1,I_2,\gamma_b,\gamma_g) = \frac{1}{hQ_T}\int_0^\infty (|S_b|^2+|S_g|^2)e^{-E/k_B T}dE, \qquad (4.2)$$

where the partition function for the reduced mass μ is $Q_T = (\frac{2\pi k_B T\mu}{h^2})^{3/2}$.

From the scattering amplitudes S_b and S_g derived by Bohn and Julienne in

---

^{2}S_b and S_g are diagonal elements of the scattering matrix (S-matrix).

Figure 4.1: Δ_1 and Δ_2 denote the detunings from the one-photon and two-photon resonance, respectively, of lasers with frequencies $\omega_1/2\pi$ and $\omega_2/2\pi$ and intensities I_1 and I_2. Ω_1 and Ω_2 are Rabi frequencies. The excited molecular state of energy E_b $|b\rangle$ spontaneously decays with a rate γ_b to levels outside this scheme. The molecular state of energy E_g $|g\rangle$ is attributed a decay rate γ_b which phenomenologically takes into account losses through inelastic collisions and laser induced dissociation, e.g., when laser 1 couples $|g\rangle$ to the unstable state $|b\rangle$. E is the relative energy of a colliding pair $|a\rangle$.

Ref. [168] we obtain scattering probabilities

$$|S_b|^2 = \frac{\gamma_b \gamma_s [(E - \Delta_2)^2 + \gamma_g^2/4]}{n(E, \gamma_s, \gamma_b, \gamma_g, \Delta_1, \Delta_2)}, \tag{4.3}$$

$$|S_g|^2 = \frac{\hbar^2 \Omega_2^2 \gamma_g \gamma_s}{n(E, \gamma_s, \gamma_b, \gamma_g, \Delta_1, \Delta_2)}, \tag{4.4}$$

$$n(E, \gamma_s, \gamma_b, \gamma_g, \Delta_1, \Delta_2) = \left\{ [E - (\Delta_1)][E - \Delta_2] - (\hbar\Omega_2)^2 - \gamma_g(\gamma_b + \gamma_s)/4 \right\}^2$$
$$+ \left\{ (\gamma_b + \gamma_s)(E - \Delta_2)/2 + \gamma_g[E - (\Delta_1)]/2 \right\}^2, \tag{4.5}$$

where the symbols are consistent with the convention used throughout the thesis (explained in Fig. 4.1) rather than Ref. [168].

In the above equations γ_s represents the stimulated absorption/emission rate

generated by the laser due to coupling of levels $|a\rangle$ and $|b\rangle$:

$$\gamma_s = 2\pi V_{ab}^2 |\langle a|b \rangle|^2 = 2\pi(\hbar\Omega_1)^2, \tag{4.6}$$

where V_{ab} is a radiative coupling of levels $|a\rangle$ and $|b\rangle$. The light shift induced by coupling $|a\rangle$ and $|b\rangle$ by the laser with intensity I_1 is incorporated into Δ_1.

In order to relate $|S_b|^2$ and $|S_g|^2$ to observables typically used in ultracold atom experiments (usually the atom number N) let's consider the loss of population from the dipole trap in the presence of two laser fields. It can be described by the evolution of the atomic density

$$\dot{n} = -2Kn^2 - \Gamma n \tag{4.7}$$

with Γ being the one-body loss rate due to background collisions and off-resonant scattering from the photoassociation lasers. K determines the spectrum of the photoassociative loss and is obtained from combining Eqs. 4.2, 4.3, 4.4 and 4.5. The integration of Eq. 4.7 gives the atom number $N(t)$ as a function of the photoassociation time t:

$$N(t) = \frac{N_t}{1 + \frac{2N_t K_{eff} V_t}{\Gamma V_0^2}\left(e^{\Gamma t} - 1\right)} \tag{4.8}$$

where N_t is the atom number after a hold time corresponding to the photoassociation time t but with no photoassociation light present. The volumes V_0 and V_t are the initial trap volume and the volume after time t, respectively. K_{eff} is defined following [164] as

$$K_{eff} = \frac{1}{V_t}\int_V d^3 r e_V^{-2U(\vec{r})/k_B T} \times \frac{1}{hQ_T}\int_0^{U_{max}-U(r)} dE(|S_b|^2 + |S_g|^2)e^{-E/k_B T}. \tag{4.9}$$

where $U(r)$ is the trap potential. The first integral in Eq. 4.9 is the effective trap volume. The kinetic energy integral is truncated by the local trap depth $U_{max} - U(r)$.

The analysis presented above can be used to model multiple physical realizations of two-photon-assisted collision processes like Autler-Townes doublet, the electromagnetically induced transparency or coherent population trapping resonance [133]. Complementary treatments extending the theory of scattering in the presence of two laser fields can be also found in e.g. [169] and [170]. The semiclas-

91

sical density matrix representation describing a set of closed three-level Λ atomic or molecular states (Ref. [170]) is analogous to the treatment of atom-molecule dark states in a BEC of ^{87}Rb used by Winkler *et al.* [140]. The analysis of our data follows the same approach (Section 4.4).
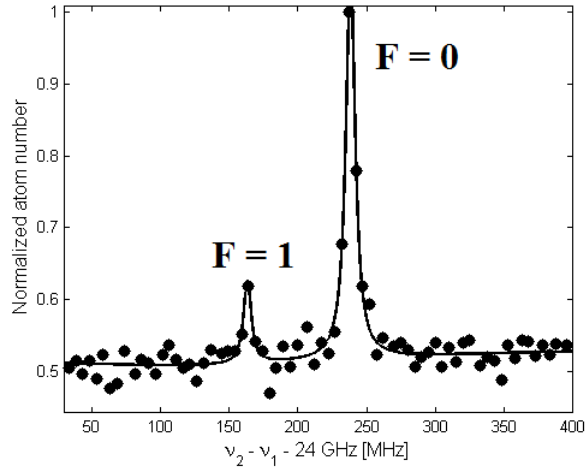
4.2   Two-color photoassociation

The single color photoassociation spectroscopy, discussed in Chapter 3, is an efficient method to determine binding energies of molecules in excited states. However, probing the ground state molecular potentials is not as straightforward. In principle, by measuring the frequency of the photons emitted when the excited molecules decay into the ground state molecules one could determine the energy difference between the rovibrational levels involved in the process and extract from that information about the ground state potential. This approach, the detection of fluorescence, is typically used when studied large ensembles of molecules in molecular beams or in hot vapors. However, the number of molecules involved in ultracold experiments is so low that fluorescence measurements would require near single photon detection capability. Moreover, the assignment of the frequencies of the fluorescence photons to the final molecular levels requires the knowledge of accurate models of molecular potentials. Alternatively, instead of looking at the fluorescence one could directly probe the population created from the decay of the excited state molecules using state selective ionization. REMPI (resonance-enhanced multiphoton ionization) was already demonstrated to work with ultracold RbCs [171] and LiCs [172] molecules trapped in a magneto-optic trap. The drawback of the above methods is that they require additional, quite often expensive, hardware (like tunable pulsed lasers for photoionization and ion detectors) that significantly increase the complexity of the experiments and limit the optical access to the atoms. As a result, these solutions put constraints on the range of the experiments that can be done in a given setup.

In experiments with ultracold gases the most common method to measure binding energies of molecular ground state levels is the so called two-color photoassociation which relies on a 3-level Λ system as shown in Fig. 4.1, where $|e\rangle$ is one of the excited molecular levels (see Chapter 3) and $|g\rangle$ is a level in the $a(1^3\Sigma_u^+)$
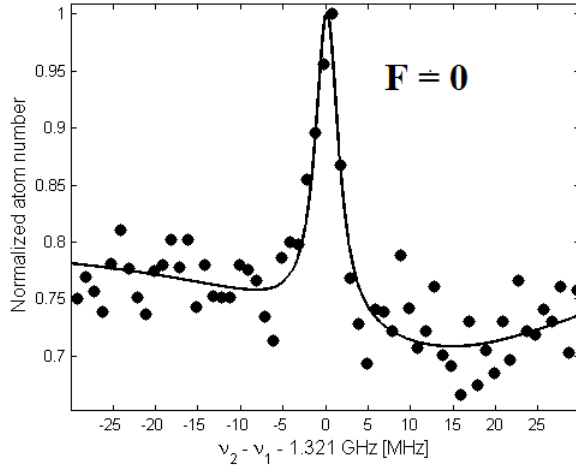
Figure 4.2: The normalized ^{6}Li atom number in two color photoassociation spectroscopy of the $v'' = 38$, $N'' = 0$ ro-vibrational level in the $X(1^1\Sigma_g^+)$ potential. The laser L_1 with frequency v_1 induces constant loss by driving transition from an initial unbound molecular state with $N = 0$, $G = 0$ to the $v' = 31$ vibrational level of the $1^1\Sigma_u^+$ excited state with $N' = 1, G' = 0$ while the frequency v_2 of the laser L_2 is varied across the $v' = 31$ to $v'' = 38$ transition. The bias magnetic field is set to 0 G.

or $X(1^1\Sigma_g^+)$ potential which binding energy we want to measure (Fig. 4.4). The starting point here is a pair of colliding atoms confined in a $\sim 10\mu$K deep dipole trap, that are resonantly coupled by a laser L_1 (frequency $\omega_1/2\pi$) to some molecular level $|e\rangle$. The intensity of this laser is set such that during time t the induced atom loss (due to single-color photoassociation) can be clearly distinguished from the shot-to-shot atom noise. In practice, the loss is typically kept in the 30%-50% range. The frequency $\omega_2/2\pi$ of the second laser L_2 is then varied to match the resonance condition $\omega_{e\text{-}g}/2\pi$ corresponding to the energy difference between bound levels $|e\rangle$ and $|g\rangle$. When $\omega_2/2\pi$ approaches $\omega_{e\text{-}g}/2\pi$ it reduces the rate of loss of trapped atoms *increasing* the trapped atom number. In our experiments the intensity of L_2 is kept low such that the primary mechanism responsible for the suppression of loss is the reduction of the population of molecules in the excited molecular state, reducing the rate of spontaneous emission events that lead to the atom loss [173].

93

Figure 4.3: The normalized ^{6}Li atom number in two color photoassociation spectroscopy of the $v'' = 9, N'' = 0$ ro-vibrational level in the $a(1^3\Sigma_u^+)$ potential. The laser L_1 with frequency ν_1 induces constant loss by driving transition from an initial unbound molecular state with $N = 0, G = 0$ to the $v' = 20$ vibrational level of the $1^3\Sigma_g^+$ excited state with $N' = 1$, $G' = 0, J' = 1$ while the frequency ν_2 of the laser L_2 is varied across the $v' = 20$ to $v'' = 9$ transition. The bias magnetic field is set to 0 G. The molecular hyperfine structure is partially resolved.

Figures 4.2 and 4.3 are examples of a two-color photoassociation spectroscopy applied to determine the binding energies of $v'' = 38, N'' = 0$ and $v'' = 9, N'' = 0$ ro-vibrational levels in the $X(1^1\Sigma_g^+)$ and $a(1^3\Sigma_u^+)$ potentials, respectively. Here, both lasers L_1 and L_2 are locked to the same frequency comb to increase the accuracy of the measurements but the scheme does not rely on the phase coherence of the lasers. In fact, the initial detection of these levels was done with the frequency of the laser L_2 stabilized to an external cavity while laser L_1 was stabilized to the frequency comb.

The method described above supported by the theoretical framework presented in Section 4.1 has been used by many experimental groups to determine the binding energies of bound molecular levels, with the emphasis on the ground state molecular potentials [164, 173–181]. In our case, however, this is only the first step necessary for further experiments where the binding energies are measured

94
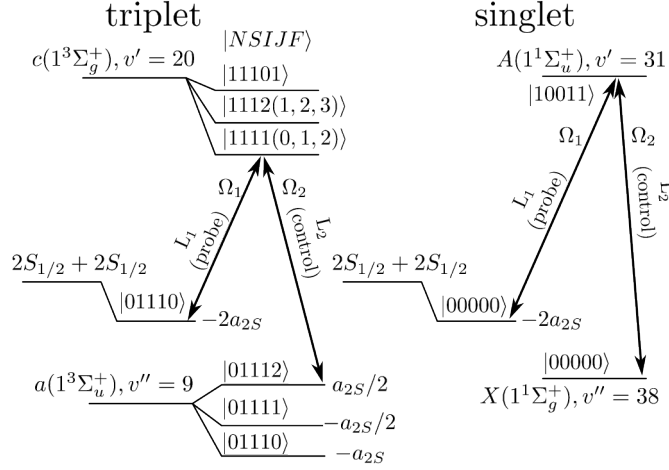
Figure 4.4: Energy levels at $B = 0$ relevant to the dark state experiments presented here. At $B = 0$, the initial unbound two-atom spin state is $|i_0\rangle = \sqrt{1/3}|00000\rangle + \sqrt{2/3}|01110\rangle$, a linear combination of the singlet and triplet states shown lying $2a_{2S}$ below the $2S_{1/2} + 2S_{1/2}$ asymptote. The levels are labeled with the quantum numbers $|NSIJF\rangle$, where $\vec{N}$ is the molecular rotational angular momentum, $\vec{S}$ is total electronic spin, $\vec{I}$ is total nuclear spin, $\vec{J}$ is total angular momentum apart from nuclear spin and $\vec{F} = \vec{J} + \vec{I}$. Here, Ω_1 and Ω_2 are Rabi frequencies of transitions driven by the lasers L_1 and L_2, respectively, and $a_{2S} = 152.137$ MHz is the atomic magnetic dipole hyperfine constant of $2^2S_{1/2}$. The naming convention of the lasers refers to their role in the dark state spectroscopy experiments. The hyperfine splittings of the $v'' = 9$ level shown here differ from our measurements, as discussed in Section 4.4. It should be also noted that a similar figure in [162] contains an incorrect hyperfine shifts of $|01112\rangle$ and $|01110\rangle$ levels in the $a(1^3\Sigma_u^+)$ potential.

exploiting the coherence properties of atom-molecule dark states.

4.3 Dark state spectroscopy

After atoms are transferred into the low power CDT a uniform magnetic field is set to 300 G and the sample is evaporatively cooled to the desired temperature. The magnetic field is then turned off and three orthogonal pairs of compensation coils are used to cancel the residual magnetic field to a level below 20 mG, as con-

firmed by the rf spectroscopy (section 2.3.4). After 1 s hold time (the timescale for the photoassociation) at the trap depths used in the experiment there are typically $40 \times 10^3 - 60 \times 10^3$ atoms left. The lowest temperature the sample is cooled to is ~ 600 nK and $T \approx 0.6 T_F$, where T_F is the Fermi temperature of a one component Fermi gas. This temperature, and a corresponding trap depth of about 4 μK, is fundamentally limited because the shallow dipole trap is not able to support atoms against gravity which causes atom loss and deterioration of the quality of the spectroscopic signal. Magnetic levitation, commonly used at non-zero magnetic fields to circumvent this issue, is not possible at low magnetic fields because the trapped states have opposite magnetic moments. It is possible to decrease the T/T_F ratio at 0 G by using a different design of the dipole trap and by improving the initial atom number, which would increase the Fermi temperature for a given trap depth. For example, Granade *et. al* [66] quotes $T \approx 0.48 T_F$ with about 10^5 atoms per spin state.

At $B = 0$, F and m_F are good quantum numbers, but to explicitly show the singlet and triplet character of the initial two-atom spin state $|i_0\rangle$ we follow Ref. [122] and represent it in the molecular basis ($|NSIJF\rangle$) shown in Fig. 4.4, such that $|i_0\rangle = \sqrt{1/3}|00000\rangle + \sqrt{2/3}|01110\rangle$.

The illumination time and light intensity I_1 of laser L_1 with frequency ν_1 (see Fig. 4.4) is chosen such that after 1 s L_1 induces a single color loss of 40% to 80% for intensities $100 - 500$ W/cm^2 corresponding to Rabi frequencies $\Omega_1 \ll$ 1 kHz. The intensity of L_2 ($20 - 200$ W/cm^2) is chosen so that the corresponding Rabi frequency $\Omega_2 \gg \Omega_1$ but also low enough ($\Omega_2 < 1$ MHz) to avoid inducing a large Autler-Townes splitting of the excited state. The frequency of L_2, ν_2, is set to match the $v'' = 9 \leftrightarrow v' = 20$ ($v'' = 38 \leftrightarrow v' = 31$) transition between the triplet(singlet) levels (Fig. 4.4) using the frequencies initially determined with the two-color photoassociation spectroscopy. The choice of the excited levels is based on empirical evidence that their ac Stark shift due to the field from laser L_1 is small in comparison with other levels measured in [49, 51]. Because there has been no prior high precision spectroscopy of the levels investigated in this thesis, our choice has been, to some extent, also a matter of convenience: the frequencies required for photoassociation to $v' = 20$ and $v' = 31$ are close enough such that it is easy to tune the Ti:Sapphire lasers when switching between the triplet and singlet potentials.
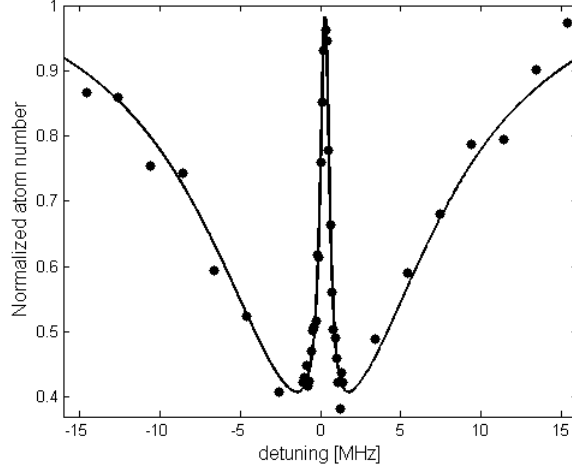
Figure 4.5: High resolution dark state spectra in a Fermi gas at 0 G with $T \approx 0.6\,T_F$. The observed feature corresponds to the $v'' = 38$, $N'' = 0$, $F'' = 0$ ro-vibrational level in the $X(1^1\Sigma_g^+)$ potential. The frequency ν_2 is fixed on the $v'' = 38$, $N'' = 0$ to $v' = 31$, $N' = 1$ bound-to-bound transition whereas ν_1 is scanned. The maximum revival appears when the two-photon condition is satisfied and the frequency difference $\nu_2 - \nu_1$ equals the difference between the energy of the initial free atoms state and ground state molecules. The intensity of I_2 of laser L_2 is kept low enough to avoid inducing a large Autler-Townes splitting.

The frequency ν_1 is scanned over a range that induces atom loss due to the single color photoassociation of free atoms to $v' = 20$ or $v' = 31$ vibrational levels. With L_2 on, dark state spectra are observed as shown in Fig. 4.5 and 4.6. It is worth noting that if the laser L_2 is detuned from a bound-to-bound transition the dark state spectra become asymmetric, but it has no influence on the determination of the binding energies. When the two-photon resonance condition is fulfilled an atom-molecule dark state is created and the loss induced by L_1 is almost completely suppressed for all levels but $|g_1\rangle = |v'' = 9, N'' = 0, F'' = 1\rangle$ where the suppression is only partial (Fig. 4.6b). We do not expect that the poor revival is caused by the finite collisional lifetime of $|g_1\rangle$ as it would have to be unreasonably short, $\sim 1\ \mu$s. This estimation comes from the fit of the 3-level model from the Eq. 4.18 to the dark state feature which returns the decay rate of the molecular level $\gamma_g \sim 1$ MHz.
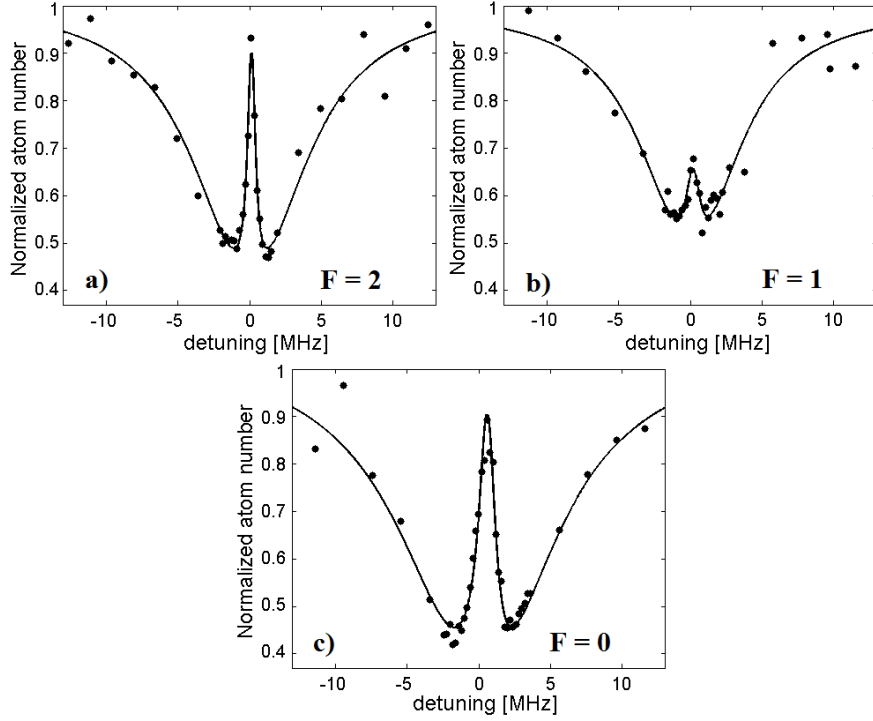
Figure 4.6: High resolution dark state spectra in a Fermi gas at 0 G with $T \approx 0.6\,T_{\mathrm{F}}$. The molecular hyperfine levels F (a–c), belong to the $v'' = 9$, $N'' = 0$ ro-vibrational level in the $a(1^3\Sigma_u^+)$ potential. The frequency v_2 is fixed on a $v'' = 9, N'' = 0$, $F'' = 2, 1, 0$ to $v' = 31$, $N' = 1$ bound-to-bound transition whereas v_1 is scanned. The maximum revival appears when the two-photon condition is satisfied and the frequency difference $v_2 - v_1$ equals the difference between the energy of the initial free atoms state and ground state molecules. The intensity of I_2 of laser L_2 is kept low enough to avoid inducing a large Autler-Townes splitting.

However, both γ_g and the Rabi frequency Ω_1 cannot be reliably determined for exposure time of the atoms to the photoassociation light longer than about $10\mu s$. For more details see Section 4.4.

4.3.1 $|v''=9, N''=0, F''=1\rangle$ revival - role of the dipole trap

Off-resonant transitions driven by the optical dipole trap could be, in principle, responsible for the loss of population from $|g_1\rangle$ and subsequent decrease in the revival of the dark state signal. The dipole trap (1064 nm, 9398.5 cm^{-1}) can couple the $|g_1\rangle$ state to an excited level in a triplet character molecular potential $c(1^3\Sigma_g^+)$ or $b(2^3\Sigma_g^+)$, as shown in Fig. 3.1. To the best of our knowledge the levels energetically closest to the frequency of the dipole trap can be found in the $c(1^3\Sigma_g^+)$ potential: $v'=5$ and $v'=6$ with binding energies $E_5 = -5674.9324$ cm^{-1} and $E_6 = -5436.1865$ cm^{-1}, respectively[3]. The dipole trap laser is therefore detuned from $v'=5$ by 170.3 cm^{-1} and from $v'=6$ by 68.4 cm^{-1}. These are predictions for rotational levels with $N'=0$ but because the rotational constant is negligible in comparison to the value of detunings, the energies E_5 and E_6 can be treated as energies of states with $N'=1$.

In order to estimate the scattering rate

$$\Gamma_{sc} = \frac{3\pi c^2}{2\hbar\omega_0^3}\left(\frac{\Gamma}{\Delta}\right)^2 I \qquad (4.10)$$

caused by the off-resonance excitation of molecules due to the dipole trap photons, the on-resonance scattering rate Γ

$$\Gamma = \frac{\omega_0^3}{3\pi\varepsilon_0\hbar c^3}|\langle e|\mu|g_1\rangle|^2 \qquad (4.11)$$

needs to be calculated. Here ω_0 is the angular frequency of the transition and Δ is the detuning of the laser with intensity I from this transition. c, $\hbar$ and ε_0 are the speed of light, Planck's constant and vacuum permittivity, respectively. To obtain the dipole matrix element between the ground $|g_1\rangle$ and the excited molecular state $|e\rangle$, $|\langle e|\mu|g_1\rangle|^2$, the wavefunctions for both states need to be known. However, to

---

[3]Private communication, Dr. N. S. Dattani

estimate an upper bound on the scattering rate Γ induced by the dipole trap, we assume that $|\langle e|\mu|g_1\rangle|^2$ is on the same order of magnitude as matrix elements for the $2S$ to $2P$ atomic transition at 671 nm (with frequency ω_0'). We have

$$\Gamma = \frac{\omega_0^3}{3\pi\varepsilon_0\hbar c^3}|\langle g_1|\mu|e\rangle|^2 \approx \left(\frac{\omega_0}{\omega_0'}\right)^3 \frac{\omega_0'^3}{3\pi\varepsilon_0\hbar c^3}|\langle 2s|\mu|2p\rangle|^2 = \left(\frac{\omega_0}{\omega_0'}\right)^3 \Gamma_{\text{atom}}. \quad (4.12)$$

As a result, $\Gamma = 0.25\Gamma_{\text{atom}} = 1.5$ MHz, where $\Gamma_{\text{atom}} = 5.9$ MHz [67]. For the dipole trap intensities used in dark state experiments (less than 13 kW/cm^2), we obtain scattering rates of up to 8 Hz and 50 Hz for detunings 170.3 cm-1 and 68.4 cm-1, respectively. The complete revivals on the two-photon resonance observed for $|v'' = 9, N'' = 0, F'' = 0\rangle$ and $|v'' = 9, N'' = 0, F'' = 2\rangle$ levels confirm that these scattering rates are negligible in our experiment. Moreover, when the frequency of L_2 is tuned to the $F = 1$ hyperfine level, the probed bound-to-bound transition differs by up to 152 MHz from the above mentioned cases. Unless the coupling of $F = 1$ to the excited state is orders of magnitude stronger than that of the other F levels (e.g. due to different selection rules that do not allow coupling of $F = 0$ and $F = 2$ to the excited level), it does not influence the scattering rate as the dipole trap is already far-detuned from any transition. Based on our analysis the dipole trap does not seem to be the cause of the observed poor revival of the $|v'' = 9, N'' = 0, F'' = 1\rangle$ level and further investigation of this effect is required.

4.3.2 Dark state lifetime

The recorded spectra reveal a complete suppression of loss on two-photon resonance even for illumination times close to 2 s. To create the dark states we turn the laser fields on and off in the following order: L_2 on, L_1 on, L_1 off, L_2 off; where the turn on or off times are ~150ns [4]. The turn on or off of L_1 is adiabatic for most of the cases; however, when the turn on or off of L_1 is non-adiabatic, we expect a loss of atoms due to the projection of the initial state onto the bright state (which decays immediately) and due to the projection of the dark state back onto the free

---

[4]The AOM turn on or off times are ~1μs. However, coupling the photoassociation light into a fiber results in the decreased effective turn on or off time.

atom state

$$P_{\text{loss}} = 1 - |\langle DS|a \rangle|^2 |\langle DS|a \rangle|^2 = 1 - \left(\frac{\Omega_2^2}{\Omega_1^2 + \Omega_2^2} \right)^2, \tag{4.13}$$

where $|DS\rangle$ is the initial dark state and $|\langle DS|a \rangle|^2$ is the probability that the dark state will survive the turn on (turn off) of laser L_1. When $\Omega_2 \gg \Omega_1$, this projection loss is $2(\Omega_1/\Omega_2)^2$.

Another loss mechanism results from non-adiabatic phase jumps of the lasers that lead to the projection of the atom-molecule state

$$|AM\rangle = \frac{\Omega_2|a\rangle - \Omega_1 e^{i\phi}|g\rangle}{\sqrt{\Omega_1^2 + \Omega_2^2}} \tag{4.14}$$

onto the new bright state

$$|BS\rangle = \frac{\Omega_1|a\rangle + \Omega_2|g\rangle}{\sqrt{\Omega_1^2 + \Omega_2^2}}. \tag{4.15}$$

Here, ϕ is the new relative phase between two lasers after the jump. The $|a\rangle$ and $|g\rangle$ are the initial atomic state and a molecule in the ground state, respectively. This mechanism amounts to the loss of population from the initial state $|AM\rangle$ that equals

$$|\langle AM|BS\rangle|^2 = \frac{2\Omega_1^2 \Omega_2^2 (1 - \cos(\phi))}{(\Omega_1^2 + \Omega_2^2)^2}. \tag{4.16}$$

We can model the phase jitter of the lasers as producing a non-adiabatic jump of the relative phase by an average $\phi = \pi/2$ every dephasing time $\tau \sim 1/\Delta \nu = 6.2\ \mu$s.[5] After the time T this causes loss of the initial atom number N_i

$$P_{\text{jitter}} = \frac{N_i}{N} = \left(1 - \frac{2\Omega_1^2 \Omega_2^2}{(\Omega_1^2 + \Omega_2^2)^2} \right)^{T/\tau}. \tag{4.17}$$

For the experiments in the weakly interacting regime we chose $\Omega_2/\Omega_1 > 1000$.

---

[5] $\Delta \nu = 160$ kHz is the relative linewidth of the photoassociation lasers used to create the dark state, see Section 2.2.5.

Under this condition, the atom loss is expected to be on the order of 10% after 350 ms. [6] However, this simple model underestimates the observed dark state lifetime, because even after 2 s we can still observe near complete revivals on the two photon resonance. We note that to the best of our knowledge the longest times reported in experiments with other species rarely exceed few tens of ms.

4.4 Binding energies of the least bound states

To determine the ac Stark shifts induced by the lasers L_1, L_2 and the dipole trap, the dark state spectra are measured for several dipole trap depths with the control(probe) beam intensity 50(350) W/cm^2. At the lowest trap depth, additional spectra are measured when both the control and the probe beam intensities are varied. A three-level model (as in e.g. [140])

$$
\begin{aligned}
i\dot{a} &= -\Omega_1 a^* b, \\
i\dot{b} &= [(\Delta + \delta) - i\gamma_b/2]b - \frac{1}{2}(\Omega_1 aa + \Omega_2 g), \\
i\dot{g} &= (\delta - i\gamma_g/2)g - \frac{1}{2}\Omega_2 b,
\end{aligned}
\tag{4.18}
$$

describing the normalized field amplitudes a, b, and g of the initial state, the excited molecular and ground state, respectively, is numerically fitted to each data set to extract the two-photon resonance position. The resulting values for each set of control and probe beam intensities are used to extract the field free binding energies which are summarized in Table 4.1.

Due to the long time scale of the experiment (1 s) which exceeds, by orders of magnitude, the timescales associated with the decay rates γ_b, γ_g and Rabi frequencies Ω_1, Ω_2, simulating the full, 1 s long evolution of the system is too time consuming to be practical with a use of a desktop computer. For that reason the evolution of the system is simulated for up to 10 μs and as a result the 3-level model (Eq. 4.18) cannot be reliably used to extract Ω_1 and γ_g. However, the two-photon resonance is time scale independent therefore its determination is reliable.

---

[6]In our setup, 10% loss of atoms is usually indiscernible due to the shot-to-shot atom number variation.

Table 4.1: Experimentally measured binding energies of the least bound vibrational levels of the $a(1^3\Sigma_u^+)$ and $X(1^1\Sigma_g^+)$ potentials of $^6\text{Li}_2$. The frequency difference $\nu_2 - \nu_1$ is extracted from the dark state spectra and corresponds to the energy difference between the initial and the final state. The initial free atomic state is $2a_{2S}$ below the hyperfine center of gravity of the $2S_{1/2} + 2S_{1/2}$ asymptote therefore the actual binding energy is computed by adding $2a_{2S} = 304.274$ MHz to the measured frequency difference. The quoted uncertainties represent the statistical uncertainties on the fits. The systematic uncertainty is below 1 kHz.

v''	F''	$\nu_2 - \nu_1$ [GHz]	Binding energy [GHz]
		$X(1^1\Sigma_g^+)$	
38	0	1.321671(21)	1.625945(21)
		$a(1^3\Sigma_u^+)$	
	2	24.010649(46)	24.314923(46)
9	1	24.163035(105)	24.467309(105)
	0	24.238372(54)	24.542646(54)
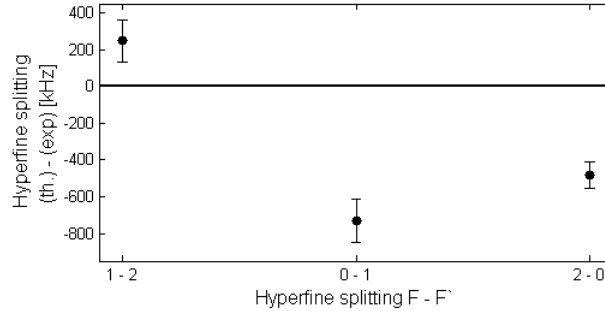
Figure 4.7: The difference between the predicted (based on Eq. 4.20) and measured molecular hyperfine splittings in the $v'' = 9$, $N'' = 0''$ level in the $a(1^3\Sigma_u^+)$ potential. The horizontal line corresponds to a perfect agreement with theory and the uncertainties result from the uncertainties of the determination of the binding energies of molecular hyperfine levels.

The dark state spectroscopy is a differential measurement; therefore only the absolute frequency difference of the lasers L_1 and L_2 needs to be known precisely. The resulting systematic uncertainty is therefore on the order of 1 kHz, as discussed in Section 2.2.5. We note that the standard spin-dependent Hamiltonian of two non-interacting atoms [104, 166]

$$H = \frac{a_{2S}}{2}(\vec{s}_1 \cdot \vec{i}_1 + \vec{s}_2 \cdot \vec{i}_2) = \frac{a_{2S}}{2}\left(\frac{1}{2}\vec{S}\cdot\vec{I} + \frac{1}{2}(\vec{s}_1 - \vec{s}_2)\cdot(\vec{i}_1 - \vec{i}_2)\right) \qquad (4.19)$$

with associated energies of a state $|NSIJF\rangle$

$$E_{|NSIJF>} = \frac{a_{2S}}{4}[F(F+1) - S(S+1) - I(I+1)] \qquad (4.20)$$

predicts molecular hyperfine splittings (Fig. 4.4) that differ from those inferred from the binding energies listed in Table 4.1 by more than can be explained by the uncertainties of our measurements, thus providing a possible reference for refinements of molecular hyperfine structure models. The disagreement cannot be caused by a systematic shift of unknown origin; see Figure 4.7. In order for all of our data to agree with theory the uncertainties would have to be increased by a factor of seven, which cannot be justified.

4.5 Binding energy of $v'' = 37, N'' = 0$

At magnetic fields above the Feshbach resonance at $B = 543.3$ G the energy of the $v'' = 38, N'' = 0$ molecular level becomes nearly degenerate with the energy of the two colliding atoms in states $|1\rangle$ and $|2\rangle$. This leads to the coupling between $v'' = 38, N'' = 0$ level and the atoms in the entrance channel, resulting in a broad Feshbach resonance at $B = 832.18$ G [85] (see Section 4.6). Above this field $v'' = 38, N'' = 0$ is no longer bound and $v'' = 37$ becomes the least bound molecular level in the singlet potential. [7]

Theoretical studies of dark states in degenerate Fermi gases in the BEC-BCS crossover regime (e.g. [158, 159]) rely on molecular levels in the $X(1^1\Sigma_g^+)$ potential therefore the knowledge of the binding energy of $v'' = 37, N'' = 0$ at various

---

[7] see e.g., a review paper devoted to Feshbach resonances by Chin *et al.* [118]
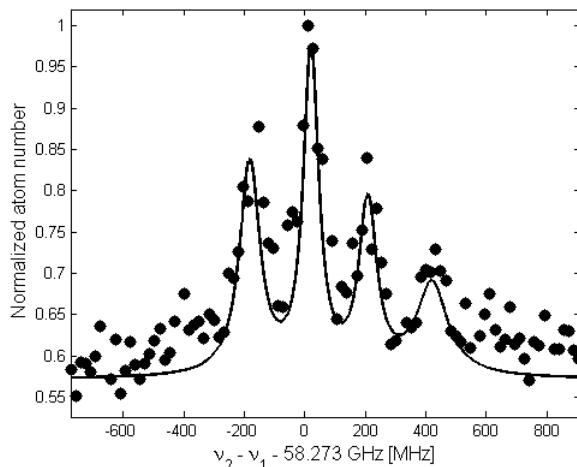
Figure 4.8: The normalized ^{6}Li atom number in two color photoassociation spectroscopy of the $v'' = 37$, $N'' = 0$ ro-vibrational level in the $X(1^1\Sigma_g^+)$ potential. The data shows an early attempt to measure the binding energy of this level and high dipole trap and L_2 intensities are used to facilitate the detection. The lasers L_1 ($I_1 = 0.1$ kW/cm^2) with frequency v_1 and L_2 ($I_2 = 2.5$ kW/cm^2) with frequency v_2 are both locked to the frequency comb. Laser L_1 induces constant loss by driving transition from an initial unbound molecular state with $N = 0$, $G = 0$ to the $v' = 31$ vibrational level of the $1^1\Sigma_u^+$ excited state with $N' = 1$, $G' = 0$. The frequency v_2 is varied across the $v' = 31$ to $v'' = 37$ transition. The dipole trap intensity is 54 kW/cm^2 corresponding to the sample temperature of about 2 μK. The bias magnetic field is set to 0 G. The lines are guides for the eye.

magnetic fields is essential. This level has been treated as "known" because the theoretical potentials for ^{6}Li$_2$ are quite well developed and some low accuracy measurements (± 150 MHz at best) are available [131]. It is worth noting that as recently as in 2012 Wu and Thomas used for their calculations 53.5 GHz [158] and 55.8 GHz [159] as the energy difference between $v'' = 37$ and $v'' = 38$. Our measurements, however, indicate that this difference at 0 G is 56.938(1) GHz (Table 4.2). The discrepancy does not change the conclusion of [158] and [159] but from the point of view of an experimentalist setting up an experiment the improved measurements of the required binding energies are essential to making their pro-

105
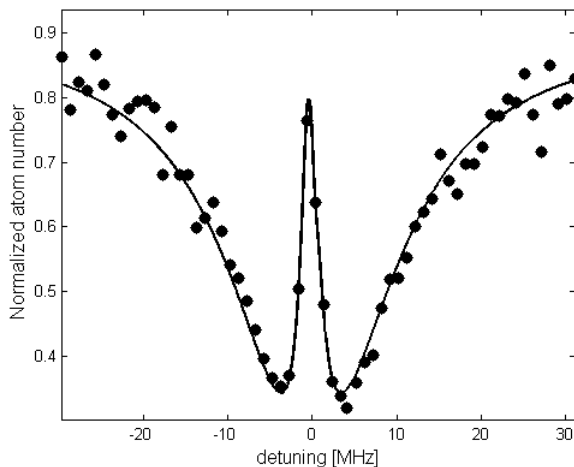
Figure 4.9: High resolution dark state spectrum associated with the $v'' = 37, N'' = 0$ ro-vibrational level in the $X(1^1\Sigma_g^+)$ potential. The frequency v_2 of the laser L_2 is fixed on the $v'' = 37$, $N'' = 0$ to $v' = 31$, $N' = 1$ transition while the frequency v_1 of the laser L_1 is scanned over the free to bound transition (free atoms to $v' = 31$, $N' = 1$). The intensity of L_2 is kept low enough to avoid inducing a large Autler-Townes splitting.

posal more feasible. The experimental determination of the binding energy of $v'' = 37$, $N'' = 0$ and $v'' = 38$, $N'' = 0$ performed by our group has been guided by theoretical calculations performed by Dr. Nikesh S. Dattani. As an illustration of the power of modern theoretical techniques it is worth mentioning that the energy difference between $v'' = 37$, $N'' = 0$ and $v'' = 38$, $N'' = 0$ predicted by Dr. Dattani's calculations is 57.002 GHz (predictions were independent of our high precision experiments).

The initial, very coarse, determination of the binding energy of $v'' = 37$, $N'' = 0$ at 0 G has been performed using two-color photoassociation technique. The lasers L_1 ($I_1 = 0.1$ kW/cm^2) with frequency v_1 and L_2 with frequency v_2 are locked to the frequency comb. Laser L_1 induces constant loss by driving transition from an initial unbound molecular state with $N = 0$, $G = 0$ to the $v' = 31$ vibrational level of the $1^1\Sigma_u^+$ excited state with $N' = 1$, $G' = 0$. The frequency v_2 of the laser L_2 ($I_2 = 2.5$ kW/cm^2) is varied across the $v' = 31$ to $v'' = 37$ transition. The dipole trap

Table 4.2: The energy difference between the initial state $|i_c\rangle$ (Feshbach molecules or BCS-like pairs, Eq. 4.21) and the final singlet state $|g\rangle$ (corresponding to $v'' = 37$, $|00011\rangle$) measured at selected magnetic fields. The uncertainties are conservatively estimated to be 1 MHz. Theoretical values are obtain by adding the Zeeman shifts of states $|1\rangle$ and $|2\rangle$ to the experimental value obtained at $B = 0$ G.

B [Gauss]	0	754	804	838.8
$\nu_2 - \nu_1$ [GHz] (exp.)	58.260	56.364	56.225	56.127
$\nu_2 - \nu_1$ [GHz] (th.)	–	56.3637	56.2242	56.1271
(th.) - (exp.) [MHz]	–	0.3	0.8	0.1

intensity is 54 kW/cm^2 corresponding to the sample temperature of about 2 μK. When the frequency ν_2 equals the energy difference between $v' = 31$, $N' = 1$ and $v'' = 37$, $N'' = 0$ the level $v' = 31$, $N' = 1$ becomes detuned from the frequency ν_1 resulting in the suppression of the atom loss, shown in Fig. 4.8. As a result, $\nu_2 - \nu_1$ can be interpreted as a frequency difference between the free atoms and $v'' = 37$, $N'' = 0$. This measurement has been verified and improved upon by performing a dark state spectroscopy with L_2 fixed on $v'' = 37$, $N'' = 0$ to $v' = 31$, $N' = 1$ transition and with the frequency of L_1 scanned across the $v' = 31$, $N' = 1$ photoassociation line, as in Section 4.3. The resulting dark state spectrum taken at the sample temperature of 800 nK can be seen in Fig. 4.9. The measurement of the binding energy of $v'' = 37$ has not been performed as rigorously as for $v'' = 9$ and $v'' = 38$ described in Section 4.3 - the ac Stark effect induced by the photoassociation lasers and the dipole trap has not been systematically studied. However, based on our experience with the least bound states and given low intensities I_1, I_2 and the dipole trap, the measured value is very conservatively estimated to have accuracy of 1 MHz. This accuracy is sufficient for all practical purposes because it is much less than the width of the excited state level $v' = 31$ and as a result only fine tuning of frequency is required if the conditions change (if e.g., different dipole trap intensity is used). To the best of our knowledge the binding energy of this level has never been reported before in the context of ultracold lithium.

The dark state spectroscopy has been performed for a range of magnetic fields (described in details in Section 4.6) and the energy difference between the $|g\rangle =$

$|v'' = 37, N'' = 0\rangle$ and the initial state $|i\rangle$ at selected magnetic fields is summarized in Table 4.2). Our observations are consistent with the expectation that the energy difference $E_{|g\rangle} - E_{|i\rangle}$ is caused solely by the Zeeman shift of the initial state $|i\rangle$ since the bound molecular state is expected to have no magnetic moment.

4.5.1   Unexpected features in the $v'' = 37$, $N'' = 0$ spectrum

The multi-peak structure observed in the two-color photoassociation spectrum of the $v'' = 37$, $N'' = 0$ level (Fig. 4.8) at 0 G came as a surprise. This level is not expected to have any degeneracies that could be lifted by the high intensities of L_2 (due to $F = 0$) therefore the structure of the signal might come from coupling of $v' = 31$ to some other excited molecular potential by laser L_2. The multi-peak signal, however, goes away when I_2 is reduced by a factor of ≈ 20, resulting in a single peak corresponding to $v_2 - v_1 \approx 58.260$ GHz. The disappearance of the anomalous spectrum when I_2 is decreased warranted focusing on other, more important, scientific goals, therefore a detailed study of the observed spectrum has not been performed.

4.6   Exotic dark states in the BEC-BCS crossover

When the final evaporation is done at magnetic fields close to the broad FR at $B = 832.18$ G, pairs form, here referred to as Feshbach molecules below (where a two-body bound state exists) and BCS-like pairs above resonance (where pairing is a many-body phenomenon). In this case, the initial Feshbach-dressed molecule or pair state is

$$|i_c\rangle = \sqrt{Z}|g_{\text{closed}}\rangle + \sqrt{1-Z}|g_{\text{open}}\rangle, \tag{4.21}$$

where the open channel has almost a pure triplet character and is strongly coupled to the closed channel molecular state responsible for the wide FR, $|g_{\text{closed}}\rangle \equiv (2\sqrt{2}|00000\rangle - |00200\rangle)/3$, a linear combination of the $I = 0$ and 2 ($v'' = 38$) singlet states [122, 159]. To form dark states, we use the singlet levels $|e\rangle$ ($v' = 31$, $|00011\rangle$) and $|g\rangle$ ($v'' = 37$, $|00011\rangle$) mainly because of their insensitivity to the magnetic field.
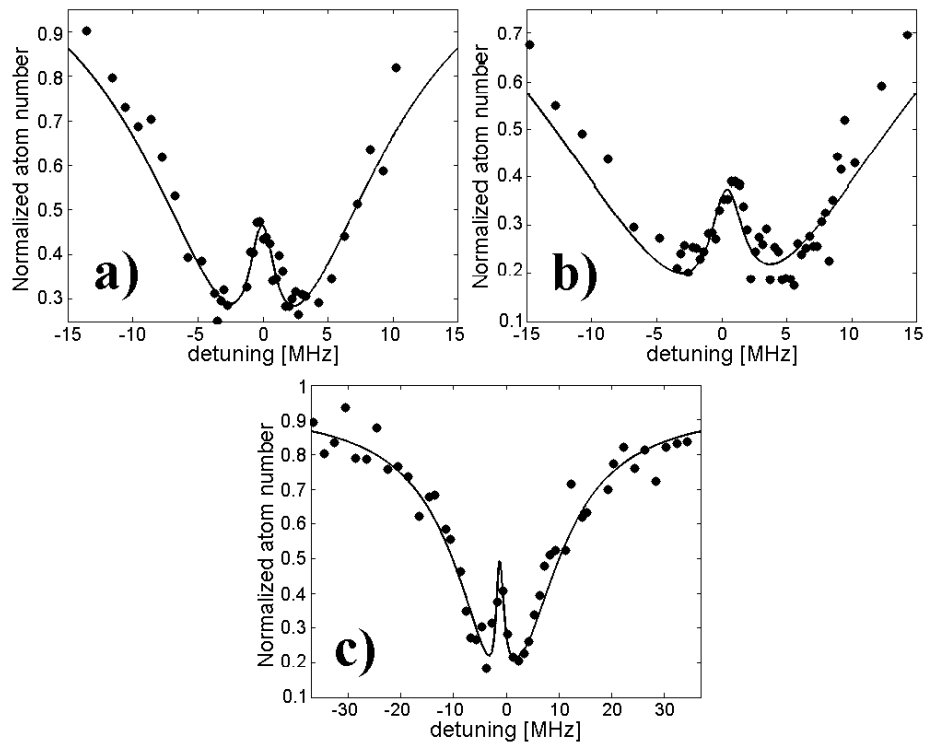
Figure 4.10: Dark state spectra observed at selected magnetic fields in a partially Bose condensed sample of Feshbach molecules of ^{6}Li using transitions between singlet molecular potentials. The photoassociation light is on for 100 ms for measurements at magnetic fields (a) $B = 754$ G and (b) $B = 804$ G. (c) Magnetic field is set to $B = 754$ G and the photoassociation lasers are on for 5 μs, the timescale relevant to STIRAP. The change of the exposure time by over four orders of magnitude does not seem to change the dark state feature. No parameters have been found that would improve the revival on the two photon resonance.
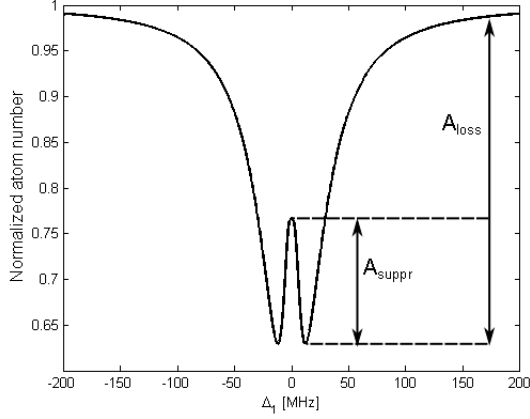
Figure 4.11: A generic dark state spectrum showing quantities defining the revival height as the ratio of the amplitude of the suppression signal A_{suppr} to the amplitude of the loss signal A_{loss}

4.6.1 Dark states in a BEC of Feshbach molecules

The evaporation on the molecular side of the $B = 832.18$ G FR allows us to create a mixture of Feshbach molecules and a Bose-Einstein condensate of Feshbach molecules. For intensities $I_1 = 0.045$-10 kW/cm^2 and $I_2 = 0.040$-0.3 kW/cm^2, and illumination times 5μs to 100 ms (short times correspond to large I_1) we observe dark state features that show only partial loss suppression on the two-photon resonance. Figure 4.10 shows the observed features at 754 G and 805 G for the photoassociation light exposure times of 5 μs and 100 ms. Both Ω_1 and Ω_2 as well as the exposure time have been varied over a range where a full revival is expected. Nevertheless, we always observe revival heights below 50%, even for temperatures above the mBEC critical temperature ($T > T_C$). For the purpose of further discussion we define the revival height as the ratio of the amplitude of the suppression signal A_{suppr} to the amplitude of the loss signal A_{loss} (see Fig. 4.11).

4.6.2 Dark states in a degenerate Fermi gas

When a degenerate Fermi gas is prepared above the resonance (here at 839 G) such that there are BCS-like pairs present we observe dark state features corresponding to a coherent superposition of these pairs and molecules in the $|g\rangle$ level of the

110
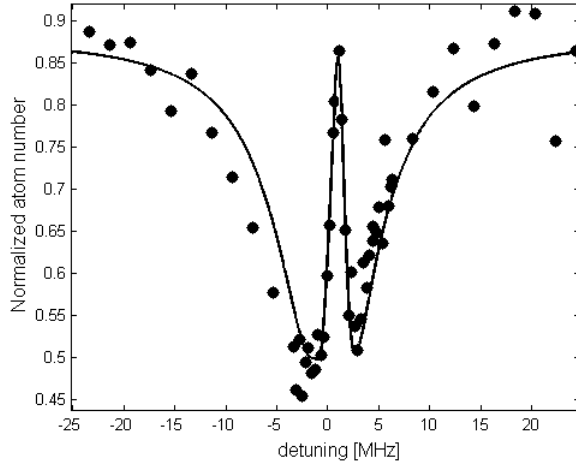
Figure 4.12: A dark state spectrum at $B = 839$ G observed after 5 μs exposure time to the photoassociation light in a BCS-like paired ^{6}Li using transitions between singlet molecular potentials. Here $\Omega_1/2\pi = 5$ kHz and $\Omega_2/\Omega_1 \sim 1000$. The full revival is in stark contrast with the results obtained below the Feshbach resonance at $B = 832.18$ G.

singlet potential (Fig. 4.12). As this is the first ever observation of such an exotic quantum superposition it has not been obvious *a priori* if dark states can be created without disrupting the many-body pairing physics by the photoassociation light from two lasers. The destruction of pairing is a possibility and the observed dark state would then be between "regular" strongly interacting two component Fermi gas and ground state molecules.

To verify the persistence of the BCS-like pairing the frequencies ν_1 and ν_2 are set to match the two-photon condition where negligible dark-state tuning of the scattering length is expected and rf spectroscopy with 200 ms long rf pulses is performed, revealing a spectrum consistent with the presence of pairing [74]. Here, $\Omega_1/2\pi = 5$ kHz and $\Omega_2/\Omega_1 \sim 1000$, thus the BCS-like pairs were only weakly dressed with the $|g\rangle$ level, and the many-body interactions were, thus, negligibly perturbed and no change of the spectrum that could be associated with the presence of the dark state has been observed, as revealed in Fig. 4.13.
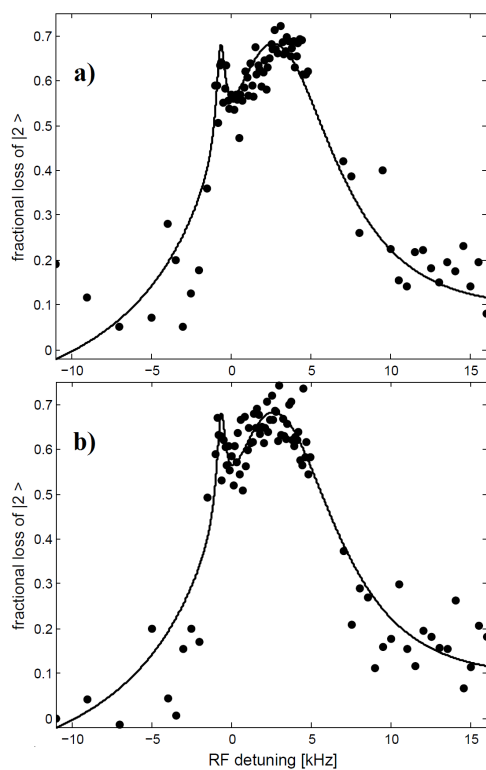
Figure 4.13: a) RF spectroscopy of BCS pairs of ^{6}Li at 839 G, the narrow peak at -1 kHz corresponds to the $|2\rangle \rightarrow |3\rangle$. transition whereas the broad peak is associated with breaking BCS pairs, b) the frequencies of the lasers L_1 and L_2 are set to a two photon resonance creating a coherent superposition of BCS pairs and singlet ground state molecules at 839 G. RF spectroscopy confirms the persistence of pairing for this exotic BCS pair- ground state molecule dark-state. The lines shown on both plots are the same functions and are intended only as a guide to the eye.

4.6.3 Dark states in the BEC-BCS crossover

The revival height on the two-photon resonance has been studied in the BEC-BCS crossover regime using $\Omega_1 = 200$ kHz, $\Omega_2 \simeq 2$ MHz, and exposure time of 40 μs. Figure 4.14(top) shows that the revival height changes abruptly for fields below 829 G. This change, coincidentally, occurs at magnetic fields where the two-body bound state is present. However, we observe a near full revival also below the Feshbach resonance center at $B = 832.18$ G [85]. This abrupt change in the revival height was unexpected, and we, therefore, independently checked that Ω_1 is continuous in this regime by performing single-color photoassociation $|i_c\rangle$ to $|e\rangle$. Only the $I = 0$ part of the closed channel contributes to photoassociation to $|e\rangle$; therefore

$$\Omega_1(B) = \langle i_c|\vec{d}\cdot\vec{E}|e\rangle = \sqrt{Z}\langle g_{\text{closed}}|\vec{d}\cdot\vec{E}|10011\rangle_{v'=31} \tag{4.22}$$

$$= \sqrt{Z}\sqrt{\frac{8}{9}}\langle 00000_{v''=38}|\vec{d}\cdot\vec{E}|10011\rangle_{v'=31} = \sqrt{\frac{8Z}{9}}\Omega_0,$$

We determine Ω_0 experimentally from a fit of the measured dark-state spectra at $B = 0$ shown in Fig. 4.5. In that spectra, Ω_0 plays the role of the bound-to-bound coupling Ω_2. We observe that $Z \equiv (9/8)(\Omega_1/\Omega_0)^2$ [shown in Fig. 4.14(bottom)] is continuous in the region where the dark state revival changes abruptly. Our observations are consistent with those reported by Partridge *et al.* [99] where a much more weakly bound excited state $v' = 68$ was used. However, our determination of Z does not rely on the calculation of Ω_0 and thus is independent of a theoretical model for the molecular potentials.

As of now, the source of the sudden change of the revival height in the vicinity of the Feshbach resonance cannot be explained and this issue requires further investigation, possibly leading to a new understanding of the BEC-BCS crossover theory.
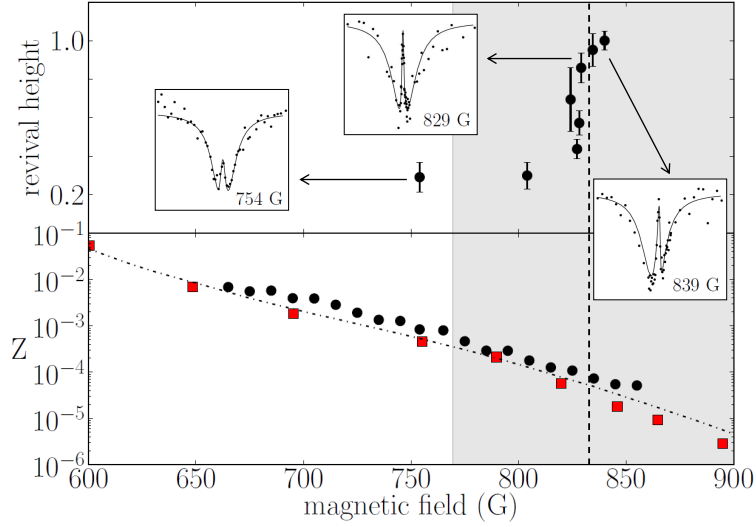
Figure 4.14: (top) The revival height of the dark state features defined as a ratio of the suppression amplitude to the loss amplitude, measured on both sides of the $B = 832.18$ G Feshbach resonance (dashed vertical line). The states involved are Feshbach molecules or BCS-like pairs ($|i_c\rangle$), $v' = 31$ in the $A(1^1\Sigma_u^+)$ excited molecular potential ($|e\rangle$) and $v'' = 37$ in the $X(1^1\Sigma_g^+)$ ground-state potential ($|g\rangle$). For magnetic fields above 829 G, we observe near complete revival on the two-photon resonance. Insets: dark states feature at selected magnetic fields: 754 G, 829 G and 839 G. (bottom) Full circles represent the probability Z of the dressed molecule to be in the bare molecular state in the closed channel of the Feshbach resonance. Squares (red) show Z measured by Partridge *et al.* [99] where the excited state $|e\rangle$ is $v' = 68$ [$A(1^1\Sigma_u^+)$ potential]. Dash-dotted line shows theoretical prediction for Z taken from digitized Fig. 8 in [182]. The grey region corresponds to $k_F|a| > 1$. For these data, $T/T_F = 0.4 \pm 0.15$, $E_F/h = 11$ kHz, $\Omega_1 = 200$ kHz, and $\Omega_2 \simeq 2$ MHz. Figure taken from [52].

114

Chapter 5

Summary and outlook

The results presented in this thesis have led to the development of experimental tools and methods that eventually will enable our laboratory to perform cutting edge experiments with ultracold molecules formed from ultracold atoms. Triggered by the goal of creating ground state polar molecules of ^{6}Li^{85}Rb we used ^{6}Li to test certain technical aspects of our setup and develop know-how that up until this work had not been available at the University of British Columbia (and for most part in Canada). These technical aspects cover primarily:

- The demonstration of a Bose-Einstein condensate (of weakly bound Feshbach molecules), as well as a strongly interacting degenerate Fermi gas in the regime where BCS-like pairing is present. This has been achieved in a drastically simplified experimental setup, where the magneto-optical trap is loaded from an oven located in the same chamber as the region where the experiments are performed. It defied the generally accepted rule that the atomic source and the experimental section need to be separated by a differential pumping stage for experiments with degenerate quantum gases.

- The setup of a laser system for the single and two-photon manipulation of atoms. It consists of two tunable Coherent 899-21 Ti:Sapphire lasers phase locked to a GPS disciplined femtosecond frequency comb. The system has been tested on ^{6}Li and is now ready for experiments leading to the production of ground state molecules. Long term, it will enable experiments with other species, notably a ^{6}Li and ^{85}Rb mixture.

The high precision single color photoassociation spectroscopy presented in this thesis resulted in a significant improvement of the models describing the c($1^3\Sigma_g^+$) and A($1^1\Sigma_u^+$) ^{6}Li potentials. The experimental demonstration of the enhancement

of the photoassociation rate in the vicinity of a p-wave Feshbach resonance extends the scope of Feshbach Optimized Photoassoaciation (FOPA) method beyond the s-wave regime.

The demonstration of atom-molecule and molecule-molecule dark states in degenerate gases of fermionic lithium extends the range of systems where such superposition states have been created and enables realization of theoretical proposal exploiting dark states as tools for optical control of interactions and probing of the superfluidity and pairing. For the past decade, ^{6}Li has been a work horse in the field of strongly interacting Fermi gases, therefore new probing techniques based on dark states could potentially have a significant impact on the field.

The measurement of the binding energies of the least bound states of the lowest singlet and triplet potentials $X(1^1\Sigma_g^+)$ and $a(1^3\Sigma_u^+)$, respectively, provides the most precise spectroscopic measurements of these levels so far, with accuracies reaching 20 kHz. The observed anomaly of the molecular hyperfine splittings in the $v'' = 9$ vibrational level of the $a(1^3\Sigma_u^+)$ state will require additional investigation to reconcile the observed difference between our measurements and theoretical calculations.

Finally, this work puts lithium in the spotlight as a system that could be used to produce a Bose-Einstein condensate of ground state molecules in the ro-vibrational ground state. As opposed to other species (bosonic atoms or Bose-Fermi mixtures) studied by many groups, the starting point for the transfer of the initial state using stimulated Raman adiabatic passage (STIRAP), long-lived sample of a Bose-Einstein condensate of Feshbach molecules, can be relatively easily achieved. This approach may result in a transfer directly into a degenerate gas of ground state molecules, without a need for additional cooling of molecules. Furthermore, Li_2 is one of the simplest dimers and creation of Li_2 in the ultracold regime could lead to experiments that would enrich our understanding of molecular physics, therefore also potentially impacting chemistry.

5.1   Future experiments

After over six years of service, we decided to upgrade the experimental setup used in this thesis and as a result the rebuild of the vacuum system and the lithium laser

system is under way. The long term goal of creating ground state molecules of $^6\text{Li}^{85}\text{Rb}$ will benefit from the separation of atom sources from the science chamber (this would be unnecessary if we were to work only with lithium). By loading the magneto-optical trap from a slow atom source (Zeeman slower) not only will we increase the trapped atom number but, more importantly, we will decrease the experimental cycle duration from $10 - 15$ s to < 5 s, significantly decreasing data acquisition cycle. The optimization of the dipole traps, the improvement of the optical access and an improved imaging system will lead to a much larger samples of degenerate gases, imaged with better resolution and signal-to-noise ratio. The details of this upgrades will be presented in a Master's thesis of William Bowden and a Doctoral thesis of Will Gunton.

From the scientific point of view, the work presented here has been a necessary step towards experiments involving lithium molecules and, in a broader sense, control of atomic (especially fermionic) systems with laser fields. The research that is expected to be a natural continuation of this thesis will focus on the following:

- Transfer of atoms from a standard magneto-optical trap based on the D_2 line into a D_1 line based trap, thus enabling sub-Doppler cooling mechanisms due to well resolved hyperfine structure of the excited $2^2P_{1/2}$ level. This should lead to a decreased temperature of the sample and increased phase space density, and as a result a more efficient transfer into the dipole trap. Similar approaches applied recently to e.g. ^{39}K [183], ^{40}K [184] and ^7Li [185, 186] show a great promise of this method.

- We have performed preliminary measurements (with resolution ~5 MHz) of the binding energies of $N'' = 0, 2$ rotational levels of all vibrational levels ($v'' = 0$ to $v'' = 9$) in the $a(1^3\Sigma_u^+)$ molecular potential. It makes it one of the most accurately measured molecular potentials. Using dark state spectroscopy described in Chapter 4 would allow further improvement of the determination of binding energies (with accuracy ~100 kHz), providing experimental data useful for tests of *ab initio* calculations of molecular energies. Moreover, the discrepancy between the theory and experiment observed in the molecular hyperfine structure of the $v'' = 9, N'' = 0$ level (see Section 4.4) indicates that high accuracy (~100 kHz) measurements could be a reference

117

for the refinement of the molecular theory.

- Our laser system allows us to measure binding energies of the $N'' = 0, 2$ rotational levels of $v'' = 26$ to $v'' = 38$ vibrational levels in the $X(1^1\Sigma_g^+)$ molecular potential. The expected accuracy on the order of 20 kHz (as demonstrated for $v'' = 38, N'' = 0$, see Section 4.4) would be at least four orders of magnitude better than the data available so far. With the precision spectroscopy covering almost 1/3 of the potential depth, this would make $X(1^1\Sigma_g^+)$ one of the best known molecular potentials.

- The demonstration of the dark states in ^{6}Li and the measurement of the binding energy of the $v'' = 37$ level in the $X(1^1\Sigma_g^+)$ potential (see Section 4.5) are the first (and absolutely necessary) steps towards experimental realization of a proposal utilizing dark states for optical control of Feshbach resonances [158].

- Finally, converting a Bose-Einstein condensate of Feshbach molecules into a Bose-Einstein condensate of the triplet ground state molecules is a major research goal of our group. Since all the hardware is already in place, as well as a necessary know-how has been acquired, performing STIRAP is one of the most important steps that will be taken after the upgrade is finalized.

References

[1] M. H. Anderson, J. R. Ensher, M. R. Matthews, C. E. Wieman, and E. A. Cornell. Observation of Bose-Einstein condensation in a dilute atomic vapor. *Science*, **269**(5221):198–201, 1995. pages 1, 11, 32

[2] K. B. Davis, M. O. Mewes, M. R. Andrews, N. J. van Druten, D. S. Durfee, D. M. Kurn, and W. Ketterle. Bose-Einstein condensation in a gas of sodium atoms. *Phys. Rev. Lett.*, **75**:3969–3973, Nov 1995. pages 1, 32

[3] C. C. Bradley, C. A. Sackett, J. J. Tollett, and R. G. Hulet. Evidence of Bose-Einstein condensation in an atomic gas with attractive interactions. *Phys. Rev. Lett.*, **75**(9):1687–1690, Aug 1995. pages 1

[4] Immanuel Bloch, Jean Dalibard, and Wilhelm Zwerger. Many-body physics with ultracold gases. *Reviews of Modern Physics*, **80**(3):885, 2008. pages 1

[5] J.R. Anglin and W. Ketterle. Bose–Einstein condensation of atomic gases. *Nature (London)*, **416**:225, 2002. pages 1

[6] Wolfgang Ketterle and Martin W. Zwierlein. Making, probing and understanding ultracold Fermi gases. *RIVISTA DEL NUOVO CIMENTO*, **31**:247–422, May-June 2008. pages 1

[7] J. B. Fixler, G. T. Foster, J. M. McGuirk, and M. A. Kasevich. Atom interferometer measurement of the Newtonian constant of gravity. *Science*, **315**(5808):74–77, 2007. pages 1

[8] G. Rosi, F. Sorrentino, L. Cacciapuoti, M. Prevedelli, and G. M. Tino. Precision measurement of the Newtonian gravitational constant using cold atoms. *Nature*, **510**(7506):518–521, June 2014. pages 1

[9] C. S. Wood, S. C. Bennett, D. Cho, B. P. Masterson, J. L. Roberts, C. E. Tanner, and C. E. Wieman. Measurement of parity nonconservation and an anapole moment in cesium. *Science*, **275**(5307):1759–1763, 1997. pages 1

[10] Holger Müller, Achim Peters, and Steven Chu. A precision measurement of the gravitational redshift by the interference of matter waves. *Nature*, **463**:926–929, February 2010. pages 1

119

[11] A. Einstein, B. Podolsky, and N. Rosen. Can quantum-mechanical description of physical reality be considered complete? *Phys. Rev.*, **47**:777–780, May 1935. pages 1

[12] A. Robert, O. Sirjean, A. Browaeys, J. Poupard, S. Nowak, D. Boiron, C. I. Westbrook, and A. Aspect. A Bose-Einstein condensate of metastable atoms. *Science*, **292**(5516):461–464, 2001. pages

[13] Johannes Kofler, Mandip Singh, Maximilian Ebner, Michael Keller, Mateusz Kotyrba, and Anton Zeilinger. Einstein-Podolsky-Rosen correlations from colliding Bose-Einstein condensates. *Phys. Rev. A*, **86**:032115, Sep 2012. pages 1

[14] C. W. Chou, D. B. Hume, J. C. J. Koelemeij, D. J. Wineland, and T. Rosenband. Frequency comparison of two high-accuracy Al^+ optical clocks. *Phys. Rev. Lett.*, **104**:070802, Feb 2010. pages 2

[15] Alan A. Madej, Pierre Dubé, Zichao Zhou, John E. Bernard, and Marina Gertsvolf. $^{88}Sr^+$ 445-THz single-ion reference at the 10^{17} level via control and cancellation of systematic uncertainties and its measurement against the SI second. *Phys. Rev. Lett.*, **109**:203002, Nov 2012. pages 2

[16] N. Hinkley, J. A. Sherman, N. B. Phillips, M. Schioppo, N. D. Lemke, K. Beloy, M. Pizzocaro, C. W. Oates, and A. D. Ludlow. An atomic clock with 10^{18} instability. *Science*, **341**(6151):1215–1218, 2013. pages 2

[17] B. J. Bloom, T. L. Nicholson, J. R. Williams, S. L. Campbell, M. Bishof, X. Zhang, W. Zhang, S. L. Bromley, and J. Ye. An optical lattice clock with accuracy and stability at the 10^{-18} level. *Nature*, **506**:71–75, February 2014. pages 2

[18] Alexander D. Cronin, Jörg Schmiedmayer, and David E. Pritchard. Optics and interferometry with atoms and molecules. *Rev. Mod. Phys.*, **81**:1051–1129, Jul 2009. pages 2

[19] G. Igel-Mann, U. Wedig, P. Fuentealba, and H. Stoll. Ground state properties of alkali dimers XY (X, Y = Li to Cs). *The Journal of Chemical Physics*, **84**(9):5007–5012, 1986. pages 2

[20] V. Tarnovsky, M. Bunimovicz, L. Vukovi, B. Stumpf, and B. Bederson. Measurements of the dc electric dipole polarizabilities of the alkali dimer molecules, homonuclear and heteronuclear. *The Journal of Chemical Physics*, **98**(5):3894–3904, 1993. pages

120

[21] M. Aymar and O. Dulieu. Calculation of accurate permanent dipole moments of the lowest $^{1,3}\Sigma^+$ states of heteronuclear alkali dimers using extended basis sets. *The Journal of Chemical Physics*, **122**(20):204302, 05 2005. pages 2

[22] Lincoln D Carr, David DeMille, Roman V Krems, and Jun Ye. Cold and ultracold molecules: science, technology and applications. *New Journal of Physics*, **11**(5):055049, 2009. pages 2

[23] K.-K. Ni, S. Ospelkaus, M. H. G. de Miranda, A. Pe'er, B. Neyenhuis, J. J. Zirbel, S. Kotochigova, P. S. Julienne, D. S. Jin, and J. Ye. A high phase-space-density gas of polar molecules. *Science*, **322**(5899):231–235, 2008. pages 2, 59, 86, 87

[24] Keith Ladouceur, Bruce G. Klappauf, Janelle Van Dongen, Nina Rauhut, Bastian Schuster, Arthur Mills, David J. Jones, and Kirk W. Madison. Compact laser cooling apparatus for simultaneous cooling of lithium and rubidium. *J. Opt. Soc. Am. B*, **26**(2):210–217, 2009. pages 3, 10, 14, 43

[25] B. Deh, W. Gunton, B. G. Klappauf, Z. Li, M. Semczuk, J. Van Dongen, and K. W. Madison. Giant Feshbach resonances in ^{6}Li-^{85}Rb mixtures. *Phys. Rev. A*, **82**:020701, Aug 2010. pages 3, 6, 7

[26] A. Micheli, G. K. Brennen, and P. Zoller. A toolbox for lattice-spin models with polar molecules. *Nature Phys.*, **2**(5):341–347, 2006. pages 3

[27] Immanuel Bloch and Peter Zoller. Chapter 5 - ultracold atoms and molecules in optical lattices. In Alexander L. Fetter Kathryn Levin and Dan M. Stamper-Kurn, editors, *Ultracold Bosonic and Fermionic Gases*, **5** of *Contemporary Concepts of Condensed Matter Science*, pages 121 – 156. Elsevier, 2012. pages

[28] M.A. Baranov. Theoretical progress in many-body physics with ultracold dipolar gases. *Physics Reports*, **464**(3):71 – 111, 2008. pages 3

[29] Mingwu Lu, Nathaniel Q. Burdick, Seo Ho Youn, and Benjamin L. Lev. Strongly dipolar Bose-Einstein condensate of dysprosium. *Phys. Rev. Lett.*, **107**:190401, Oct 2011. pages 3

[30] Mingwu Lu, Nathaniel Q. Burdick, and Benjamin L. Lev. Quantum degenerate dipolar Fermi gas. *Phys. Rev. Lett.*, **108**:215301, May 2012. pages 3

[31] M. Saffman, T. G. Walker, and K. Mølmer. Quantum information with Rydberg atoms. *Rev. Mod. Phys.*, **82**:2313–2363, Aug 2010. pages 3

[32] Daniel Comparat and Pierre Pillet. Dipole blockade in a cold Rydberg atomic sample (invited). *J. Opt. Soc. Am. B*, **27**(6):A208–A232, Jun 2010. pages 3

[33] Goulven Quéméner and Paul S. Julienne. Ultracold molecules under control! *Chemical Reviews*, **112**(9):4949–5011, 2012. PMID: 22921011. pages 3

[34] J. Doyle, B. Friedrich, R.V. Krems, and F. Masnou-Seeuws. Editorial: Quo vadis, cold molecules? *Eur. Phys. J. D*, **31**:149, 2004. pages

[35] Deborah S. Jin and Jun Ye. Introduction to ultracold molecules: New frontiers in quantum and chemical physics. *Chemical Reviews*, **112**(9):4801–4802, 2012. PMID: 22967213. pages 3

[36] M. H. G. de Miranda, A. Chotia, B. Neyenhuis, D. Wang, G. Quéméner, S. Ospelkaus, J. L. Bohn, J. Ye, and D. S. Jin. Controlling the quantum stereodynamics of ultracold bimolecular reactions. *Nature Physics*, **7**:502–507, June 2011. pages 3

[37] Arthur K. Mills, Yi-Fei Chen, Kirk W. Madison, and David J. Jones. Widely tunable, single-mode optical frequency synthesizer with a 100 kHz uncertainty. *J. Opt. Soc. Am. B*, **26**(7):1276–1280, Jul 2009. pages 4, 35

[38] Milena Ivanova, Alexander Stein, Asen Pashov, Horst Knöckel, and Eberhard Tiemann. The $X^1\Sigma^+$ state of LiRb studied by Fourier-transform spectroscopy. *The Journal of Chemical Physics*, **134**(2), 2011. pages 4

[39] Sourav Dutta, Adeel Altaf, D.S. Elliott, and Yong P. Chen. Laser spectroscopy of the $X^1\Sigma^+$ and $B^1\Pi$ states of the LiRb molecule. *Chemical Physics Letters*, **511**(13):7 – 11, 2011. pages 4

[40] Sourav Dutta, Daniel S. Elliott, and Yong P. Chen. Formation of ultracold LiRb molecules by photoassociation near the $\mathrm{Li}(2s^2 S_{1/2})$ + $\mathrm{Rb}(5p^2 P_{1/2})$ asymptote. *EPL (Europhysics Letters)*, **104**(6):63001, 2013. pages 4

[41] Sourav Dutta, Adeel Altaf, John Lorenz, D S Elliott, and Yong P. Chen. Interspecies collision-induced losses in a dual species $^7\mathrm{Li}^{85}\mathrm{Rb}$ magneto-optical trap. *Journal of Physics B: Atomic, Molecular and Optical Physics*, **47**(10):105301, 2014. pages

[42] Sourav Dutta, John Lorenz, Adeel Altaf, D. S. Elliott, and Yong P. Chen. Photoassociation of ultracold LiRb* molecules: Observation of high efficiency and unitarity-limited rate saturation. *Phys. Rev. A*, **89**:020702, Feb 2014. pages 4

[43] T V Tscherbul, Yu V Suleimanov, V Aquilanti, and R V Krems. Magnetic field modification of ultracold molecule-molecule collisions. *New Journal of Physics*, **11**(5):055021, 2009. pages 4

[44] Michael Mayle, Goulven Quéméner, Brandon P. Ruzic, and John L. Bohn. Scattering of ultracold molecules in the highly resonant regime. *Phys. Rev. A*, **87**:012709, Jan 2013. pages 4

[45] P. Makotyn, C. E. Klauss, D. L. Goldberger, E. A. Cornell, and D. S. Jin. Universal dynamics of a degenerate unitary Bose gas. *Nature Phys.*, **10**:116–119, 2014. pages 5

[46] Joanna Karczmarek, James Wright, Paul Corkum, and Misha Ivanov. Optical centrifuge for molecules. *Phys. Rev. Lett.*, **82**:3420–3423, Apr 1999. pages 5

[47] Aleksey Korobenko, Alexander A. Milner, and Valery Milner. Direct observation, study, and control of molecular superrotors. *Phys. Rev. Lett.*, **112**:113004, Mar 2014. pages

[48] Alexander A. Milner, Aleksey Korobenko, John W. Hepburn, and Valery Milner. Effects of ultrafast molecular rotation on collisional decoherence. *Phys. Rev. Lett.*, **113**:043005, Jul 2014. pages 5

[49] Mariusz Semczuk, Xuan Li, Will Gunton, Magnus Haw, Nikesh S. Dattani, Julien Witz, Arthur K. Mills, David J. Jones, and Kirk W. Madison. High-resolution photoassociation spectroscopy of the ^{6}Li$_2$ $1^3\Sigma_g^+$ state. *Phys. Rev. A*, **87**:052505, May 2013. pages 7, 30, 31, 55, 67, 77, 96

[50] Will Gunton, Mariusz Semczuk, and Kirk W. Madison. Realization of BEC-BCS-crossover physics in a compact oven-loaded magneto-optic-trap apparatus. *Phys. Rev. A*, **88**:023624, Aug 2013. pages 7, 10, 12, 30, 31, 41, 42, 43, 45, 48, 49

[51] Will Gunton, Mariusz Semczuk, Nikesh S. Dattani, and Kirk W. Madison. High-resolution photoassociation spectroscopy of the ^{6}Li$_2$ $A(1^1\Sigma_u^+)$ state. *Phys. Rev. A*, **88**:062510, Dec 2013. pages 7, 31, 55, 96

[52] Mariusz Semczuk, Will Gunton, William Bowden, and Kirk W. Madison. Anomalous behavior of dark states in quantum gases of ^{6}Li. *Phys. Rev. Lett.*, **113**:055302, Jul 2014. pages 7, 86, 114

[53] H. J. Metcalf and P. van der Straten. *Laser Cooling and Trapping*. Springer, 1999. pages 7, 42

[54] Philippe Pellegrini, Marko Gacesa, and Robin Côté. Giant formation rates of ultracold molecules via Feshbach-optimized photoassociation. *Phys. Rev. Lett.*, **101**:053201, Aug 2008. pages 8, 61, 62, 73

[55] C. Monroe, W. Swann, H. Robinson, and C. Wieman. Very cold trapped atoms in a vapor cell. *Phys. Rev. Lett.*, **65**:1571–1574, Sep 1990. pages 10

[56] M. S. Santos, P. Nussenzveig, L. G. Marcassa, K. Helmerson, J. Flemming, S. C. Zilio, and V. S. Bagnato. Simultaneous trapping of two different atomic species in a vapor-cell magneto-optical trap. *Phys. Rev. A*, **52**:R4340–R4343, Dec 1995. pages 10

[57] R. S. Williamson and T. Walker. Magneto-optical trapping and ultracold collisions of potassium atoms. *J. Opt. Soc. Am. B*, **12**(8):1393–1397, Aug 1995. pages 10

[58] D. Hoffmann, P. Feng, R. S. Williamson, and T. Walker. Excited-state collisions of trapped ^{85}Rb atoms. *Phys. Rev. Lett.*, **69**:753–756, Aug 1992. pages 10

[59] Brian P. Anderson and Mark A. Kasevich. Enhanced loading of a magneto-optic trap from an atomic beam. *Phys. Rev. A*, **50**:R3581–R3584, Nov 1994. pages 10, 12

[60] S Franke-Arnold, M Arndt, and A Zeilinger. Magneto-optical effects with cold lithium atoms. *Journal of Physics B: Atomic, Molecular and Optical Physics*, **34**(12):2527, 2001. pages 10

[61] Zhong Lin, Kazuko Shimizu, Mingsheng Zhan, Fujio Shimizu, and Hiroshi Takuma. Laser cooling and trapping of li. *Japanese Journal of Applied Physics*, **30**(7B):L1324, 1991. pages 10

[62] T. G. Tiecke, S. D. Gensemer, A. Ludewig, and J. T. M. Walraven. High-flux two-dimensional magneto-optical-trap source for cold lithium atoms. *Phys. Rev. A*, **80**:013409, Jul 2009. pages 10

[63] Paul Lebel. *Contributions to the UBC Quantum Degenerate Gas Lab*. Progress report, University of British Columbia, 2005. pages 11

[64] U. Schünemann, H. Engler, R. Grimm, M. Weidemüller, and M. Zielonkowski. Simple scheme for tunable frequency offset locking of two lasers. *Review of Scientific Instruments*, **70**(1):242–243, 1999. pages 21

[65] M. W. Zwierlein, C. A. Stan, C. H. Schunck, S. M. F. Raupach, S. Gupta, Z. Hadzibabic, and W. Ketterle. Observation of Bose-Einstein condensation of molecules. *Phys. Rev. Lett.*, **91**:250401, Dec 2003. pages 21, 87

[66] S. R. Granade, M. E. Gehm, K. M. O'Hara, and J. E. Thomas. All–optical production of a degenerate Fermi gas. *Phys. Rev. Lett.*, **88**(12):120405, Mar 2002. pages 23, 29, 50, 96

[67] Michael E. Gehm. Properties of ^{6}Li, 2003. pages 24, 33, 100

[68] Rudolf Grimm, Matthias Weidemüller, and Yurii B. Ovchinnikov. *Optical Dipole Traps for Neutral Atoms*, **42** of *Advances In Atomic, Molecular, and Optical Physics*. Academic Press, 2000. pages 26

[69] Thomas Lompe. *An apparatus for the production of molecular Bose-Einstein condensates*. Diploma Thesis, University of Heidelberg, 2008. pages 28

[70] B. DeMarco and D. S. Jin. Onset of fermi degeneracy in a trapped atomic gas. *Science*, **285**(5434):1703–1706, 1999. pages 29

[71] K. M. O'Hara, S. L. Hemmer, M. E. Gehm, S. R. Granade, and J. E. Thomas. Observation of a strongly interacting degenerate Fermi gas of atoms. *Science*, **298**(5601):2179–2182, 2002. pages 29, 47

[72] M. Bartenstein, A. Altmeyer, S. Riedl, S. Jochim, C. Chin, J. Hecker Denschlag, and R. Grimm. Crossover from a molecular Bose-Einstein condensate to a degenerate Fermi gas. *Phys. Rev. Lett.*, **92**:120401, Mar 2004. pages 29, 46

[73] S. Gupta, Z. Hadzibabic, M. W. Zwierlein, C. A. Stan, K. Dieckmann, C. H. Schunck, E. G. M. van Kempen, B. J. Verhaar, and W. Ketterle. Radio-frequency spectroscopy of ultracold fermions. *Science*, **300**(5626):1723–1726, 2003. pages 32, 50

125

[74] C. Chin, M. Bartenstein, A. Altmeyer, S. Riedl, S. Jochim, J. Hecker Denschlag, and R. Grimm. Observation of the pairing gap in a strongly interacting Fermi gas. *Science*, **305**(5687):1128–1130, 2004. pages 33, 47, 87, 111

[75] F. Lang, P. v. d. Straten, B. Brandstatter, G. Thalhammer, K. Winkler, P. S. Julienne, R. Grimm, and J. Hecker Denschlag. Cruising through molecular bound-state manifolds with radiofrequency. *Nature Physics*, **4**:223–226, Jan 2008. pages 32

[76] Kendall B. Davis, Marc-Oliver Mewes, Michael A. Joffe, Michael R. Andrews, and Wolfgang Ketterle. Evaporative cooling of sodium atoms. *Phys. Rev. Lett.*, **74**:5202–5205, Jun 1995. pages 32

[77] E. Arimondo, M. Inguscio, and P. Violino. Experimental determinations of the hyperfine structure in the alkali atoms. *Rev. Mod. Phys.*, **49**:31–75, Jan 1977. pages 32, 33

[78] M. Bartenstein, A. Altmeyer, S. Riedl, R. Geursen, S. Jochim, C. Chin, J. Hecker Denschlag, R. Grimm, A. Simoni, E. Tiesinga, C. J. Williams, and P. S. Julienne. Precise determination of ^{6}Li cold collision parameters by radio-frequency spectroscopy on weakly bound molecules. *Phys. Rev. Lett.*, **94**:103201, Mar 2005. pages 33

[79] Andre Niklas Wenz. *Few-Body Physics in a Three-Component Fermi Gas*. Diploma Thesis, University of Heidelberg, 2008. pages 34

[80] Scott A. Diddams, David J. Jones, Jun Ye, Steven T. Cundiff, John L. Hall, Jinendra K. Ranka, Robert S. Windeler, Ronald Holzwarth, Thomas Udem, and T. W. Hänsch. Direct link between microwave and optical frequencies with a 300 THz femtosecond laser comb. *Phys. Rev. Lett.*, **84**:5102–5105, May 2000. pages 35

[81] Th. Udem, R. Holzwarth, and T. W. Hansch. Optical frequency metrology. *Nature*, **416**:233–237, March 2002. pages 35

[82] Daniel A. Steck. Rubidium ^{85}D line data, September 2013. Available online at http://steck.us/alkalidata (revision 2.1.6). pages 38, 40, 41

[83] David E. Fagnan, Jicheng Wang, Chenchong Zhu, Pavle Djuricanin, Bruce G. Klappauf, James L. Booth, and Kirk W. Madison. Observation of quantum diffractive collisions using shallow atomic traps. *Phys. Rev. A*, **80**:022712, Aug 2009. pages 41, 42

[84] J. Van Dongen, C. Zhu, D. Clement, G. Dufour, J. L. Booth, and K. W. Madison. Trap-depth determination from residual gas collisions. *Phys. Rev. A*, **84**:022708, Aug 2011. pages 41, 42

[85] G. Zürn, T. Lompe, A. N. Wenz, S. Jochim, P. S. Julienne, and J. M. Hutson. Precise characterization of ^{6}Li Feshbach resonances using trap-sideband-resolved RF spectroscopy of weakly bound molecules. *Phys. Rev. Lett.*, **110**:135301, Mar 2013. pages 44, 50, 59, 104, 113

[86] K. M. O'Hara, M. E. Gehm, S. R. Granade, and J. E. Thomas. Scaling laws for evaporative cooling in time-dependent optical traps. *Phys. Rev. A*, **64**:051403, Oct 2001. pages 46

[87] D. S. Petrov, C. Salomon, and G. V. Shlyapnikov. Weakly bound dimers of fermionic atoms. *Phys. Rev. Lett.*, **93**:090404, Aug 2004. pages 46, 87

[88] K. M. O'Hara, S. L. Hemmer, S. R. Granade, M. E. Gehm, J. E. Thomas, V. Venturi, E. Tiesinga, and C. J. Williams. Measurement of the zero crossing in a Feshbach resonance of fermionic ^{6}Li. *Phys. Rev. A*, **66**:041401, Oct 2002. pages 46, 50

[89] A. Trenkwalder, C. Kohstall, M. Zaccanti, D. Naik, A. I. Sidorov, F. Schreck, and R. Grimm. Hydrodynamic expansion of a strongly interacting Fermi-Fermi mixture. *Phys. Rev. Lett.*, **106**:115304, Mar 2011. pages 47

[90] P. Pieri, A. Perali, G. C. Strinati, S. Riedl, M. J. Wright, A. Altmeyer, C. Kohstall, E. R. Sánchez Guajardo, J. Hecker Denschlag, and R. Grimm. Pairing-gap, pseudogap, and no-gap phases in the radio-frequency spectra of a trapped unitary ^{6}Li gas. *Phys. Rev. A*, **84**:011608, Jul 2011. pages 47, 50, 87

[91] T. B. Ottenstein, T. Lompe, M. Kohnen, A. N. Wenz, and S. Jochim. Collisional stability of a three-component degenerate Fermi gas. *Phys. Rev. Lett.*, **101**:203202, Nov 2008. pages 49

[92] J. R. Williams, E. L. Hazlett, J. H. Huckans, R. W. Stites, Y. Zhang, and K. M. O'Hara. Evidence for an excited-state Efimov trimer in a three-component Fermi gas. *Phys. Rev. Lett.*, **103**:130404, Sep 2009. pages 49

[93] Qijin Chen, Jelena Stajic, Shina Tan, and K. Levin. BCS-BEC crossover: From high temperature superconductors to ultracold superfluids. *Physics Reports*, **412**(1):1 – 88, 2005. pages 50

[94] Kevin E. Strecker, Guthrie B. Partridge, and Randall G. Hulet. Conversion of an atomic Fermi gas to a long-lived molecular Bose gas. *Phys. Rev. Lett.*, **91**:080406, Aug 2003. pages 50

[95] K. M. O'Hara, M. E. Gehm, S. R. Granade, S. Bali, and J. E. Thomas. Stable, strongly attractive, two-state mixture of lithium fermions in an optical trap. *Phys. Rev. Lett.*, **85**:2092–2095, Sep 2000. pages 50

[96] S. Jochim, M. Bartenstein, G. Hendl, J. Hecker Denschlag, R. Grimm, A. Mosk, and M. Weidemüller. Magnetic field control of elastic scattering in a cold gas of fermionic lithium atoms. *Phys. Rev. Lett.*, **89**:273202, Dec 2002. pages 50

[97] X. Du, L. Luo, B. Clancy, and J. E. Thomas. Observation of anomalous spin segregation in a trapped Fermi gas. *Phys. Rev. Lett.*, **101**:150401, Oct 2008. pages 50

[98] Kevin M. Jones, Eite Tiesinga, Paul D. Lett, and Paul S. Julienne. Ultracold photoassociation spectroscopy: Long-range molecules and atomic scattering. *Rev. Mod. Phys.*, **78**:483–535, May 2006. pages 55

[99] G. B. Partridge, K. E. Strecker, R. I. Kamar, M. W. Jack, and R. G. Hulet. Molecular probe of pairing in the BEC-BCS crossover. *Phys. Rev. Lett.*, **95**:020404, Jul 2005. pages 55, 113, 114

[100] Dominik M. Bauer, Matthias Lettner, Christoph Vo, Gerhard Rempe, and Stephan Durr. Control of a magnetic Feshbach resonance with laser light. *Nature Physics*, **5**:339–342, May 2009. pages 55, 87

[101] Zhengkun Fu, Pengjun Wang, Lianghui Huang, Zengming Meng, Hui Hu, and Jing Zhang. Optical control of a magnetic Feshbach resonance in an ultracold Fermi gas. *Phys. Rev. A*, **88**:041601, Oct 2013. pages 55, 87

[102] Mi Yan, B. J. DeSalvo, Ying Huang, P. Naidon, and T. C. Killian. Rabi oscillations between atomic and molecular condensates driven with coherent one-color photoassociation. *Phys. Rev. Lett.*, **111**:150402, Oct 2013. pages 55

[103] B. DeMarco, J. L. Bohn, J. P. Burke, M. Holland, and D. S. Jin. Measurement of p-wave threshold law using evaporatively cooled fermionic atoms. *Phys. Rev. Lett.*, **82**:4208–4211, May 1999. pages 55

[104] E. R. I. Abraham, W. I. McAlexander, H. T. C. Stoof, and R. G. Hulet. Hyperfine structure in photoassociative spectra of $^6Li_2$ and $^7Li_2$. *Phys. Rev. A*, **53**:3092–3097, May 1996. pages 56, 65, 81, 104

[105] E. R. I. Abraham, W. I. McAlexander, J. M. Gerton, R. G. Hulet, R. Côté, and A. Dalgarno. Singlet *s*-wave scattering lengths of ^6Li and ^7Li. *Phys. Rev. A*, **53**:R3713–R3715, Jun 1996. pages 56

[106] D. Wang, B. Neyenhuis, M. H. G. de Miranda, K.-K. Ni, S. Ospelkaus, D. S. Jin, and J. Ye. Direct absorption imaging of ultracold polar molecules. *Phys. Rev. A*, **81**:061404, Jun 2010. pages 56

[107] P. Jasik and J.E. Sienkiewicz. Calculation of adiabatic potentials of Li_2. *Chemical Physics*, **323**(23):563 – 573, 2006. pages 57

[108] Magnus Haw. Single color photoassociation spectroscopy of $^6Li_2$ and $^{85}Rb_2$. Undergraduate honours thesis, University of British Columbia, 2012. pages 58, 61

[109] C. H. Schunck, M. W. Zwierlein, C. A. Stan, S. M. F. Raupach, W. Ketterle, A. Simoni, E. Tiesinga, C. J. Williams, and P. S. Julienne. Feshbach resonances in fermionic ^6Li. *Phys. Rev. A*, **71**:045601, Apr 2005. pages 58, 61, 71

[110] Herman Feshbach. A unified theory of nuclear reactions. {II}. *Annals of Physics*, **19**(2):287 – 313, 1962. pages 58

[111] E. Tiesinga, B. J. Verhaar, and H. T. C. Stoof. Threshold and resonance phenomena in ultracold ground-state collisions. *Phys. Rev. A*, **47**:4114–4122, May 1993. pages 58

[112] S. Inouye, M. R. Andrews, J. Stenger, H. J. Miesner, D. M. Stamper-Kurn, and W. Ketterle. Observation of feshbach resonances in a bose-einstein condensate. *Nature*, **392**(6672):151, 03 1998. pages 59

[113] S. Jochim, M. Bartenstein, A. Altmeyer, G. Hendl, S. Riedl, C. Chin, J. Hecker Denschlag, and R. Grimm. Bose-Einstein condensation of molecules. *Science*, **302**(5653):2101–2103, 2003. pages 59, 87

[114] Markus Greiner, Cindy A. Regal, and Deborah S. Jin. Emergence of a molecular Bose-Einstein condensate from a Fermi gas. *Nature*, **426**:537–540, December 2003. pages 59

129

[115] Thierry Lahaye, Tobias Koch, Bernd Frohlich, Marco Fattori, Jonas Metz, Axel Griesmaier, Stefano Giovanazzi, and Tilman Pfau. Strong dipolar effects in a quantum ferrofluid. *Nature*, **448**:672–675, August 2007. pages 59

[116] Albert Frisch, Michael Mark, Kiyotaka Aikawa, Francesca Ferlaino, John L. Bohn, Constantinos Makrides, Alexander Petrov, and Svetlana Kotochigova. Quantum chaos in ultracold collisions of gas-phase erbium atoms. *Nature*, **507**:475–479, March 2014. pages 59

[117] Kristian Baumann, Nathaniel Q. Burdick, Mingwu Lu, and Benjamin L. Lev. Observation of low-field fano-feshbach resonances in ultracold gases of dysprosium. *Phys. Rev. A*, **89**:020701, Feb 2014. pages 59

[118] Cheng Chin, Rudolf Grimm, Paul Julienne, and Eite Tiesinga. Feshbach resonances in ultracold gases. *Rev. Mod. Phys.*, **82**(2):1225–1286, Apr 2010. pages 59, 60, 104

[119] H R Sadeghpour, J L Bohn, M J Cavagnero, B D Esry, I I Fabrikant, J H Macek, and A R P Rau. Collisions near threshold in atomic and molecular physics. *Journal of Physics B: Atomic, Molecular and Optical Physics*, **33**(5):R93, 2000. pages 61

[120] J. Zhang, E. G. M. van Kempen, T. Bourdel, L. Khaykovich, J. Cubizolles, F. Chevy, M. Teichmann, L. Tarruell, S. J. J. M. F. Kokkelmans, and C. Salomon. p-wave Feshbach resonances of ultracold ^{6}Li. *Phys. Rev. A*, **70**:030702, Sep 2004. pages 61, 62

[121] G. Herzberg. *Molecular spectra and molecular structure, I. Spectra of diatomic molecules*. D. Van Nostrand, New York, 1950. pages 63, 75

[122] G. M. Falco and H. T. C. Stoof. Dressed molecules in resonantly interacting ultracold atomic Fermi gases. *Phys. Rev. A*, **75**:023612, Feb 2007. pages 64, 96, 108

[123] F. Martin, R. Bacis, J. Vergs, C. Linton, G. Bujin, C.H. Cheng, and E. Stad. Fourier spectrometry investigation of the $1^3\Sigma_g^+ \to a^3\Sigma_u^+$ transition of the ^{7}Li$_2$ molecule. *Spectrochimica Acta Part A: Molecular Spectroscopy*, **44**(12):1369 – 1376, 1988. pages 67

[124] C. Linton, T. L. Murphy, F. Martin, R. Bacis, and J. Verges. Fourier transform spectroscopy of the $1^3\Sigma_g^+$–a$^3\Sigma_u^+$ transition of the ^{6}Li$_2$ molecule. *The Journal of Chemical Physics*, **91**(10):6036–6041, 1989. pages 67

[125] E. R. I. Abraham, N. W. M. Ritchie, W. I. McAlexander, and R. G. Hulet. Photoassociative spectroscopy of long-range states of ultracold $^6Li_2$ and $^7Li_2$. *The Journal of Chemical Physics*, **103**(18):7773–7778, 1995. pages 67, 81

[126] M. Aubert-Frecon, G. Hadinger, S. Magnier, and S. Rousseau. Analytical formulas for long-range energies of the $16\Omega_{g,u}^{(+/-)}$ states of alkali dimers dissociating into M(ns) +M(np^2P_J). *Journal of Molecular Spectroscopy*, **188**(2):182 – 189, 1998. pages 67

[127] R. Côté and A. Dalgarno. Mechanism for the production of $^6Li_2$ and $^7Li_2$ ultracold molecules. *Journal of Molecular Spectroscopy*, **195**(2):236 – 245, 1999. pages 68

[128] Robert Schlapp. Intensities in singlet-triplet bands of diatomic molecules. *Phys. Rev.*, **39**:806–815, Mar 1932. pages 75

[129] Boris Minaev. Ab initio study of low-lying triplet states of the lithium dimer. *Spectrochimica Acta Part A: Molecular and Biomolecular Spectroscopy*, **62**(4-5):790 – 799, 2005. pages 75, 76

[130] C. Linton, F. Martin, I. Russier, A.J. Ross, P. Crozet, S. Churassy, and R. Bacis. Observation and analysis of the $A^1\Sigma_u^+$ state of $^6Li_2$ from $v = 0$ to the dissociation limit. *Journal of Molecular Spectroscopy*, **175**(2):340 – 353, 1996. pages 81, 82

[131] Robert J. Le Roy, Nikesh S. Dattani, John A. Coxon, Amanda J. Ross, Patrick Crozet, and Colan Linton. Accurate analytic potentials for Li$_2$ $X^1\Sigma_g^+$ and Li$_2$ a$^1\Sigma_u^+$ from 2 to 90 A, and the radiative lifetime of Li(2p). *The Journal of Chemical Physics*, **131**(20):204309, 2009. pages 82, 105

[132] E. Arimondo and G. Orriols. Nonabsorbing atomic coherences by coherent two-photon transitions in a three-level optical pumping. *Lettere Al Nuovo Cimento Series 2*, **17**(10):333–338, 1976. pages 86

[133] Michael Fleischhauer, Atac Imamoglu, and Jonathan P. Marangos. Electromagnetically induced transparency: Optics in coherent media. *Rev. Mod. Phys.*, **77**:633–673, Jul 2005. pages 86, 91

[134] Lene Vestergaard Hau, S. E. Harris, Zachary Dutton, and Cyrus H. Behroozi. Light speed reduction to 17 metres per second in an ultracold atomic gas. *Nature*, **397**:594–598, February 1999. pages 86

131

[135] J. Oreg, F. T. Hioe, and J. H. Eberly. Adiabatic following in multilevel systems. *Phys. Rev. A*, **29**:690–697, Feb 1984. pages 86

[136] K. Bergmann, H. Theuer, and B. W. Shore. Coherent population transfer among quantum states of atoms and molecules. *Rev. Mod. Phys.*, **70**:1003–1025, Jul 1998. pages 86, 87

[137] S. Moal, M. Portier, J. Kim, J. Dugué, U. D. Rapol, M. Leduc, and C. Cohen-Tannoudji. Accurate determination of the scattering length of metastable helium atoms using dark resonances between atoms and exotic molecules. *Phys. Rev. Lett.*, **96**:023203, Jan 2006. pages 86, 88

[138] S. Moal, M. Portier, N. Zahzam, and M. Leduc. Lifetime of weakly bound dimers of ultracold metastable helium studied by photoassociation. *Phys. Rev. A*, **75**:033415, Mar 2007. pages 86

[139] R. Dumke, J. D. Weinstein, M. Johanning, K. M. Jones, and P. D. Lett. Sub-natural-linewidth quantum interference features observed in photoassociation of a thermal gas. *Phys. Rev. A*, **72**:041801, Oct 2005. pages 86

[140] K. Winkler, G. Thalhammer, M. Theis, H. Ritsch, R. Grimm, and J. Hecker Denschlag. Atom-molecule dark states in a Bose-Einstein condensate. *Phys. Rev. Lett.*, **95**:063202, Aug 2005. pages 86, 92, 102

[141] K. Winkler, F. Lang, G. Thalhammer, P. v. d. Straten, R. Grimm, and J. Hecker Denschlag. Coherent optical transfer of Feshbach molecules to a lower vibrational state. *Phys. Rev. Lett.*, **98**:043201, Jan 2007. pages 86, 87

[142] F. Lang, K. Winkler, C. Strauss, R. Grimm, and J. Hecker Denschlag. Ultracold triplet molecules in the rovibrational ground state. *Phys. Rev. Lett.*, **101**:133005, Sep 2008. pages 86, 87

[143] Simon Stellmer, Benjamin Pasquiou, Rudolf Grimm, and Florian Schreck. Creation of ultracold Sr_2 molecules in the electronic ground state. *Phys. Rev. Lett.*, **109**:115302, Sep 2012. pages 86, 87

[144] Johann G. Danzl, Elmar Haller, Mattias Gustavsson, Manfred J. Mark, Russell Hart, Nadia Bouloufa, Olivier Dulieu, Helmut Ritsch, and Hanns-Christoph Nägerl. Quantum gas of deeply bound ground state molecules. *Science*, **321**(5892):1062–1066, 2008. pages 86, 87

[145] S. Ospelkaus, A. Pe'er, K.-K. Ni, J. J. Zirbel, B. Neyenhuis, S. Kotochigova, P. S. Julienne, J. Ye, and D. S. Jin. Efficient state transfer in an ultracold dense gas of heteronuclear molecules. *Nature Physics*, **4**(8):622–626, 8 2008. pages 86, 87

[146] B. D. Esry, Chris H. Greene, and James P. Burke. Recombination of three atoms in the ultracold limit. *Phys. Rev. Lett.*, **83**:1751–1754, Aug 1999. pages 86

[147] Johann G. Danzl, Manfred J. Mark, Elmar Haller, Mattias Gustavsson, Russell Hart, Jesus Aldegunde, Jeremy M. Hutson, and Hanns-Christoph Nägerl. An ultracold high-density sample of rovibronic ground-state molecules in an optical lattice. *Nat. Phys.*, **6**:265–270, February 2010. pages 87

[148] Tetsu Takekoshi, Lukas Reichsöllner, Andreas Schindewolf, Jeremy M. Hutson, C. Ruth Le Sueur, Olivier Dulieu, Francesca Ferlaino, Rudolf Grimm, and Hanns-Christoph Nägerl. Ultracold dense samples of dipolar RbCs molecules in the rovibrational and hyperfine ground state. *Phys. Rev. Lett.*, **113**:205301, Nov 2014. pages 87

[149] Peter K. Molony, Philip D. Gregory, Zhonghua Ji, Bo Lu, Michael P. Köppinger, C. Ruth Le Sueur, Caroline L. Blackley, Jeremy M. Hutson, and Simon L. Cornish. Creation of ultracold ^{87}Rb^{133}Cs molecules in the rovibrational ground state. *Phys. Rev. Lett.*, **113**:255301, Dec 2014. pages 87

[150] Jee Woo Park, Cheng-Hsun Wu, Jennifer Schloss, Qingyang Wang, Sebastian WillL, and Martin Zwierlein. Towards creating fermionic ground state molecules of ^{23}Na^{40}K with strong dipolar interactions. Abstract, DAMOP14 meeting of the American Physical Society, 2014. pages 87

[151] T. Mukaiyama, J. R. Abo-Shaeer, K. Xu, J. K. Chin, and W. Ketterle. Dissociation and decay of ultracold sodium molecules. *Phys. Rev. Lett.*, **92**:180402, May 2004. pages 87

[152] D. Jaksch, V. Venturi, J. I. Cirac, C. J. Williams, and P. Zoller. Creation of a molecular condensate by dynamically melting a Mott insulator. *Phys. Rev. Lett.*, **89**:040402, Jul 2002. pages 87

[153] Andrew Robertson, Lei Jiang, Han Pu, Weiping Zhang, and Hong Y. Ling. Macroscopic atom-molecule dark state and its collective excitations in fermionic systems. *Phys. Rev. Lett.*, **99**:250404, Dec 2007. pages 87

[154] Meng Shao-Ying, Chen Xi-Hao, Wu Wei, and Fu Li-Bin. Linear instability and adiabaticity of a dark state during conversion of two species of fermionic atoms to stable molecules. *Chinese Physics B*, **21**(4):040308, 2012. pages 87

[155] Lei Jiang, Han Pu, Weiping Zhang, and Hong Y. Ling. Detection of Fermi pairing via electromagnetically induced transparency. *Phys. Rev. A*, **80**:033606, Sep 2009. pages 87

[156] Marijan Koštrun and Robin Côté. Two-color spectroscopy of fermions in mean-field BCS-BEC crossover theory. *Phys. Rev. A*, **73**:041607, Apr 2006. pages

[157] H. Jing, Y. Deng, and P. Meystre. Slow-light probe of Fermi pairing through an atom-molecule dark state. *Phys. Rev. A*, **83**:063605, Jun 2011. pages 87

[158] Haibin Wu and J. E. Thomas. Optical control of Feshbach resonances in Fermi gases using molecular dark states. *Phys. Rev. Lett.*, **108**:010401, Jan 2012. pages 87, 104, 105, 118

[159] Haibin Wu and J. E. Thomas. Optical control of the scattering length and effective range for magnetically tunable Feshbach resonances in ultracold gases. *Phys. Rev. A*, **86**:063625, Dec 2012. pages 87, 104, 105, 108

[160] S. Jochim, M. Bartenstein, A. Altmeyer, G. Hendl, C. Chin, J. Hecker Denschlag, and R. Grimm. Pure gas of optically trapped molecules created from fermionic atoms. *Phys. Rev. Lett.*, **91**:240402, Dec 2003. pages 87

[161] M. W. Zwierlein, C. A. Stan, C. H. Schunck, S. M. F. Raupach, A. J. Kerman, and W. Ketterle. Condensation of pairs of fermionic atoms near a Feshbach resonance. *Phys. Rev. Lett.*, **92**:120403, Mar 2004. pages 87

[162] E. R. I. Abraham, W. I. McAlexander, J. M. Gerton, R. G. Hulet, R. Côté, and A. Dalgarno. Triplet s-wave resonance in ^{6}Li collisions and scattering lengths of ^{6}Li and ^{7}Li. *Phys. Rev. A*, **55**:R3299–R3302, May 1997. pages 88, 95

[163] U. Schlöder, T. Deuschle, C. Silber, and C. Zimmermann. Autler-Townes splitting in two-color photoassociation of ^{6}Li. *Phys. Rev. A*, **68**:051403, Nov 2003. pages 88

134

[164] Y. N. Martinez de Escobar, P. G. Mickelson, P. Pellegrini, S. B. Nagel, A. Traverso, M. Yan, R. Côté, and T. C. Killian. Two-photon photoassociative spectroscopy of ultracold ^{88}Sr. *Phys. Rev. A*, **78**:062708, Dec 2008. pages 88, 91, 94

[165] W. Kolos and L. Wolniewicz. Vibrational and rotational energies for the $B^1\Sigma_u^+$, $C^1\Pi_u$, and a $^3\Sigma_g^+$ states of the hydrogen molecule. *The Journal of Chemical Physics*, **48**(8):3672–3680, 1968. pages 88

[166] A. J. Moerdijk and B. J. Verhaar. Laser cooling and the highest bound states of the Na diatom system. *Phys. Rev. A*, **51**:R4333–R4336, Jun 1995. pages 88, 104

[167] John L. Bohn and P. S. Julienne. Semianalytic treatment of two-color photoassociation spectroscopy and control of cold atoms. *Phys. Rev. A*, **54**:R4637–R4640, Dec 1996. pages 88

[168] John L. Bohn and P. S. Julienne. Semianalytic theory of laser-assisted resonant cold collisions. *Phys. Rev. A*, **60**:414–425, Jul 1999. pages 88, 90

[169] Maximilien Portier, Michele Leduc, and Claude Cohen-Tannoudji. Fano profiles in two-photon photoassociation spectra. *Faraday Discuss.*, **142**:415–428, 2009. pages 91

[170] Thomas Zanon-Willette, Emeric de Clercq, and Ennio Arimondo. Ultrahigh-resolution spectroscopy with atomic or molecular dark resonances: Exact steady-state line shapes and asymptotic profiles in the adiabatic pulsed regime. *Phys. Rev. A*, **84**:062502, Dec 2011. pages 91, 92

[171] Andrew J. Kerman, Jeremy M. Sage, Sunil Sainis, Thomas Bergeman, and David DeMille. Production and state-selective detection of ultracold RbCs molecules. *Phys. Rev. Lett.*, **92**:153001, Apr 2004. pages 92

[172] J. Deiglmayr, A. Grochola, M. Repp, K. Mörtlbauer, C. Glück, J. Lange, O. Dulieu, R. Wester, and M. Weidemüller. Formation of ultracold polar molecules in the rovibrational ground state. *Phys. Rev. Lett.*, **101**:133004, Sep 2008. pages 92

[173] E. R. I. Abraham, W. I. McAlexander, C. A. Sackett, and Randall G. Hulet. Spectroscopic determination of the *s*-wave scattering length of lithium. *Phys. Rev. Lett.*, **74**:1315–1318, Feb 1995. pages 93, 94

135

[174] H. Wang, A. N. Nikolov, J. R. Ensher, P. L. Gould, E. E. Eyler, W. C. Stwalley, J. P. Burke, J. L. Bohn, Chris. H. Greene, E. Tiesinga, C. J. Williams, and P. S. Julienne. Ground-state scattering lengths for potassium isotopes determined by double-resonance photoassociative spectroscopy of ultracold ^{39}K. *Phys. Rev. A*, **62**:052704, Oct 2000. pages

[175] C. C. Tsai, R. S. Freeland, J. M. Vogels, H. M. J. M. Boesten, B. J. Verhaar, and D. J. Heinzen. Two-color photoassociation spectroscopy of ground state Rb$_2$. *Phys. Rev. Lett.*, **79**:1245–1248, Aug 1997. pages

[176] Ch. Lisdat, N. Vanhaecke, D. Comparat, and P. Pillet. Line shape analysis of two-colour photoassociation spectra on the example of the Cs ground state. *The European Physical Journal D - Atomic, Molecular, Optical and Plasma Physics*, **21**(3):299–309, 2002. pages

[177] Lus E. E. de Araujo, Jonathan D. Weinstein, Stephen D. Gensemer, Fredrik K. Fatemi, Kevin M. Jones, Paul D. Lett, and Eite Tiesinga. Two-color photoassociation spectroscopy of the lowest triplet potential of Na$_2$. *The Journal of Chemical Physics*, **119**(4):2062–2074, 2003. pages

[178] N. Vanhaecke, Ch. Lisdat, B. TJampens, D. Comparat, A. Crubellier, and P. Pillet. Accurate asymptotic ground state potential curves of Cs$_2$ from two-colour photoassociation. *The European Physical Journal D - Atomic, Molecular, Optical and Plasma Physics*, **28**(3):351–360, 2004. pages

[179] Masaaki Kitagawa, Katsunari Enomoto, Kentaro Kasa, Yoshiro Takahashi, Roman Ciuryło, Pascal Naidon, and Paul S. Julienne. Two-color photoassociation spectroscopy of ytterbium atoms and the precise determinations of s-wave scattering lengths. *Phys. Rev. A*, **77**:012719, Jan 2008. pages

[180] C. Strauss, T. Takekoshi, F. Lang, K. Winkler, R. Grimm, J. Hecker Denschlag, and E. Tiemann. Hyperfine, rotational, and vibrational structure of the $a^3\Sigma_u^+$ state of ^{87}Rb$_2$. *Phys. Rev. A*, **82**:052514, Nov 2010. pages

[181] Frank Münchow, Cristian Bruni, Maximilian Madalinski, and Axel Görlitz. Two-photon photoassociation spectroscopy of heteronuclear YbRb. *Phys. Chem. Chem. Phys.*, **13**:18734–18737, 2011. pages 94

[182] M. W. J. Romans and H. T. C. Stoof. Bogoliubov theory of Feshbach molecules in the BEC-BCS crossover. *Phys. Rev. A*, **74**:053618, Nov 2006. pages 114

[183] G. Salomon, L. Fouché, P. Wang, A. Aspect, P. Bouyer, and T. Bourdel. Gray-molasses cooling of ^{39}K to a high phase-space density. *EPL (Europhysics Letters)*, **104**(6):63002, 2013. pages 117

[184] D. Rio Fernandes, F. Sievers, N. Kretzschmar, S. Wu, C. Salomon, and F. Chevy. Sub-Doppler laser cooling of fermionic ^{40}K atoms in three-dimensional gray optical molasses. *EPL (Europhysics Letters)*, **100**(6):63001, 2012. pages 117

[185] Paul Hamilton, Geena Kim, Trinity Joshi, Biswaroop Mukherjee, Daniel Tiarks, and Holger Müller. Sisyphus cooling of lithium. *Phys. Rev. A*, **89**:023409, Feb 2014. pages 117

[186] Andrew T. Grier, Igor Ferrier-Barbut, Benno S. Rem, Marion Delehaye, Lev Khaykovich, Frédéric Chevy, and Christophe Salomon. Λ-enhanced sub-Doppler cooling of lithium atoms in D_1 gray molasses. *Phys. Rev. A*, **87**:063411, Jun 2013. pages 117